UNIVERSIDAD DE MURCIA

FACULTAD DE MEDICINA

Study of the optical effect of cataracts and its correction using wavefront shaping

Estudio de los efectos ópticos de las cataratas y su corrección mediante manipulado del frente de onda

D. Augusto Arias Gallego

2018

A toda mi familia

A mis abuelos

TABLE OF CONTENTS

LIST OF FIGURES

LIST OF TABLES

LIST OF ABBREVIATIONS

PSF	Point Spread Function
RMS	Root Mean Squared
CIE	Commission Internationale de l'Eclairage
FFT	Fast Fourier Transform
MAR	Minimum Angle of Resolution
CS	Constrast Sensitivity
VA	Visual Acuity
LOCS-III	Lens Opacity Classification System III
IOL	IntraOcular Lens
SLM	Spatial Light Modulator
LCoS	Liquid Crystal on Silicon
WS	Wavefront Shaping
DMD	Digital Micromirror Device
MEM	Micro-Electromechanical System
IDCT	Inverse Discrete Cosine Transform
HO	High-Order (aberrations)
SR	Strehl Ratio
MTF	Modulation Transfer Function
LED	Light-Emitting Diode
AMD	Age-related Macular Degeneration
LRT	Laser Ray-Tracing
EMCCD	Electron Multiplying Charge-Coupled Device
FWHM	Full Width at Half Maximum
CR	Correlation Coeffient
VSMTF	Visual Strehl ratio calculated at MTF
DOF	Depth of Focus
CMOS	Complementary Metal-Oxide Semiconductor
HMD	Head-Mounted Display
SP	Single-pass
DP	Double-pass
LUT	Look-Up Table

RESUMEN

<u>Motivación y objetivo</u>

Las cataratas son una patología caracterizada por la opacificación del cristalino, cuyo origen se encuentra en los cambios físicos y químicos de las proteínas que lo componen. Esos cambios producen el incremento de las aberraciones ópticas y la dispersión (o *scattering*) intraocular, volviendo borrosas, y reduciendo el contraste, de las imágenes en la retina.

El tratamiento actual para esta patología es la cirugía, donde el cristalino afectado es extraído y reemplazado por una lente intraocular. Aunque este procedimiento se practica de manera rutinaria, especialmente en los países desarrollados, las cataratas siguen siendo una de las principales causas de ceguera en el mundo. Por tanto, surge la necesidad de una solución no invasiva para aumentar la cobertura de los tratamientos. En la revisión del estado del arte sólo se encontró un antecedente (publicado en 1973) con este objetivo, donde la formación de imágenes a través de un cristalino cataratoso extraído fue restaurada usando métodos holográficos. Sin embargo, los requerimientos de este tipo de montaje no permitieron su implementación *in vivo*. Además, el desempeño de los sensores de frente de onda incorporados a los sistemas actuales de óptica adaptativa, está limitado por la cantidad de aberraciones y *scattering* presentes en los ojos cataratosos.

En esta tesis se propone la aplicación de una técnica de manipulación del frente de onda (WS, del inglés *wavefront shaping*) para compensar los efectos de la catarata, suponiendo el objetivo de evaluar su desempeño. Esta técnica ha sido previamente aplicada para la formación de las imágenes a través de medios turbios.

<u>Métodos</u>

Con el fin de evitar la influencia de los fenómenos dinámicos del ojo, presentes en una implementación *in vivo*, la evaluación de la técnica de WS se realizó en un banco óptico.

En primer lugar, se desarrolló un método para generar los efectos de las cataratas de forma realista, modelando el *scattering* intraocular mediante mapas de fase ubicados en la pupila de entrada. Los mapas de fase se calcularon usando la transformada cosenoidal inversa de una superficie que modula valores aleatorios. Tal superficie fue inicialmente descrita a través de una ley potencial de la frecuencia espacial para reproducir los efectos del *scattering* intraocular, cuyo dominio en la función de punto esparcido (PSF, del inglés *point spread function*) corresponde a ángulos mayores de 1 grado, aproximadamente. Una característica de este modelo es la generación de varias cantidades de *scattering* intraocular manipulando simplemente la amplitud de los mapas de fase calculados. Seguidamente, la complejidad de la superficie se incrementó para mejorar la reproducción

de los efectos de las aberraciones, las cuales redistribuyen la PSF en los ángulos menores a 1 grado.

Los mapas de fase calculados con el modelo fueron reproducidos en un modulador espacial de luz de cristal líquido sobre silicio (LCoS, del inglés *Liquid Crystal on Silicon*), con el fin de comprobar experimentalmente las cantidades de *scattering* intraocular generadas. El método de integración óptica fue usado para medir las cantidades de *scattering*. Este montaje experimental fue modificado para desarrollar un simulador visual, permitiendo evaluar el impacto de varias cantidades de *scattering* inducidas en la agudeza visual y la sensibilidad al contraste (a 3 ciclos por grado), tanto en la fóvea como a dos excentricidades (5 y 10 grados del campo visual nasal).

Para las pruebas en el banco óptico se usó un doble paso del haz por un LCoS. El acondicionamiento del LCoS para esta aplicación conllevó la calibración de la modulación de fase, la optimización de la respuesta temporal, la compensación de las aberraciones preexistentes en el montaje y la eliminación de la luz no modulada. El área del LCoS fue dividida en dos mitades, conjugadas entre sí, para presentar simultáneamente los mapas de fases cataratosos y de prueba, simulando un solo paso por el medio ocular. Según la técnica de WS, los mapas de fase de prueba están compuestos por segmentos regulares cuyas fases son ajustadas para producir una interferencia constructiva en una posición espacial de la PSF. De esta forma, los efectos de tres niveles de cataratas (asociados a valores de *scattering* $\text{Log}_{10}[s]$ desde 1.75 a 2.25) fueron corregidos usando siete tamaños de segmentos desde 16 a 80 pixeles del LCoS. La calidad de la corrección fue inicialmente evaluada mediante la mejora de la PSF. Seguidamente, se calcularon la razón visual de Strehl y los coeficientes de correlación (métricas relacionadas a la función visual) sobre las imágenes con y sin la corrección de los efectos inducidos. Adicionalmente, un canal visual fue adaptado al banco de pruebas para la valoración subjetiva de la calidad de la corrección a través de la agudeza visual. El análisis sobre la capacidad de la técnica WS para minimizar el *scattering* se completó utilizando simulaciones numéricas. Por último, el desempeño de la técnica de WS se evaluó simulando un doble paso simétrico y asimétrico por el medio ocular, modificando ligeramente el banco óptico desarrollando.

<u>Resultados</u>

Generación artificial de cantidades programadas del scattering intraocular

El modelado de mapas de fase se usó para generar controladamente las cantidades de *scattering* intraocular. Estas cantidades fueron experimentalmente medidas usando el método de integración óptica. La relación entre las cantidades de *scattering* programadas y experimentalmente medidas es lineal con una pendiente de 0.96, demostrando la exactitud del método desarrollado.

Reproducción de fenómenos oculares a partir de un modelo de mapas de fase

Los siguientes fenómenos ópticos oculares fueron reproducidos usando el modelo modificado de los mapas de fases para incluir las aberraciones de alto orden: el efecto del envejecimiento sobre la cantidad de aberraciones de alto orden y la razón de Strehl, la dependencia del *scattering* introcular con la longitud de onda y la corona ciliar. La fidelidad del modelo fue comprobada al comparar los resultados numéricos con las estadísticas de estudios clínicos y experimentales sobre los mismos fenómenos.

Evaluación de los efectos del scattering intraocular en la función visual foveal

Las medidas de agudeza visual y sensibilidad al contraste usando el simulador visual permitieron establecer las relaciones entre ambas métricas con las cantidades de *scattering* intraocular. Así, se observó que la agudeza visual (en unidades LogMAR) se incrementa linealmente con la cantidad de *scattering* artificialmente generado. Además, los valores logarítmicos de la sensibilidad al contraste decrecen linealmente con la cantidad de *scattering*.

Explicación de los beneficios de la cirugía de cataratas en pacientes con patologías retinianas preexistentes

Usando el simulador visual de los efectos del *scattering* intraocular, se realizaron medidas de agudeza visual y sensibilidad al contraste en la región periférica de la retina. Las dependencias entre ambas métricas con la cantidad de *scattering* generado en esas regiones son similares a las encontradas en la fóvea. Los resultados permitieron explicar la modesta mejora de la agudeza visual tras la cirugía de cataratas en pacientes con degeneración macular relacionada con la edad, los cuales fueron previamente reportados.

Corrección de los efectos simulados de las cataratas

Las PSFs optimizadas por la técnica de WS, independientes de la cantidad de *scattering* intraocular generado, corresponden a un pico de energía sobre un fondo de luz no corregida. La altura del pico depende del tamaño de los segmentos del mapa de fase corrector. Sin embargo, se observó un umbral en la mejora de la PSF para el menor nivel de catarata reproducido, y tamaños de segmento menores de 69 μm. Los mejoramientos de las PSFs se reflejaron en incrementos de las funciones de transferencia de modulación y, en consecuencia, la razón visual de Strehl. Los coeficientes de correlación se incrementaron para todos los niveles de catarata y tamaños de segmentos. Igualmente, la agudeza visual se mejoró por efecto de la corrección, siendo limitada por las aberraciones naturales de los ojos que la valoraron para tamaño de segmentos menores de 137 μm en todos los niveles de catarata simulados.

Los resultados de las simulaciones numéricas de las PSFs corregidas demostraron que el rango angular en el cual la corrección redistribuye la energía está dado por el tamaño de segmento. El máximo rango angular fue 0.56 grados (radio), asociado a un tamaño de segmento igual a 55 μm. Este rango angular no es suficiente para corregir el *scattering*

intraocular, cuyo dominio son ángulos mayores a 1 grado. Por lo tanto, el *scattering* no corregido disminuye el contraste de las imágenes vistas a través del sistema corrector basado en la técnica de WS. Para solventar esta limitación, se propone la simplificación digital de las imágenes proyectadas a través del corrector, excluyendo las fuentes de deslumbramiento presentes.

Definición de los rangos de tolerancia de los desplazamientos entre los mapas de fase cataratosos y correctores

Los coeficientes de correlación fueron evaluados, usando un optotipo con un tamaño de 5.4 arcmin, mientras se desplazaban lateralmente los mapas de fase correctores respecto los cataratosos. Según el análisis, el optotipo es reconocible en los siguientes rangos de desplazamientos: 158, 110 y 82 μm para valores $Log_{10}[s]$ correspondientes a 1.75, 2.00 and 2.25. Es decir, a medida que se incrementa la cantidad de *scattering* intraocular, se reduce la tolerancia a los descentramientos. Estos rangos son menores al promedio de la amplitud (horizontal) de los movimientos oculares durante la fijación, cuyo valor es 190 μm. Por lo tanto, una futura implementación *in-vivo* de esta técnica posiblemente requerirá un sistema de seguimiento de pupila.

Corrección de los efectos simulados de las cataratas en doble paso

La corrección en una configuración de doble paso, usando luz coherente, fue altamente influenciada por la difusión retiniana simulada. Así, aunque la PSF del doble paso fue optimizada, esta corrección no beneficiará la calidad visual.

Conclusiones

- Se desarrolló una nueva metodología para diseñar mapas de fase aleatorios de modo que reproduzcan la distribución angular de la PSF, especialmente en el dominio de la dispersión intraocular. Las cantidades de *scattering*, generadas por el método, fueron verificadas experimentalmente usando un LCoS.

- La capacidad de la metodología fue extendida para reproducir la PSF ocular en todo el rango angular, incluyendo el dominio de las aberraciones de alto orden.

- Se implementó un simulador visual usando un LCoS para proyectar los mapas de fase calculados. En este instrumento se reveló que tanto la agudeza visual (en unidades LogMAR) como los valores logarítmicos de la sensibilidad al contraste tienen una dependencia lineal con la cantidad de *scattering* intraocular inducido.

- Para evaluar la técnica de WS se desarrolló un instrumento que emplea un doble paso por un LCoS para, simultáneamente, generar y corregir los efectos de varios niveles de cataratas. Inicialmente, el instrumento se usó para compensar los efectos inducidos de turbulencia y turbidez por separado.

- Los efectos de tres cantidades inducidas de *scattering*, asociadas a tres niveles de cataratas, fueron parcialmente corregidos usando siete tamaños de segmentos de los

mapas de fase correctores. Esta corrección se realizó simulando un solo paso por el medio ocular.

- En general, el principal efecto de la compensación es el aumento de la nitidez e intensidad en las imágenes. El mejoramiento de la intensidad depende del número de segmentos. Sin embargo, se observó un umbral en la mejora de la PSF con los efectos de una catarata débil (es decir, $Log_{10}[s] \equiv 1.75$) usando tamaños de segmento menores a 69 μm.

- Para la implementación *in vivo* de la técnica de WS podría ser necesario un sistema de seguimiento de pupila. Esto se debe a que los rangos de desplazamientos entre los mapas de fase cataratosos y correctores para los cuales un optotipo permanece reconocible, son menores a la amplitud de los movimientos oculares durante la fijación.

- La técnica de WS no tiene impacto en la minimización de la cantidad de *scattering* intraocular porque su rango angular de acción depende del tamaño de los segmentos del mapa de fase corrector. El máximo rango angular considerado en los experimentos desarrollados fue 0.56 grados. Una estrategia propuesta para evitar la reducción de contraste por el *scattering* no corregida, consiste en simplificar las imágenes proyectadas a través del corrector.

- El instrumento fue modificado para evaluar el desempeño de la técnica WS simulando un doble paso a través del medio ocular cataratoso. La corrección realizada usando luz coherente estuvo altamente influenciada por la difusión en la retina, lo que imposibilitó un beneficio efectivo en la calidad de la visión.

SUMMARY

Cataract is one of the main causes of visual impairment in the world. It increases both intraocular scattering and aberrations because microscopic and macroscopic changes of the refractive index in the lens. Consequently, the effect of cataracts is the simultaneous blurring and reduction of the contrast in the retinal images. The intensity of the effect is associated to the amount of straylight, which is a quantification of the impinging light into the eye deviated to large retinal angles (i.e., larger than one degree).

The current treatment of cataract is surgery, where the lens is extracted and replaced with an intraocular lens. However, the requirements for its safe practice have not allowed to cover its global demand, especially in developing countries. Therefore, a non-invasive optical technique is appealing, and its development is an open challenge. There is a unique precedent reported in 1973, where the phase of an extracted lens was retrieved using holography for its posterior phase conjugation. Moreover, the performance of current adaptive optics systems is limited by the large amount of scattering that is present in the cataractous eyes.

On the other hand, wavefront-shaping (WS) technique was developed for imaging through opaque samples. In this work, the WS technique is proposed to partially correct the effects of cataracts non-invasively *in-vivo*, being the objective to evaluate its performance for this application. The technique was tested in an optical bench to avoid the influence of the dynamics of ocular phenomena which is inherent in an *in-vivo* implementation.

As first step, a model was developed to reproduce the ocular point spread function (PSF) with different amounts of straylight through the weighted summation of both low and high spatial frequency phase perturbations at the entrance pupil of the eye. The model was initially tested by numerically calculating the following ocular phenomena and their comparison with previously reported experimental and clinical studies: aging effects on high order aberrations and Strehl ratio, the wavelength dependence of straylight and the ciliary corona.

The calculated phase maps by the model were displayed on a liquid crystal on silicon (LCoS) device as spatial light modulator to experimentally generate the amounts of straylight, measured by the optical integration method. Moreover, the model was incorporated in a visual simulator to evaluate the effects of straylight on the visual acuity, the contrast sensitivity and the glare sensitivity, in fovea and two eccentricities of the visual nasal field. In this way, the relationships between the amount of straylight and these measurements of the visual function were established. Furthermore, the modest benefits of the cataract surgery with preexisting retinal diseases can be explained from these measurements.

An instrument was developed for the experimental evaluation of the WS technique's performance in the correction of simulated cataracts. It simultaneously generates and corrects the effects of cataracts using a double-pass through a single LCoS device. The following process were done for the incorporation of the LCoS device: phase calibration, optimization of the phase modulation, suppression of the unmodulated light, and compensation of its inherent aberrations. Thus, the effects of three levels of cataract, with associated logarithmic amounts of straylight ranged from 1.75 to 2.25, were corrected using seven different spatial resolutions of the correcting phase maps. The quality of the correction was initially evaluated, considering one pass through the affected ocular media, by means of the following objective and subjective metrics: the enhancement of the PSF, the visual Strehl ratio, the correlation coefficients and the visual acuity. According to these measurements, the main effect of the WS technique is deblurring. Further calculations showed that the angular range of influence of the WS technique was narrow and, therefore, it did not correct the straylight. A strategy was proposed to overcome this limitation.

Finally, the developed instrument was slightly modified to evaluate the performance of the WS technique considering symmetrical and asymmetrical double-passes through the cataractous ocular media. Although the WS technique optimized the double-pass PSFs, it did not mean a benefit in the quality of vision. Therefore, some suggestions are given to obtain a visual benefit from the implementation of WS in double-pass.

1. INTRODUCTION

The human interaction with the physical world is highly dependent on the information received through the eyes, and therefore, loss of sight (or even poor vision) dramatically affects the quality of life. Because cataract is one of the main causes of visual impairments in the world[1], the research about an alternative way for its correction is of outmost importance. In this thesis, an adaptive optics technique is proposed and implemented to correct the effect of cataracts.

In this Chapter, the fundamental concepts will be discussed. In the first Section, the eye is described and modelled as an imaging system where two optical phenomena take place: aberrations and straylight. In the second Section, their impact on the visual function is described. The origin, effects, classification and current treatment of cataracts are documented in Section 1.3. Furthermore, in Section 1.4, the limitations of current adaptive optics systems and the proposed 'see-through' technique are described. Finally, the motivation, objective and outline of this thesis are presented in Section 1.5.

1.1   The eye as an imaging system

For a better understanding of the human eye, its anatomy is sketched in Figure 1-1 and briefly described below.
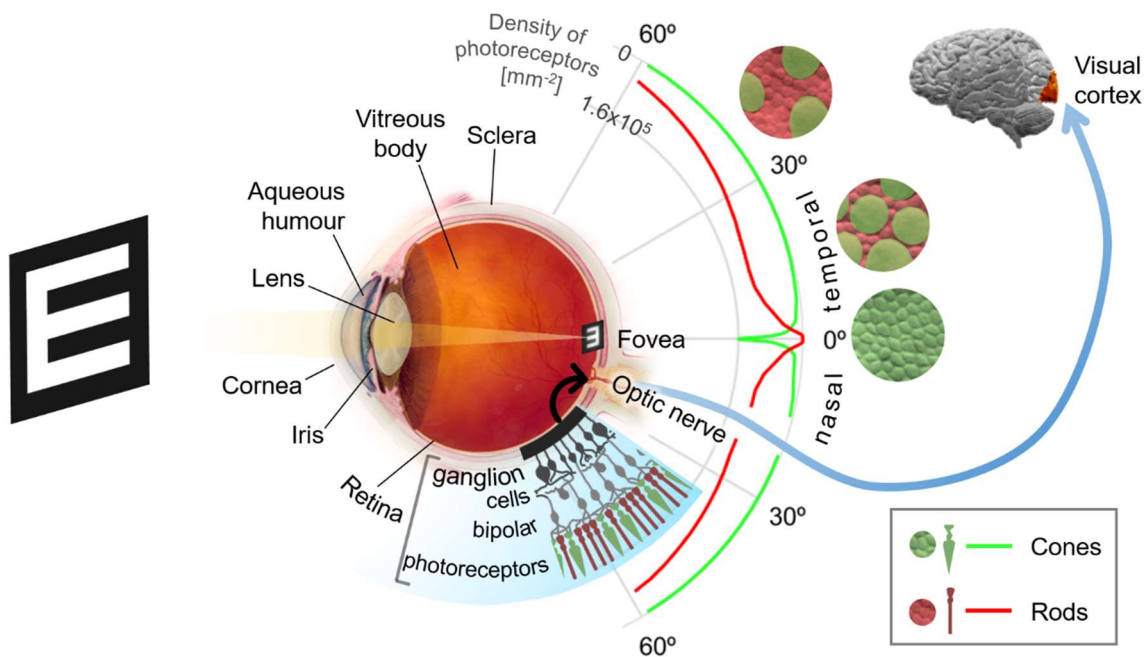
Figure 1-1. Anatomy of the human eye.

This sophisticated organ is mainly composed of two lens elements: the cornea and the crystalline lens. The cornea is a transparent meniscus shaped lens, with an outer surface curvature of about 8 mm and a central thickness of 0.5 mm, in average. Its effective refractive power is approximately 40 diopters (D)[2], being about two-thirds of the ocular

refractive power. The remaining power (20 D) is provided by the lens, a biconvex structure with a gradient refractive index profile because of its composition of fiber cells arranged in onion-like layers (so called zoned of discontinuities)[3,4]. In young eyes, the curvature of the lens is voluntarily changed to focus objects at different distances in a process called accommodation. This element is transparent in healthy eyes, becoming opaque by the cataract development (see Section 1.3). Between the cornea and lens, the pigmented iris separates the eye chambers filled by the aqueous humor and forms a circular opening acting as the pupil to regulate the amount of light to be detected in the retina.

After the lens, the light passes through the vitreous body, which is filled by a liquid with similar optical properties to the aqueous humor. Once the light reaches the retina, it travels through roughly 0.5 mm of different layers of tissue before its absorption by the photoreceptors[5]. There are two types of photoreceptors: the cones, found in the center of retina, responsible for both photopic and color vision; and rods, mainly found in the periphery, responsible for low light vision. At the central fovea, an important region for vision with high spatial resolution, cones are present in a high density and the diameter of their outer segments is reduced (see diagram in Figure 1-1). Finally, the electrical signal from the photoreceptors is transmitted to the cerebral cortex through the optic nerve, after passing through the bipolar and ganglion cells. The brain processing of the retinal image can be summarized in the neural contrast sensitivity function, which basically enhances spatial frequencies from 2 to 6 cycles per degree[6,7].

The described components of the eye do not produce an optically perfect organ. Indeed, the anatomist and physicist Hermann von Helmholtz (1692) commented[8]:

... if an optician wanted to sell me an instrument which had all these defects, I should think myself quite justified in blaming his carelessness in the strongest terms, and giving him back his instrument

However, in a less famous quote[8], the scientist recognized the importance of their 'imperfect' eyes for his quality of life.

These imperfections, at different spatial scales, reduce the quality of the retinal images. Their impact on extended images can be analyzed using the point spread function (PSF), which is the image of a point source at the infinity. In the following sub-Sections, two related optical phenomena are described, as well as, the numerical approach to reproduce their effects.

1.1.1 Aberrations

Aberrations are deviations of the ocular wavefront from a sphere. The sphere is adopted as reference because it corresponds to the surface with the identical phase of the optical field propagated from a point source through a homogeneous media. Ocular aberrations are mainly caused by the irregularities in the shape of the refractive components and the

macroscopic non-uniformities of their refractive index, although the eye has developed mechanisms to minimize them[9–11].

The primary (or Seidel) aberrations, the most significant in visual optics, are: curvature of field (also known as defocus), astigmatism, coma and spherical aberration. The amount of aberrations is quantified through the root mean squared (RMS) of the wavefront. On average, for a pupil size of 5 mm, the RMS corresponding to a healthy eye is approximately 0.25 μm. However, that value decreases with the pupil size, where diffraction becomes significant[12]. The main effect of the aberrations, understood as phase-maps with low-spatial frequencies, is the blurring of the retinal images because of the PSF's redistribution in a narrow angular range.

Ocular aberrations are currently and objectively measured using Hartmann-Shack sensors or laser ray tracing instruments[13,14]. The principle of operation of those technologies will be described in Section 4.1. The retrieved aberrations are generally expressed as a linear combination of the Zernike polynomials[15], an orthonormal basis initially used to described the aberrations produced by atmospheric turbulence[16]. These polynomials are convenient in the study of visual optics for two main reasons: first, their definition on a circular region as the eye's pupil; and secondly, a reduced number is required to represent the aberrations with the highest impact on vision[17,18]. However, Zernike polynomials are not the only way to describe aberrations; nowadays other basis have been proposed to represent the ocular wavefronts[19,20]. The convenience of the cosine functions to reproduce both aberrations and scattering effects will be shown in Section 2.1.

Additionally, the wavelength dependence of the refractive index of the ocular components is the source of the chromatic aberrations. In consequence, both defocus and lateral position of retinal images change with wavelength[21]. Throughout this thesis, the term aberrations will be referred only to the monochromatic ones.

1.1.2   Straylight

The term 'straylight' refers to the intraocular scattered light. It is mainly caused by the interaction of light with significantly smaller features of the cornea and the lens, such as cell nuclei and protein aggregates, because of the local variations of refractive index. While the amount of scattered light supplied by the cornea is approximately constant with age[22], the contribution of the lens increases with age or the cataract development[23]. The iris and sclera are not completely opaque, and the light transmitted through them reaches chaotically the retina[24]. Lastly, the fundus does not absorb all light that reaches the retina; part of the light is reflected and scattered towards other retinal locations[25]. The amount of straylight from the iris, sclera and fundus depends on the pigmentation, being higher in light eyes than in dark ones. Figure 1-2 shows the interaction mechanisms of the light that originate the straylight in the eye.
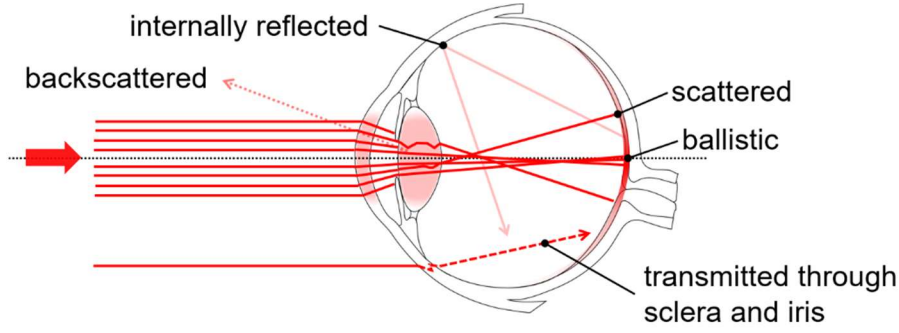
Figure 1-2. Interaction of the light with the sources of intraocular scattering.

The light that interacted with the cornea and lens can be classified as: ballistic (governed by refraction), scattered and backscattered. While scattered light interacts with microstructures with a size comparable or bigger to the protein aggregates, backscattered light is produced by small sized proteins (with typical radius of 10nm) and the zones of discontinuities of the lens with high reflectivity[26]. Currently, the amount of backscattered light is objectively and subjectively assessed to indirectly evaluate the impact of the straylight on the quality of vision[27]. However, forward scattering determines the functional effect of straylight in vision, reducing the contrast of the retinal images.

The effects of the forward scattering on the radially averaged ocular wide-angle PSF were initially modelled as a power law (power -2) of the retinal angle within its domain (i.e., for angles larger than one degree)[28]. The first and simplest version of the PSF formulation as function of the age (A) was the Stiles-Holladay equation[29]:

$$PSF(\theta) = \left[1 + \left(\frac{A}{70}\right)^4\right]\frac{10}{\theta^2} \quad (1\text{-}1)$$

where θ is the retinal angle in degrees. It has a validity domain between 3 and 30 degrees.

Further studies were conducted to include the effects of the pigmentation and to extend the validity domain, increasing the complexity of the ocular PSF formulations[30,31]. They were based on psychophysical data, in-vitro measurements and analytical descriptions. The equation of the PSF for the standard observer, documented by the *Commission Internationale de l'éclairage* (CIE)[32], usable in the whole angular range is given by:

$$
\begin{aligned}
PSF_{CIE}(\theta) =\ & \left[1 - 0.08\left(\frac{A}{70}\right)^4\right]\left[\frac{9.2\times10^6}{[1+(\theta/0.0046)^2]^{1.5}} + \frac{1.5\times10^5}{[1+(\theta/0.045)^2]^{1.5}}\right] \\
& + \left[1 - 1.6\left(\frac{A}{70}\right)^4\right]\left\{\left[\frac{400}{1+(\theta/0.1)^2} + 3\times10^{-8}\theta^2\right]\cdot \right. \\
& \left. + p\left[\frac{1300}{[1+(\theta/0.1)^2]^{1.5}} + \frac{0.8}{[1+(\theta/0.1)^2]^{0.5}}\right]\right\} + 2.5\times10^{-3}p
\end{aligned}
\quad (1\text{-}2)
$$

where p is a pigmentation coefficient that equals to 0, 0.5 and 1 for black, brown and light eyes respectively. The units of the PSF_{CIE} are inverse of steradians (sr^{-1}), i.e. it is

normalized to the solid angle covered by the light propagation. Some examples of the PSF_{CIE} for two different ages are shown in Figure 1-3a.
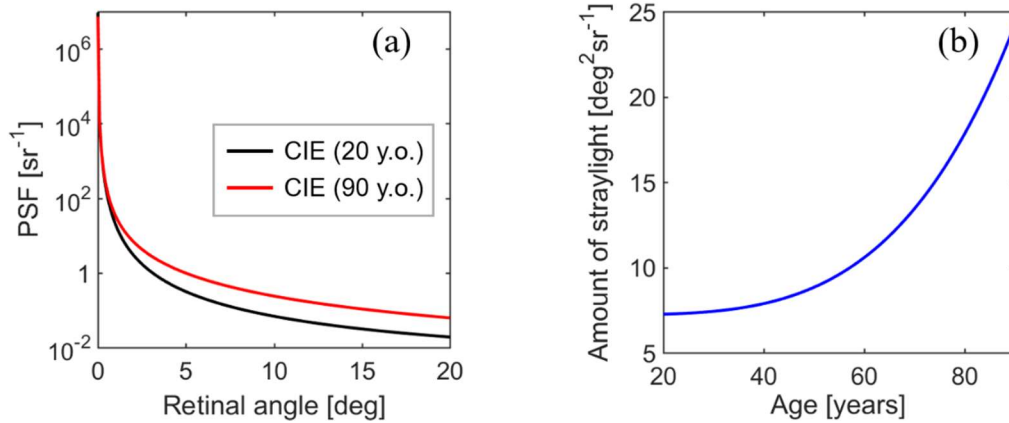
Figure 1-3. Aging effects on: (a) the PSF of the CIE standard observer and (b) the amount of straylight at six degrees.

The amount of straylight is quantified by the straylight parameter (s) defined as $\theta^2 PSF(\theta)$. The logarithm of the s parameter is commonly used. The aging effects on the straylight parameter at six degrees (for light eyes) is depicted in Figure 1-3b, according to the Equation 1-2.

Regarding the size of the scatterers, there are two analytical approaches to study the scattering: Mie and Rayleigh regimes. The Mie regime is applicable to scatterers with size comparable to the wavelength or bigger, and shows no wavelength dependence[33]. It was previously applied to reproduce the effects of the intraocular scattering[34,35]. On the other hand, the Rayleigh regime is useful to describe the scattering of particles smaller than a tenth of the wavelength, approximately[36]. In this case, the deviation angle is highly dependent on wavelength following a power law function (power -4). This approach was used to explain the wavelength dependence of the intraocular straylight in well-pigmented eyes[37]. In this thesis, an alternative approach is adopted to reproduce the effects of the intraocular scattering, which is based on Fourier optics.

1.1.3 Description using Fourier optics

In a simplified description of imaging, objects are projected and focused on the retina by a single-lens located in the pupil. This lens has a refractive power ($1/f$, where f is the focal length) of 60 D, adding the optical power contributions of both cornea and lens for far vision. The phase map of the lens is composed of the spherical wavefront, representing a perfect shaped lens, and a thin phase screen W to incorporate the effects of both aberrations and intraocular scattering. Moreover, the lens has a circular aperture with diameter ϕ.

According to the Fourier optics theory, for monochromatic (wavelength λ) and spatially incoherent illumination, the response of a linear optical system to an arbitrary

input O (i.e., an extended object) is the sum of the PSFs from every bright point at the input plane[38]. The system is assumed shift invariant for simplification. This means that the PSF generated by the modelled lens is independent of the input's position. Thus, following the notation shown in Figure 1-4, the image I is the convolution of the object and the PSF:

$$I(x',y') = \iint_{-\infty}^{\infty} O(x,y)PSF(x'-x, y'-y)dxdy \quad (1\text{-}3)$$

Since we are interested in far vision (i.e., the object is located at the 'infinity'), the PSF at the focal plane becomes independent of the input coordinates and it is giving by the following formula:

$$PSF(x',y') = \left| \frac{1}{\lambda f} \iint_{-\infty}^{\infty} P(\xi,\eta)\exp\left[-i\frac{2\pi}{\lambda f}(x'x + y'y)\right]dxdy \right|^2 \quad (1\text{-}4)$$

where $P(\xi,\eta) = circ(\xi,\eta)\exp[iW(\xi,\eta)]$ is the complex pupil function with aperture function $circ()$, valued 1 for $\sqrt{x^2 + y^2} < 0.5\phi$ and zero otherwise.

Numerically, the PSF is calculated by applying the Fast Fourier Transform (FFT) to the complex matrix of the pupil function[39]. A zero padding is applied to double the size of the pupil matrix, improving the sampling on the PSF[40]. The angular size of a pixel in the PSF matrix is equal to $0.5\lambda/\phi$ (in radians).

To compare the numerical PSFs with the PSF_{CIE} (Equation 1-2), the numerical PSFs must be normalized over the solid angle Ω:

$$\alpha \sum_{\Omega} PSF\Delta\Omega = 1 \quad (1\text{-}5)$$

where α is a normalization factor and $\Delta\Omega$ is the subtended solid angle in each square pixel of the PSF matrix, which is equivalent to $0.25\lambda^2/\phi^2$.

Finally, the normalization factor is:

$$\alpha = \left[0.25\frac{\lambda^2}{\phi^2}\sum PSF\right]^{-1} \quad (1\text{-}6)$$
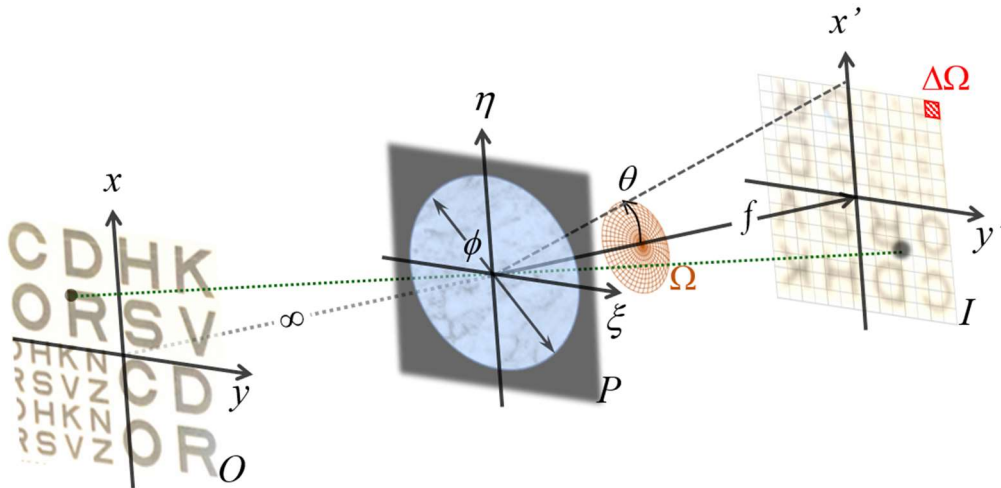
Figure 1-4. Schematic diagram of the image-formation process.

1.2 Evaluation of the visual function

Several psychophysical tests have been developed to evaluate the eye and the visual system. The simplest and widely used test is measuring the visual acuity (VA), that provides an estimation of the spatial resolution, i.e., the minimum size of the stimulus that the visual system can resolve[41]. In a healthy observer, the minimum angle of resolution (MAR) is usually expected around 1 minute of arc (arcmin). VA is mainly affected by the aberrations and intraocular scattering. Apart from the size, the contrast of the stimulus is another important aspect in the vision, which quantifies its relative difference in luminance from the background[42]. It can be calculated on periodic and non-periodic stimuli using the Michelson or Weber formalisms, respectively. The amount of contrast that a person needs to see a stimulus with a given spatial frequency is defined as the contrast threshold, and its inverse is known as the contrast sensitivity (CS). While aberrations decrease the CS values at higher spatial frequencies, straylight reduces the CS values for all spatial frequencies[25] by superimposing a veil of light originating from the brighter parts of the image. The methodologies used to assess VA and CS throughout this thesis will be described in each case.

1.3 Cataracts

Cataract is a common pathology related to the elevated amount of straylight that causes a significant impairment of vision. It is mainly due to oxidative damage to lens proteins, especially to the α-crystallin molecules[43]. Proteins are well folded in their native state, however, they become misfolded because of oxidation, forming protein aggregates with different optical properties of the original molecule[44]. For example, the aggregates have the appropriate size to directly scatter light[45]. Although the lens has mechanisms to repair or remove the damaged proteins, they degrade with age, leading to a progressive increase of lens's turbidity. Such increase can be accelerated by metabolic disorders, genetic predisposition, certain diseases (e.g., diabetes), exposure to ultraviolet light, among others risk factors[46].
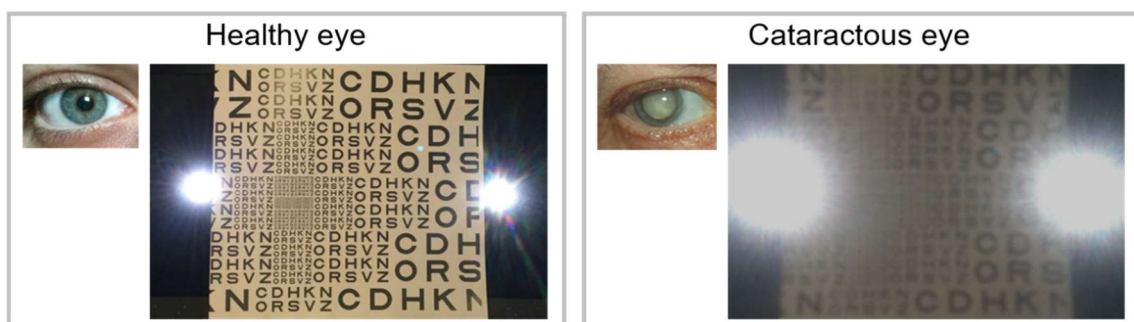
Figure 1-5. Effects of cataracts on a scene with two incorporated glare sources.

Cataract development also involves an increase of aberrations[47–52]. Therefore, its effects are both the blurring of the retinal image and the reduction in its contrast, as

depicted in Figure 1-5. The impact on the quality of vision can be assessed by the reduction of visual acuity[53] and contrast sensitivity[54–56], being strongest in the latter[57–59].

1.3.1 Classification

Cataracts are graded through the amount of backward scattering. By this modality, the classification is entirely subjective (e.g., using the Lens Opacity Classification System LOCS-III[27]) or numerically assisted (e.g., using the Wisconsin System[60]) when the pupil is illuminated with a slit lamp. Other advanced instruments, such as lens opacity meters[61] and the Scheimpflug photography[62], can objectively assess the physical properties of the opacities. Throughout this thesis, the cataracts states are referred to their equivalent LCOS-III grade, because it is widely used in clinical studies. According to this system, cataracts are initially classified depending on the location of the opacities as: nuclear, cortical, and posterior. Successively, for each localization, the opacification's severity is ranked from 0 to 5 (for cortical and posterior subcapsular cataracts) and from 0 to 6 (for nuclear cataracts).

On the other hand, the amount of forward straylight (or s) can be psychophysically and objectively measured. Psychophysically, the compensation comparison method[25] or the differential contrast test[63–65] allows the direct estimation of the s parameter. Objectively, s is valued applying the optical integration method[66–68] or analyzing the aerial retinal images[69]. Several studies have been conducted to assess the correlations between the amount of straylight (objective or subjective) with the above-referred grading systems[70–73].

1.3.2 Current treatment

The current treatment for this pathology is the cataract surgery, which has been practiced at least since the ancient Egypt[74]. The early technique consists of couching the affected lens into the vitreous cavity. Since then, two significant milestones have been achieved. First, the invention of the cataract extraction surgery in 1747. Second, the correction of the aphakia with intraocular lenses (IOLs), implanted for the first time in 1950. In the last decades, tremendous improvements of the technique have allowed to reduce the pain, the rate of complications and the recovery periods. Despite those progress, cataract remains the leading cause of visual impairment in the world, except for developed countries[1]. Therefore, cataracts are generally untreated or rudimentary techniques (e.g., couching) are still being practiced[75,76] in the countries where the majority of the affected population live[77].

Cataract surgery, as an invasive procedure, poses possible side effects, such as: corneal edema, increase of intraocular pressure, infection, uveitis, retinal detachment, among others[78]. Moreover, the intraocular straylight could increase after the surgery because the posterior capsular opacification, where a hazy layer of migrated cells is

formed between the capsule and the IOL[79]. Those complications would be avoided by using a purely optical approach for correction.

1.4 Adaptive optics for cataracts compensation

Adaptive optics (AO) systems have been used to improve the quality of vision[80] and to study the neural system's response when the ocular aberrations are manipulated[81,82]. Those systems are composed by two coupled stages: measurement the ocular aberrations, using a wavefront sensor; and their correction, carried out by a spatial light modulator (SLM). However, current AO systems cannot be widely applied to cataractous eyes because the limitations in the performance of the wavefront sensors. The wavefront shaping (WS) technique has been applied to retrieve the imaging through turbid media and, therefore, is proposed to overcome those limitations.

1.4.1 Limits of the current wavefront sensors

Hartmann-Shack (HS) sensors has been used to measure the ocular aberrations[83] and successfully incorporated into AO systems[84]. The HS sensors primarily consists of a camera placed at the focal plane of a lenslet array. The local slopes of the incoming wavefront are calculated as the ratio between the position shifting of the focal points and the focal length of the lenslet. In order to estimate the aberrations, a narrow laser beam is projected into the eye and the backscattered light from the retina, passing through the eye's optics again, being collected by the HS sensor by conjugating its lenslet array with the eye's exit pupil. Hence, HS sensors allows to measure the ocular aberrations in an extended population even with refractive disorders[85,86].

HS sensors have been used in eyes with early and mild cataracts[47,48,87,88], however, their performance decreases when the opacity increases[50]. The typical maximum grades of the examined eyes with cortical and nuclear cataracts were 3 and 4 in the LOCS-III scale, respectively. It corresponds to amounts of straylight ($Log_{10}[s]$) less than 2 in the case of the nuclear cataract[70]. The origin of the limitation is the inability to locate the focal spots because the HS patterns are affected by both blurring and contrast reduction as consequence of the spread light in the lens opacities. In fact, this degradation of the quality of spots has been proposed as a method to assess the local opacities at the exit pupil of the eye[89].

On the other hand, laser ray-tracing (LRT) is another technique that uses the rapid projection of narrow laser beams, parallels to the line of sight, into particular locations of the pupil where the local aberrations produce the lateral displacement of each beam on the retina[90]. The displacements are estimated capturing the retro-reflected light with a position sensitive detector. Cataractous eyes have been also evaluated using this technique[51,91,92]. However, those measurements are limited as well by the reduced quality of the laser beams when early and mild cataract (with equivalent $Log_{10}[s]$ values less than 2) are measured.

1.4.2   Wavefront shaping

When a scattering lens (composed by a transparent lens and scattering layer) is illuminated by a coherent beam, the PSF corresponds to a speckle pattern, as shown in Figure 1-6. Speckle is the result of the constructive or destructive interference among the field's contributions from every point in the scattering lens's pupil to each spatial position on the observation plane. If the pupil is discretized in regular segments, the resulting field at one position of the PSF (i.e., the target) can be easily understood using a phasorial representation. Figure 1-6 depicts the summation of the field's components with random phases.

WS technique allows to increase the energy at the target, associated to the length of the resulting phasor, by manipulating the amplitude or the phase of the incident beam to the scattering lens. In the case of the amplitude manipulation, the energy's enhancement is achieved darkening the segments that provide phasors in the opposite direction to the total phasor[93]. In the case of the phase manipulation, the phase of each segment is changed from 0 to 2π radians, rotating the corresponding phasor until it is aligned with the resulting phasor[94] (see in Figure 1-6). For the same number of segments, the magnitude of the optimized phasor is higher when the phase is manipulated instead of the amplitude and therefore phase modulation was used in the experiments performed in this thesis.
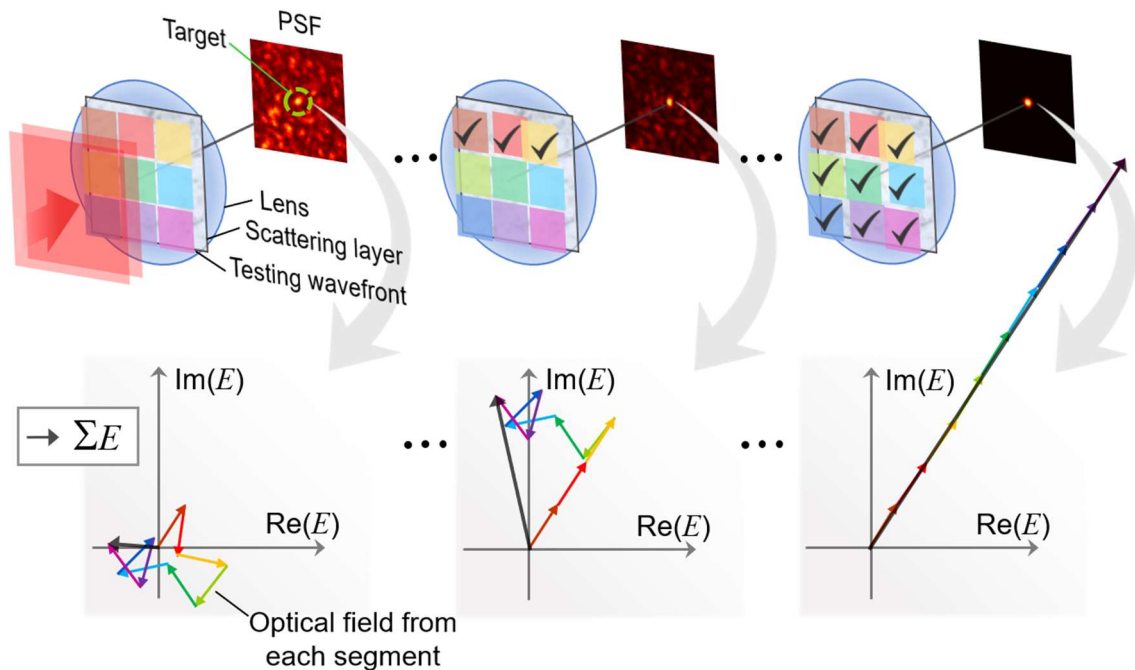
Figure 1-6. Principle of WS technique using phase modulation. The result of the optimization is the increase of the magnitude of the total optical field at the target, represented in the complex plane (down).

Several optimization algorithms have been developed for the WS implementation[95,96]: sequential (stepwise and continuous), partitioning and genetics. They are differentiated by their complexity and required iterations to optimize the PSF. However, the achievable

PSF's enhancement, i.e. the ratio between the optimized intensity at target and the initial average of intensity around that position, is the same for all algorithms because it exclusively depends on the number of segments.

The WS technique was firstly demonstrated by Vellekoop *et al.*[94] and, since then, it has been applied in several fields, such as: imaging through turbid medias[97], microscopy[98], optical coherence tomography[99], endoscopy[100], among others.

1.4.3 Spatial light modulators

The correction of scattering using WS requires SLMs with high spatial resolution. In this thesis, a Liquid Crystal on Silicon (LCoS) device was used as SLM to reproduce and correct the intraocular scattering. The feasibility of this kind of device to correct the ocular aberrations has been previously demonstrated[101]. The main advantages of this device are the relative low cost and easy operation. On the other hand, as potential drawbacks, the optical properties of the liquid crystal depend on the wavelength and the polarization.

The LCoS device is a reflective micro-display with millions of independent pixels with typical sizes of several microns. Each pixel or cell is basically composed of parallel aligned molecules of nematic liquid crystal between two electrodes[102]. The user can address 256 voltages to each pixel using the 8-bits gray levels in a video card of a computer, changing the birefringence of the liquid crystal by the rotation of their molecules towards the direction of the electric field, as shown in Figure 1-7. This kind of devices requires a phase calibration before its operation, which is the linearization of the phase modulation (between 0 and 2π radians) as function of the gray levels by the proper configuration of the LCoS driver. This procedure is explained in Appendix A.
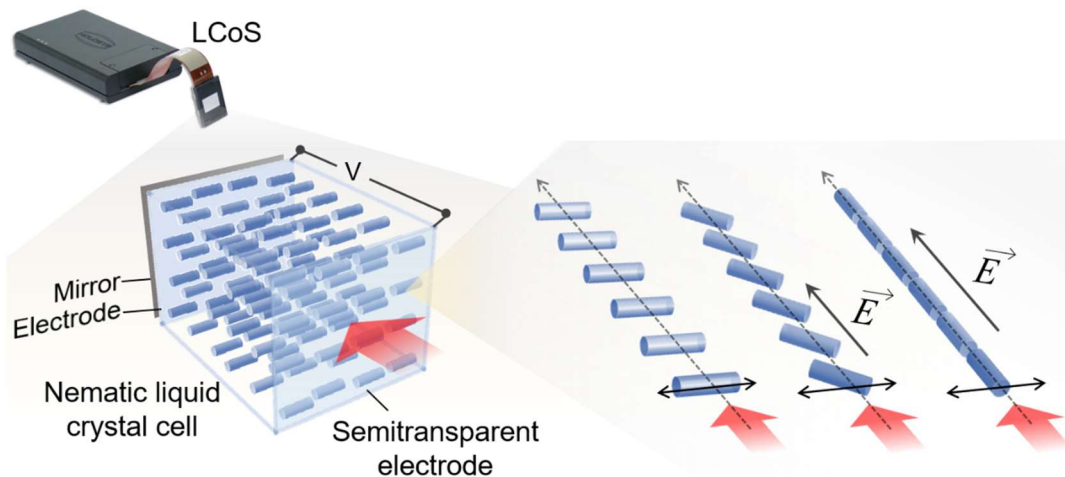
Figure 1-7. Basic composition of the LCoS display, showing the effects of the electric field (produced by the voltage V) on the rotation of the molecules of nematic liquid crystal.

Additionally, a Digital Micromirror Device (DMD) was used for image projection, operated in amplitude-only modulation. DMDs consist of segmented mirrors on micro-electromechanical systems (MEMS), which reflect the incoming light in two angles (±12

degrees) as binary states. The deviated light that follows the prepared path in the experiment is 'on' and the missed (or blocked) light is 'off', providing high-contrast stimulus. The main advantages of this kind of devices are: the low cost, their performance is independent of the polarization state, and the remarkable high frame rate compared to the liquid crystal modulators. Those devices have been also programmed as phase-modulators using the Lee method[103,104], however, the diffraction efficiency of the generated phase elements is drastically reduced.

Other class of SLMs used in AO systems are the deformable mirrors (DM), which are composed by a reflective surface whose shape is controlled by an array of actuators. The main advantages of the DMs are the high reflectance, achromaticity, and very high control speed[105]. Early DMs had a small number of segments, which were enough to correct low spatial frequencies phase perturbations (e.g., the ocular aberrations[106]). However, the invention of DMs based on MEMS[107] allows their application for scattering compensation in microscopy[108]. The latter can locally manipulate the phase delay using thousands of piston-type actuators covered by a segmented reflective membrane. Their current cost is high compared to that of LCoS or DMD devices.

1.5 Motivation and outline of the thesis

The requirements for the safety practice of the cataract surgery (facilities, specialized professionals and the IOL) have not allowed to cover the global demand. Therefore, a non-invasive correcting technique would be beneficial and its development is an open challenge whose unique precedent was reported forty-five years ago[109]. In that experiment, the phase of the extracted lens was retrieved using holography for its posterior phase conjugation. Figure 1-8 shows the effects of the achieved correction on an USAF test as object. Nonetheless, this approach is impractical for a *in vivo* implementation due to the requirements of the holographic setups.

Uncorrected   Corrected
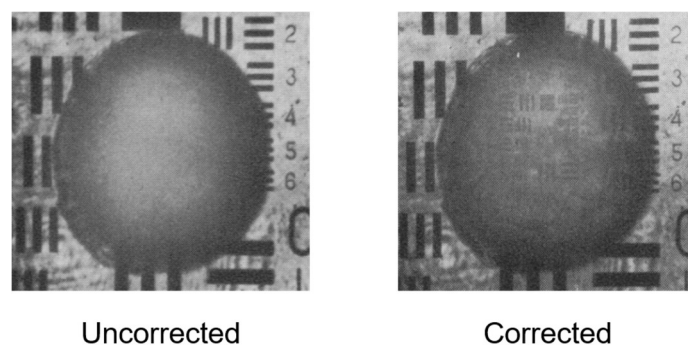
Figure 1-8. An USAF test seen through the uncorrected and corrected excised cataractous lens. (Source: adapted from Miller *et al.*).

In this thesis, a solution based on the WS technique is proposed for the *in-vivo* correction of cataracts. Hence, the main objective is to evaluate the benefits that WS technique can offer in this application. Because fine spatial perturbations of the ocular wavefront are manipulated during the correction, *in-vivo* evaluation would be

simultaneously influenced by several factors such as tear film stability[110], eye movements[111], accommodation (depending of the age[112]), among others. Therefore, an evaluation in an optical bench is more convenient to recognize the benefits offered by the technique and their comparison when several cataracts levels are considered.

The evaluation of the WS performance for the correction of the simulated effects of cataracts is described as follows. The first activity was the development of a phase perturbation model to realistically replicate the effects of programmable amounts of straylight (Chapter 2). The generated phase maps were incorporated in a visual simulator to assess the impact of artificially induced straylight on the visual function (Chapter 3). Moreover, an experimental setup was made for the simultaneous artificial generation of intraocular straylight and the WS implementation (Chapter 4). The performance of the WS technique was initially evaluated for the correction of the effect of different cataract states considering a single-pass of the light through the ocular media (Chapter 5). Under that assumption, those results were considered as the highest expected performance. Finally, the performance was evaluated in the double-pass setup (Chapter 6), producing several suggestions towards a feasible *in-vivo* implementation.

2. GENERATION OF THE OCULAR POINT SPREAD FUNCTION USING RANDOM PHASE PERTURBATIONS

A first step to achieve the general aim of this thesis is to implement a methodology for generating different amounts of intraocular straylight in a control way. Several approaches have been proposed to reproduce the ocular PSF incorporating the effects of the intraocular scattering. The first model[113] replicated an empirical ocular PSF with a Gaussian diffuser inserted in a schematic eye with aspheric surfaces. Afterwards, the scattering sources were simplified to micro spheres analyzing the forward light distribution from donor lenses[114,115]. However, the assumption that ocular scatterers are represented by a distribution of single sized particles is not completely realistic because its generated PSF differs from the CIE glare function[34]. On the other hand, a variable diffuser based on a polymer dispersive liquid crystal was used as part of a physical eye model with controllable scattering[116], however, there was no a quantitative assessment of the generated amounts of straylight. In addition, Black Pro-Mist filters (BPM; The Tiffen Company, NY), originally designed for decreasing the contrast and sharpness in professional photography, are commonly considered as a reference in the estimation and production of typical amounts of intraocular straylight to certain angles[66,117–119]. The current approaches are not sufficiently accurate to reproduce the straylight influence on the PSF at its whole angular domain.

In this Chapter, intraocular straylight is reproduced by a random phase screen located at the pupil plane. The wavefronts of the screen correspond to pseudo self-replicant surfaces, which are calculated from the weighted combination of phase perturbations with different spatial frequencies [68]. Furthermore, the amount of straylight can be controlled through the wavefront amplitude[120]. Nevertheless, a model based on this kind of random surfaces requires a complete definition of its parameters. Thus, in the first Section, the parametrization of the model is explained, and its optimization is conducted to reproduce the intraocular scattering component of the ocular PSF suggested by the CIE. In the second Section, the model is extended to reproduce the whole angular range of the PSF by including phase maps with lower spatial frequencies. The validity of the methodology is demonstrated through the calculation of optical metrics and their comparison to reported clinical and experimental data.

2.1 Reproduction of the intraocular scattering

A new methodology was developed for the calculation of phase maps (W) whose angular distribution of their diffraction patterns mimics the intraocular straylight. The model is based on the parametrization of the discrete cosine spectrum of W. Thus, W will be

composed of cosine modes, i.e. oscillating wavefronts with defined spatial horizontal (f_j) and vertical (f_i) frequencies.

The calculus of the discrete cosine spectrum of W is the modulation of the standard normally distributed random values in the matrix R by the surface contained in the matrix U, as depicted in Figure 2-1. Then, W is obtained by applying the Inverse Discrete Cosine Transform (IDCT) to the element-wise multiplication between U and R. Mathematically:

$$W_{i',j'} = circ(i',j') \sum_{i=0}^{N-1} \sum_{j=0}^{N-1} U_{ij} R_{ij} \cos\left(\frac{\pi \phi f_i}{N} i'\right) \cos\left(\frac{\pi \phi f_j}{N} j'\right) \quad (2\text{-}1)$$

where N is the dimension of matrices and $circ(\ )$ is the aperture function, valued 1 for $2\sqrt{(i' - 0.5N)^2 + (j' - 0.5N)^2} \leq N$ and zero otherwise, acting as iris with diameter ϕ. Each set of values in R differentiates the information of individual eyes, allowing to simulate populations with alike characteristics.
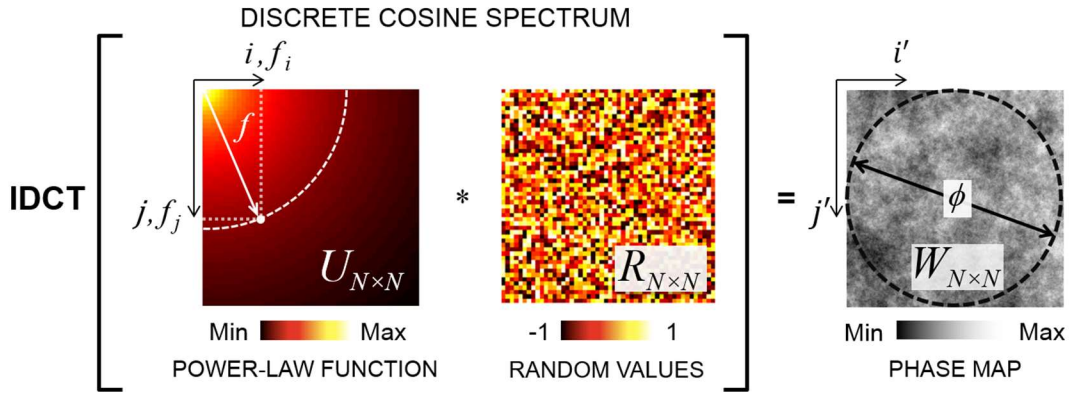
Figure 2-1. Procedure for calculation of phase maps.

Each position (i,j) in the spectrum is associated to a bidimensional cosine oscillation in the spatial domain (i',j') with single vertical $f_i = \left(i + \frac{1}{2}\right)/\phi$ and horizontal $f_j = \left(j + \frac{1}{2}\right)/\phi$ frequencies. In this way, the wavefront is the sum of all cosine modes where the amplitude of each mode is related to the fraction of the incoming energy into the eye directed to a specific angular position of the PSF.

The modulating matrix U is calculated using a power-law function applied on the radial frequency $f = \sqrt{f_i^2 + f_j^2}$:

$$F(f) = Bf^{\beta} \quad (2\text{-}2)$$

where B and β are the model parameters. While β controls the relative weighting of the modes (i.e., the energy distribution between small and large angles in the PSF), B controls the root mean square (RMS) amplitude of the wavefront. Therefore, B also controls the straylight amount, due to the linear relationship between logarithmic values of the root mean squared (RMS) and the straylight parameter[121]. For further calculations, the units of spatial frequency are cycles per millimeter.

For each set of parameters (B,β), the normalized PSF was numerically calculated as the monochromatic diffraction pattern produced by the W through the Fourier transform.

The particular (B,β) couple that reproduces the angular distribution of the ocular straylight was found by an optimization procedure that minimizes the RMS difference between the logarithmic values of the calculated PSF and empirical PSF_{CIE} (Equation 1.2). This procedure was implemented using the *fminunc*() function in MATLAB (MathWorks, Natick, MA, USA), which is based on the quasi-Newton method[122].

The model performance was demonstrated replicating the features of the experimental setup described in Chapter 3: resolution of W matrix ($N\equiv1001$ pixels), pupil size ($\phi\equiv1.33$mm) and wavelength (λ=540 nm). Initially B and β values are optimized for representing the PSF of a young eye, i.e. assuming $A\equiv30$ in the Equation 1.2. Afterwards, the amount of straylight is evaluated for several B values to estimate the relationship between them. The random values in R are preserved in this process.

Thus, the optimized values of B (9.21 μm) and β (-1.21) produce the phase map shown in Figure 2-2a. This β value classifies the estimated wavefront as pink noise which is a common feature in physical and biological systems[123] and, particularly, it was employed for the scattering description of biological tissues[124]. This kind of wavefronts simultaneously represents the phase perturbations due to high-order Zernike aberrations and the typical intraocular scatterers such as cell nuclei, mithocondrias, organelles and protein aggregates. This feature allows the continuous replication of the scattering effects on the ocular PSF along wide angular range according to the CIE reference for 30 years old eye, as depicted in Figure 2-2b.
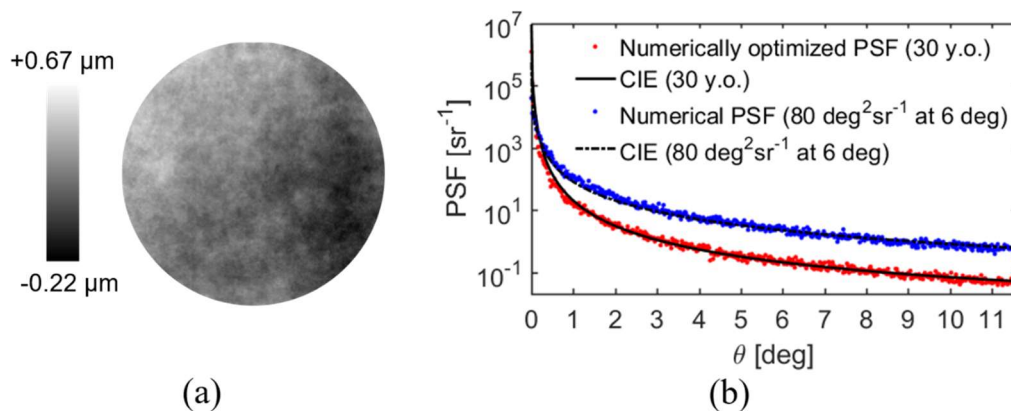
Figure 2-2. Results of numerical optimization: a) optimized phase map and b) angular average of numerical PSFs (dots) compared with the CIE reference (black lines).

Figure 2-3 shows the relationship between the amounts of straylight at six degrees and the RMS amplitude of the wavefronts for several B values. The amount of straylight can be reproduced in a simple way after a single optimization process has been performed. Figure 2-2b includes the comparison between the PSF_{CIE} with a straylight amount of

80 degree^{2}sr^{-1} (at six degrees) and the calculated PSF with the *B* value (32.62 μm) that generates the same straylight, according to the previously found relationship.
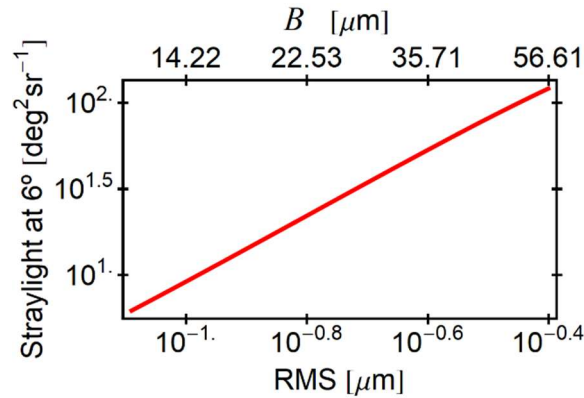
Figure 2-3. Relationship between straylight at six degrees and RMS amplitude.

The results support the robustness of the numerical model replicating intraocular straylight, i.e. the ocular PSF at large angles. However, the model will be adjusted using high resolution *W* matrices to include the effects of phase maps with lower spatial frequencies.

2.2 Complete reproduction of the ocular PSFs

In this Section, large pupils are simulated to reproduce ocular PSFs using higher resolution matrices than the previously considered ones. Therefore, the new values for *N* and ϕ are 4001 pixels and 4 mm, respectively.

Initially, the (*B*,β) parameters of the previously introduced *F* function (see Equation 2-2) were optimized to represent a young and healthy eye (i.e., $A \equiv 30$ in Equation 1-2). Figure 2-4a shows the optimized modulating function with *B*=9.21μm and β=-1.21, the same obtained values for a smaller pupil. Optimized PSF and the PSF_{CIE} are compared in Figure 2-4b, where the lack of agreement at lower angles is evident. It means that the power law function does not allow to reproduce both aberrations (understood as phase perturbations of low spatial frequencies) and scattering effects. Hence, a numerical strategy was implemented to find a proper function that mimics the ocular PSF in the whole angular range. The new modulating function is the linear interpolation of ten values logarithmically spaced in the frequency range. Those values are tuned in an optimization process to reduce the RMS error between calculated and reference PSFs. The initial values for that process were taken from the previously optimized power law function. The *fminunc()* function was applied anew. The optimized profile of the function and the PSF are shown in Figure 2-4a and 2-4b, respectively.
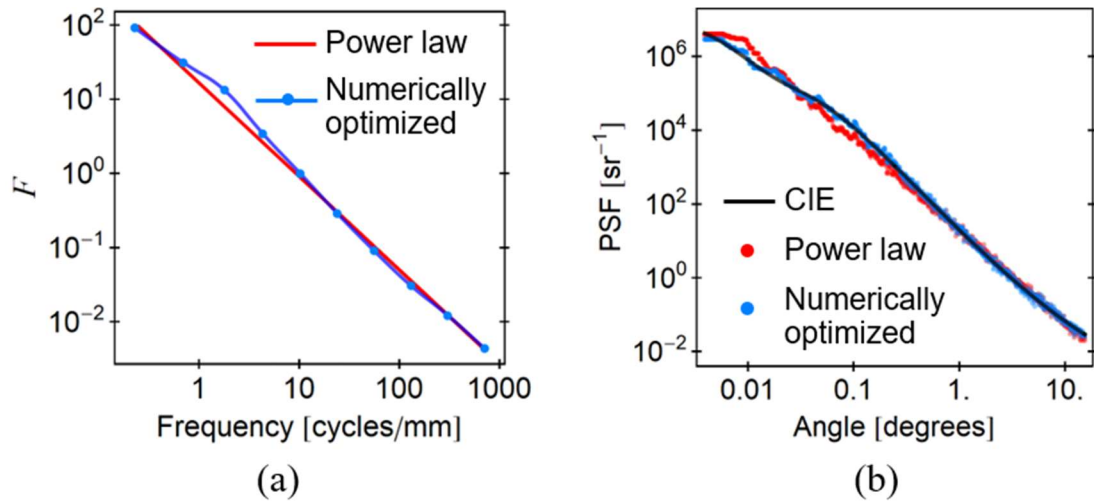
Figure 2-4. (a) Profiles of the modulating functions and (b) examples of their generated PSFs.

The relationship between the generated amount of straylight at six degrees (s) and the amplitude of the calculated W wavefronts is calculated through the multiplication of the optimized F function by the α parameter. As shown in Figure 2-3, for the new formulation of F, the relationship between the logarithm of s and the α values is linear too:

$$\text{Log}_{10}s = 0.424\text{Log}_{10}\alpha + 0.801 \quad (2\text{-}3)$$

Apart from the improvement of the agreement between the numerical PSF and the CIE reference (see Figure 2-4b), the validity of both the methodology and the modified function for the generation of realistic ocular wavefronts is evaluated through the reproduction of the aging effects on the amplitude of high order (HO) aberrations and the Strehl ratio (SR), the wavelength dependence of the straylight, and the ciliary corona.

2.2.1 Aging effects on HO RMS

Aging increases the amplitude of HO aberrations[125]. Applegate *et al.*[12] calculated the statistical relationships among HO RMS, age and pupil size on a population of healthy eyes using . The ocular wavefronts were measured using a Hartman-Shack sensor and fitted to Zernike polynomials up to the 10th radial order, but only the coefficients up to 6th radial order were analyzed[15]. Figure 2-5 depicts the statistics of HO RMS as function of the age for a pupil size of 4 mm.

To replicate this aging effect with the developed model, the amount of straylight associated to ages ranged from 20 to 90 years is calculated from the relationship plotted in Figure 1-3b. The α values that generates those amounts of scattering are estimated using the Equation 2-3. For each α value, thirty wavefronts were calculated using different random R matrices in the Equation 2-1, simulating a population of thirty eyes. The wavefronts were fitted up to the 6th radial order using the *ZernikeCalc*() function, which is based on least-squarest method[126].Thus, the RMS of HO aberrations was calculated as the root-mean-square of the resulting Zernike coefficients from 4th to 6th radial order. The

statistics of the calculated HO RMS values are plotted in Figure 2-5 for comparison with the clinical data.
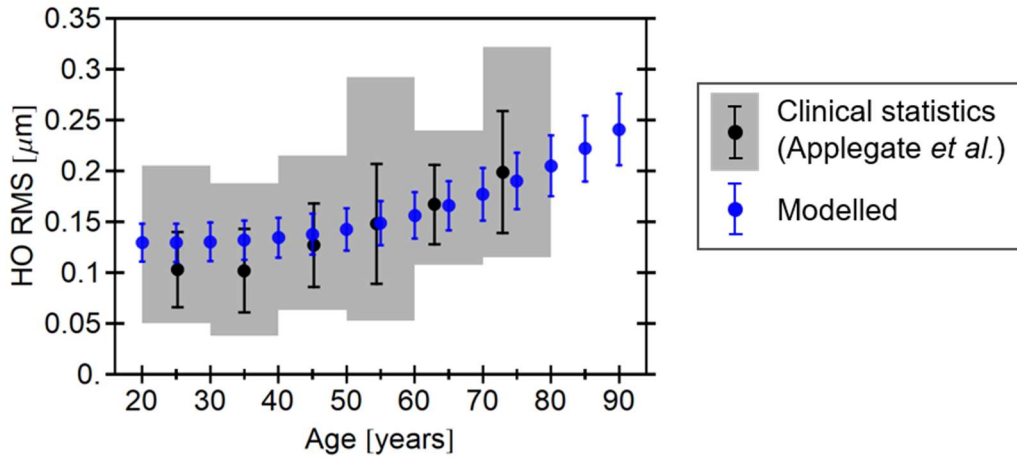
Figure 2-5. Aging effects on HO RMS. Points and bars represent mean and standard deviation values, respectively. Gray region shows the maximum and minimum clinical HO RMS.

The model provides HO RMS values within the standard deviation of the previously reported data. Although the numerical mean values are slightly higher than the clinical ones for ages less than 50 years, their differences become small with the increase of the clinical HO RMS values after 45 years. The modelling of the aging effect on the aberrations mainly based on scattering stablishes a link between both phenomena traditionally studied separately.

2.2.2 Aging effects on Strehl Ratio

SR is a basic metric of the image quality. It is usually computed in the frequency domain as the ratio of areas under the radial average modulation transfer functions (MTF) of the evaluated eye (MTF_{eye}) and an aberration-free optical system with the same aperture (MTF_{dl})[127]:

$$SR = \frac{\int_0^{f_{cutoff}} MTF_{eye}(f)df}{\int_0^{f_{cutoff}} MTF_{dl}(f)df} \qquad (2\text{-}4)$$

being the MTF calculated as the modulus of the Fourier transform of the PSF[38].

Aging reduce the SR as consequence of the increase of ocular aberrations, as it was shown previously. Guirao et al.[128] experimentally measured the aging effects on MTF using the double-pass technique[129]. In this method, the ocular PSF is recorded as the reflection of a projected point source in the retina after a double-pass through the ocular media. Those results were sorted the results in three categories according to age, as shown in Figure 2-6. Recently, Martinez-Roda et al.[130] reported a negative correlation between age and SR as a result of a clinical study using a commercial instrument based on the same technique. Figure 2-6 shows the statistics of the SR values for each age group. Defocus and astigmatism for each subject were corrected in the clinical and experimental

studies, focusing the analysis on the HO aberrations. Likewise, artificial pupils of 4 mm were used in both kind of measurements.

For comparison, the SR was estimated using the calculated wavefronts from the previous numerical calculation where aging effects on HO RMS were reproduced. SR was also computed in the frequency domain. Although the cut-off frequency of the optical system is 127 cpd, MTF values of higher frequencies than 60 cpd were annulled. This filter mimics limit of frequency imposed in the clinical devices due to the background noise in the acquired double-pass images[128]. Furthermore, the implemented low-pass filter focuses the analysis on the relevant spatial frequencies for the human vision. Numerical results are depicted in Figure 2-6.
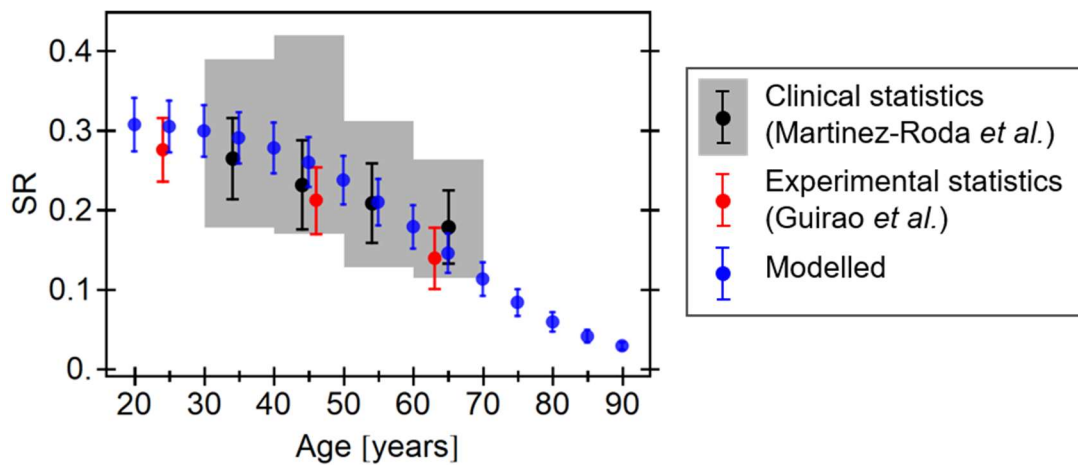
Figure 2-6. Aging effects on SR. Points and bars represent mean and standard deviation values, respectively. Moreover, gray region shows the maximum and minimum clinically founded SRs for each range of age.

Numerical mean SR values are generally within the standard deviation of both experimental and clinical data; however, they are slightly higher than both experimental and clinical mean values for ages less than 55 years. Surprisingly, these results are apparently contradictory respect to the previous HO RMS comparison (see Figure 2-5) where numerical mean values were higher than the clinical ones. A possible explanation to this 'contradiction' is given in the next paragraph.

The spatial resolution of the Hartmann-Shack sensor, used for the clinical HO RMS assessment, is mainly limited by the size of the lenses in the array. It filters the high-spatial frequency phase perturbations and underestimates the HO RMS. On the other hand, the double-pass PSF is affected by the phase perturbations of all spatial frequencies, producing SR values lower than the expected ones from the reported clinical HO RMS[131]. In conclusion, the proposed model generates representatives SR values of the human eye for different ages. Additionally, an analysis on the SR values allows understanding the differences between the modelled and clinical HO RMS.

2.2.3 Wavelength dependence of straylight

The wavelength dependence of the straylight have been measured in subjects with a variety of ocular pigmentations and ages using subjective[37] and objective[132] techniques. This dependence is originated from the intraocular scattering and the diffuse reflectance of the retinal layers[133]. However, according to the measurements of Ginis *et al.*[132], this dependence is mainly influenced by the scattering at large retinal angles (e.g., six degrees) in eyes with lighter pigmentation. Figure 2-7 shows those experimental measurements on four healthy eyes.

Alternatively, the chromatic response of the phase maps, generated by the proposed methodology, is evaluated by propagating the optical field with several wavelengths ranged from 450 to 650 nm. For a direct comparison with reported experimental results, the amount of straylight was set to 24 degree^{2}sr^{-1} for an illumination wavelength of 540 nm by manipulating the wavefront amplitude (using Equation 2-3). Light eyes condition was previously assumed by setting p=1 in Equation 1-2. Four wavefronts, simulating the same number of subjects, are produced by the replacement of four different random R matrices in the Equation 2-1. In this way, the straylight amount (at six degrees) is evaluated for those wavefronts illuminated with several wavelengths. The numerical results are shown in Figure 2-7.
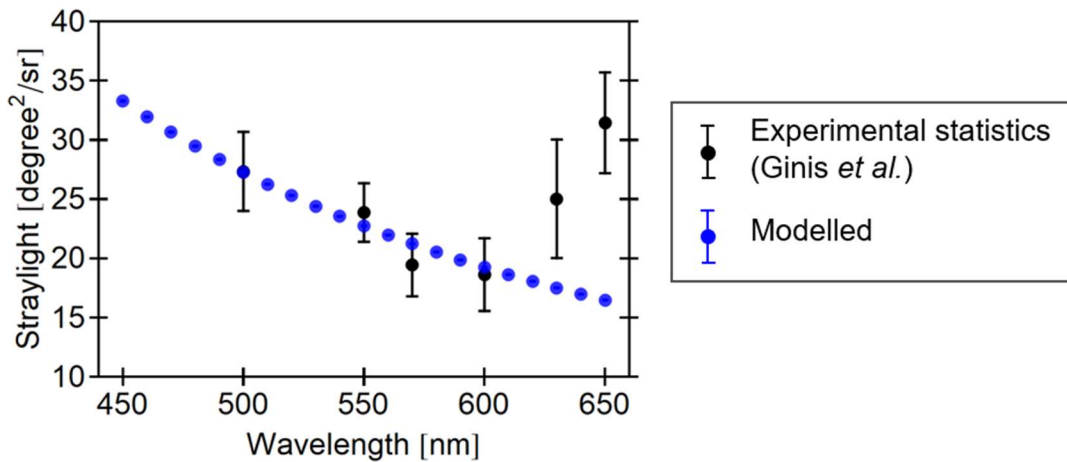
Figure 2-7. Wavelength dependence of straylight at six degrees. Points and bars represent mean and standard deviation values, respectively. The standard deviations of the numerical values are negligible.

The experimental and numerical mean values of straylight amounts are closer between 500 and 600 nm, demonstrating that developed model accurately reproduces the wavelength dependence of the intraocular scattering. Moreover, the comparison between experimental and clinical results also suggests that the origin of the wavelength dependence of the intraocular scattering (in light eyes) is the chromatic aberration of the diffraction through the scatterers, which were modelled as phase perturbations.

2.2.4 Ciliary corona

As previously shown, scattered light has different spatial distributions according to the wavelength. Generally, people can perceived this phenomena, known as ciliary corona, when glare sources are observed[134]. The appearance of the ciliary corona was numerically estimated by van den Bert *et al*.[135] (see Figure 2-8a) as the interference of the light propagate from multiple transparent scatterers. Although the parameters of the simulation were not realistic, such as the pupil size (0.2 mm) or the distribution of the particles, the study was supported in a survey on twenty subjects who approved the similarity between the simulated and the perceived phenomena. It allows to conclude that the ciliary corona is the result of the chromatic dispersion by diffraction.

The ciliary corona can also be replicated by the wavefronts generated with the proposed methodology. For its demonstration, a representative phase map for an 80 years old eye was calculated and illuminated using one hundred wavelengths ranged from 450 to 650 nm. A high number of considered wavelengths is required for increasing the reproduction fidelity. Each monochromatic PSF, an example is shown in Figure 2-8b, is spatially scaled by the ratio between design (540 nm) and illuminated wavelength[136]. The ciliary corona corresponds to the polychromatic PSF, calculated as the sum of all monochromatic PSFs. In this case, the same weight was given for all monochromatic PSFs mimicking a source with a flat-spectrum. Finally, the perception is simulated mapping the polychromatic PSF with a gamma function, according to the Steves law[137]. Figure 2-8c shows the resulting ciliary corona.

| van den Berg *et al.* | Monochromatic PSF | Polychromatic PSF |
| (a) | (b) | (c) |
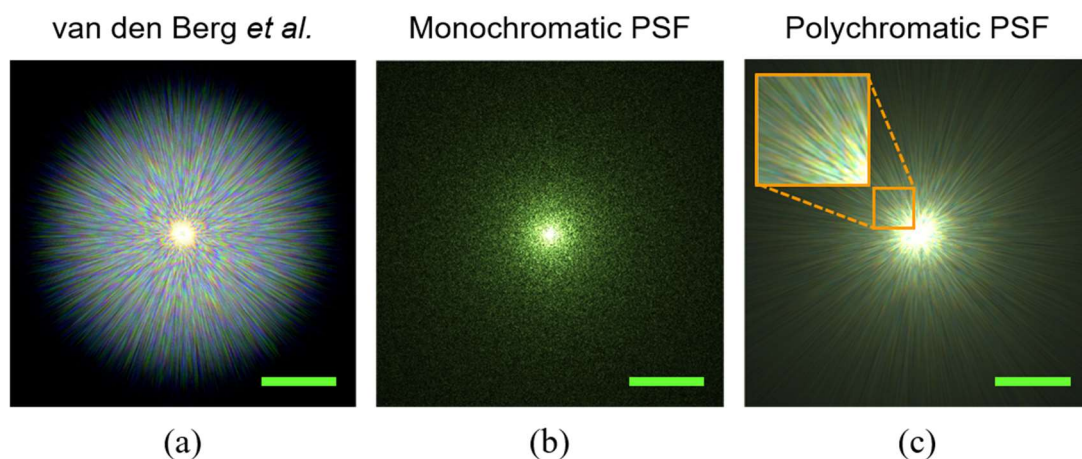
Figure 2-8. (a) Simulated ciliary corona by van den Bert *et al*[135]. Numerical calculated (b) monochromatic and (c) polychromatic PSFs using the proposed model. Length of green bar is one degree.

The chromatic aberration by diffraction is the common phenomena in both approaches: the interference of multiple individual scatterers by van den Berg *et al*. and the optical field propagation of the modelled ocular wavefronts (referring Figure 2-8a and c, respectively). Therefore, in both cases the corona is composed by fine needles colored

blue on the inside to red on the outside, as visually was evaluated by the observers[135]. In addition to the parameters of simulation, the differences between the appearance of the ciliary coronas could be originated in unlike settings of brightness, contrast, and others image features.

In summary, the discussed comparisons between the numerically reproduced ocular phenomena with the clinical and experimental data allows the validation of the proposed methodology to generate controllable amounts of intraocular straylight. This model will be used in further experiments to evaluate the visual impact of artificially induced straylight and to simulate the effect of cataract in an optical bench.

3. VISUAL EFFECTS OF ARTIFICALLY INDUCED INTRAOCULAR SCATTERING

In the first Section of this Chapter, the performance of the model is evaluated through the comparison between programmed and experimentally measured amounts of straylight. The optical integration method was implemented to estimate the generated amounts of straylight. In addition, the model can be used for a better understanding of the visual effects of intraocular scattering. Therefore, a visual simulator is developed by modifying the setup used for the estimation of the amounts of straylight. The visual effects are evaluated in terms of the visual acuity (VA) and the contrast sensitivity (CS). In Section 3.2, VA was evaluated for different amounts of straylight and retinal eccentricities. In the following Section, the glare sensitivity is tested at fovea by implementing a differential CS method following two aims: to understand the dependence of the CS with straylight and to subjectively assess the programmable amounts of straylight. Moreover, CS is evaluated for several amounts of straylight and retinal eccentricities. The results of both VA and CS in the eccentricities are discussed to explain the found benefits of the cataract surgery with preexisting age-related macular degeneration (AMD). In this pathology, the normal function of the photoreceptors in the fovea is lost, leading subjects to use the near peripheral retina that usually remains functional and whose performance is lower than the foveal one[138].

3.1 Experimental generation and evaluation of the straylight

The instrument to both generate and evaluate the intraocular straylight is depicted in Figure 3-1. The programmable generation of the straylight was mainly carried out by a LCoS device (PLUTO; Holoeye, Germany) as spatial phase modulator, where the previously designed phase maps were displayed. The LCoS device was calibrated by applying the procedure described in Appendix A.

The objects displayed on a LED monitor are imaged through the LCoS device by an artificial eye which is composed of a biconvex lens and 14-bits camera (Luca; Andor, Belfast, UK), acting as cornea and retina respectively. The pixel pitch of the LCoS (8 μm) limits the angular range of the PSF to 1.93 degrees, which is not enough for an appropriated representation of wide-angle intraocular scattering. Therefore, a telescope with an angular magnification of six was introduced in the setup. It simultaneously conjugates the SLM plane with the pupil of the artificial eye. The size (N) of the matrix displayed on the SLM is 1000 pixels and it produces a pupil size (ϕ) of 1.33 mm. In this way, phase perturbations with periods ranged from 2.67 to 1333.33 μm, which correspond to an angular domain of the PSF from 0.023 to 11.9 degrees (radius), were represented. The performance of the LCoS was improved by including a horizontal linear polarizer and a green filter ($\lambda \equiv 540 \pm 10$ nm) into the telescope.
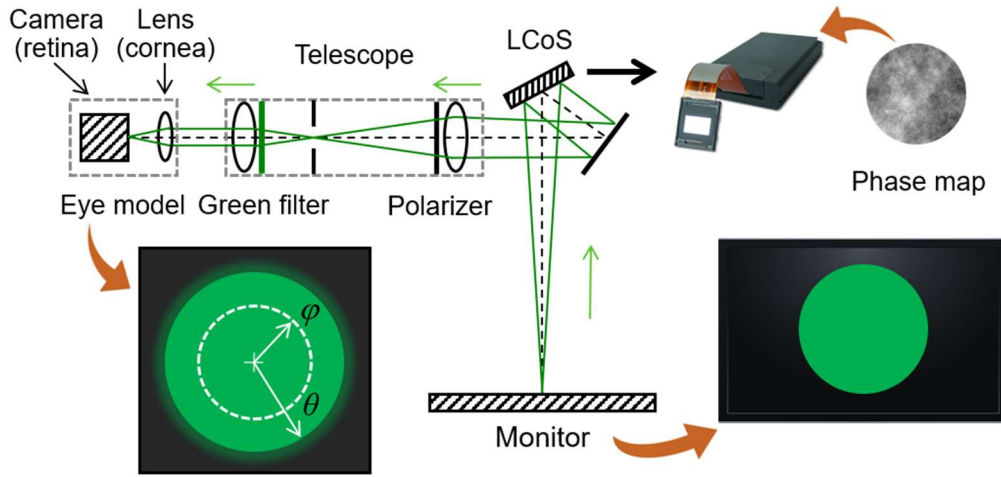
Figure 3-1. Experimental setup for the simultaneous generation and estimation of straylight.

3.1.1 *Implementation of the optical integration method*

The generated straylight was assessed using the optical integration method[68,117]. It allows to retrieve the angular averaged PSF with high dynamic range by recording projected disks of uniform irradiance and angular wide 2θ from the monitor. Thus, the incoherent PSF is calculated from the recorded disks using its relationship with their central intensities I_c (following the notation shown in Figure 3-1):

$$I_c(\theta) = \int_0^\theta 2\pi PSF(\varphi)d\varphi \quad (3\text{-}1)$$

It means that each point source localized on φ radius has an intensity contribution at the center of the disk that equals to $PSF(\varphi)$ and therefore the complete annular ring provides a total energy of $2\pi\varphi\,PSF(\varphi)$. The integration of φ values from 0 to θ predicts the effect of the complete disk. Thus, the PSF at θ angle is retrieved calculating the angular derivative of the Equation 3-1:

$$PSF(\theta) = \frac{1}{2\pi}\frac{dI_c(\theta)}{d\theta} \quad (3\text{-}2)$$

A simplified function is proposed by the approximated PSF estimation from the recorded central intensities[117]:

$$PSF(\theta) = C\,PSF_{dl} + D\left[\frac{1}{(\theta+0.001)^E}\right] \quad (3\text{-}3)$$

where PSF_{dl} is the diffraction-limited PSF radially normalized to 1. The C, D and E parameters are optimized to minimize the mean squared error between the experimental and numerical central intensities data. Numerical values are calculated replacing Equation 3-3 in 3-1. Moreover, the parameters are adjusted to comply with the normalization condition of the encircled energy by the calculated PSF on the considered τ angular range, i.e., $\int_0^\tau 2\pi PSF(\theta)d\theta = 1$. As explained above, due to the SLM features and the telescope

magnification, τ is equivalent to 11.9 degrees. The straylight is calculated as the multiplication between PSF and θ^2 (θ in degrees).

The performance of the phase maps calculated by the developed model (Section 2.1) is experimentally evaluated. The phase maps, calculated for the addition of six straylight amounts (s_{add}) at six degrees ranging from 10 to 60 deg^{2}sr^{-1}, were displayed in the LCoS. The central intensity for each projected disk is the temporal average of five measured values. Figure 3-2 shows the normalized central intensities and their fits from Equation 3-2. High correlation coefficients ($r^2 > 0.990$) between experimental and numerical data allow to continue with the estimation of straylight amounts.
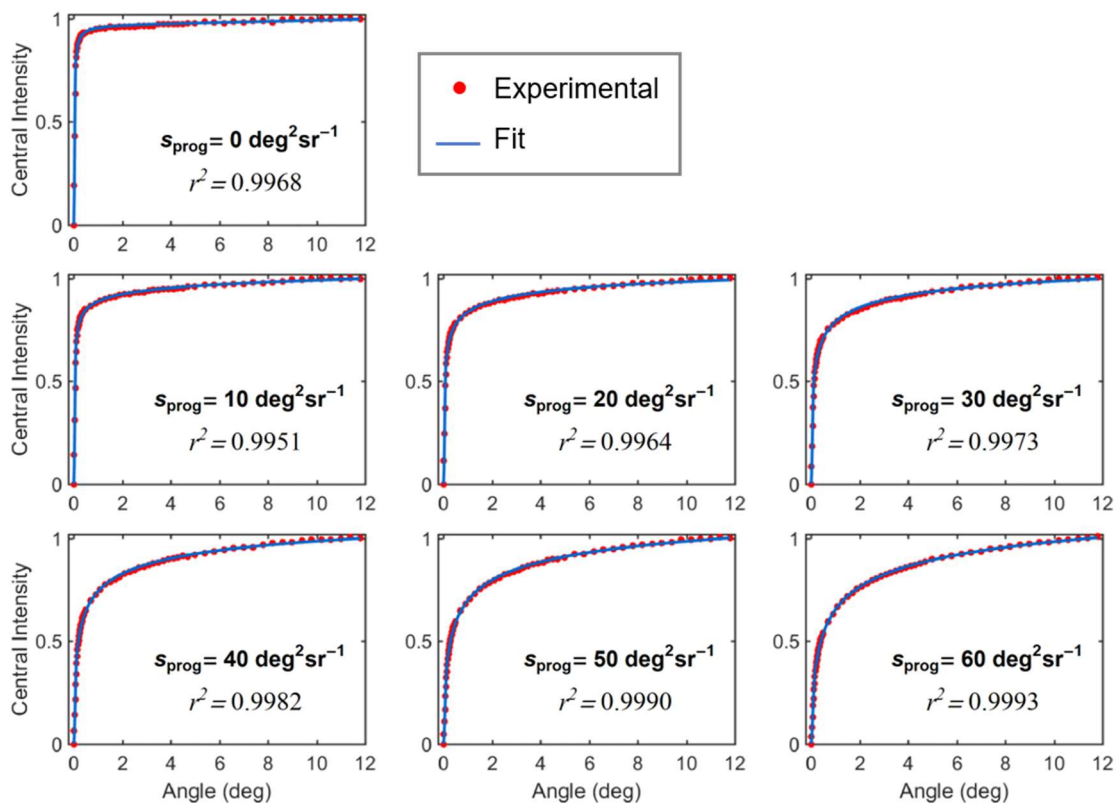
Figure 3-2. Recorded and fitted central intensities as function of the θ angle subtended by the projected disks on the monitor.

The retrieved PSFs are shown in Figure 3-3a. Moreover, they are compared with the CIE PSF for a 70 years-old eye. Figure 3-3b depicts the programmed and measured additions of straylight at six degrees, pointing out the measured amount straylight when no-additional scattering is induced in the setup (i.e., a flat wavefront is displayed on the LCoS device). This offset of 9.12 deg^{2}sr^{-1}, equivalent to straylight amount expected for a 50 years-old eye (according to Equation 1-2), is originated by the diffusion properties of the nematic liquid crystal that composes the LCoS device[139], scattered light in others optical components and parasitic light reflections.
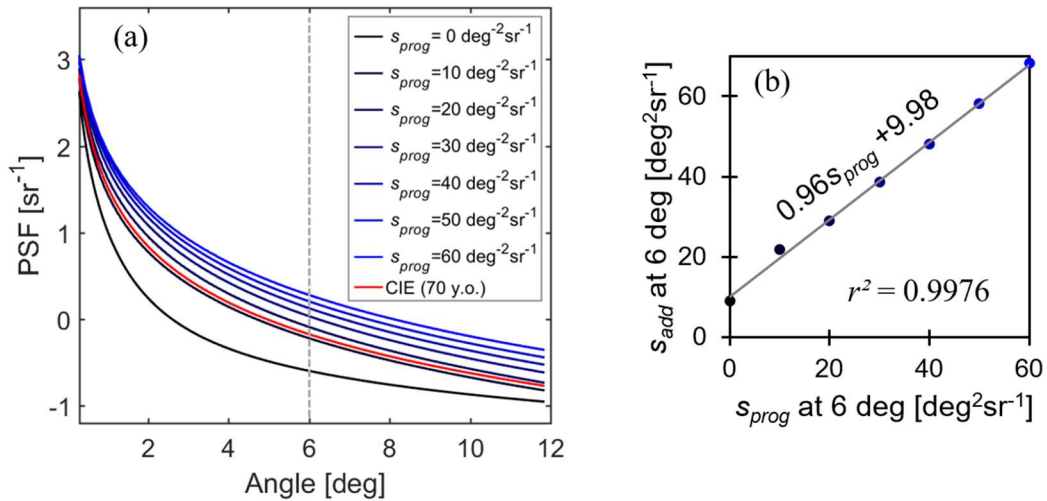
Figure 3-3. (a) PSFs retrieved from the fitted central intensities shown in Figure 3-2. (b) Relationship between the (s_{prog}) programmed and (s_{add}) experimentally assessed amount of straylight at six degrees.

Similarity between experimental and CIE PSF profiles demonstrates the capacity of the developed model to generate the effect of the intraocular straylight. In addition, the slope of the linear relationship, which is approximately one, between programmed and measured additions of straylight shows the accuracy control of the amount of scattered light through the amplitude of the phase maps, as it was explained in Section 2.1.

3.2 Straylight effects on visual acuity

VA was measured in the fovea and two retinal eccentricities to better characterize the impact of induced scatter on central and near peripheral vision. When both pathologies (AMD and cataracts) are simultaneously developing, previous studies suggest[140–143] that the improvement of the visual acuity after the cataract surgery is limited by the stage of the retinal pathology.

For the VA assessment, the instrument of Figure 3-1 was adapted to be used as a visual simulator by incorporating realistic effects of straylight (see Figure 3-4). High contrast white-on-black 'E' optotypes were displayed on the monitor in front of the LCoS device. The stimulus has a luminance of 0.3 cd/m^2 and was seen through the LCoS device by the dominant eye of each subject. The subject was asked about five random orientations of each optotype size. To evaluate the VA, the stimulus size was gradually reduced until the subject fails in three or more trials of orientation choice. Then, the angular resolution was calculated as one fifth of the last angular size for which the subject got right more than two trials. Finally, VA was reported in LogMAR units as the logarithm of the angular resolution in minutes of arc (arcmin). In addition, for the VA evaluation at several eccentricities, a LED was placed in front of the monitor acting as fixation point.
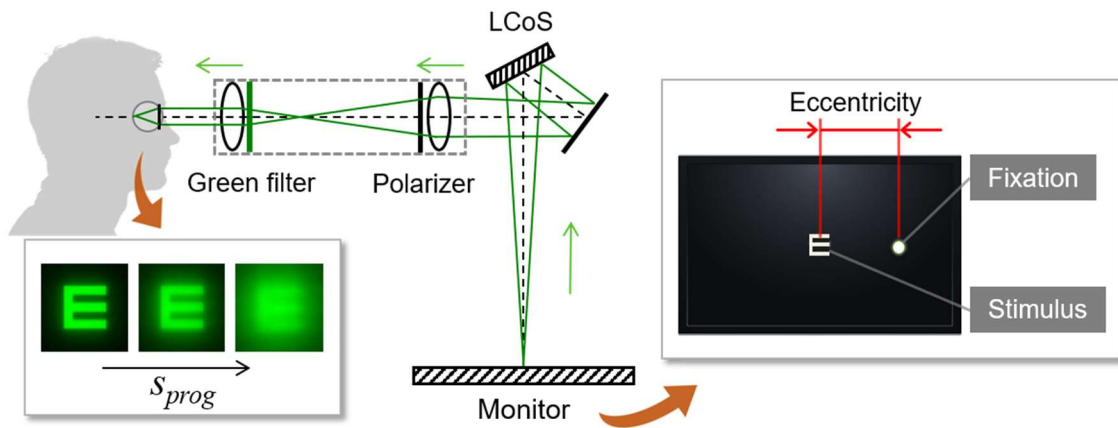
Figure 3-4. Visual simulator to assess the straylight effects on the VA at foveal and the near retinal periphery.

Ten subjects aged 30±4 years old, without any known ocular pathologies, participated as volunteers in this study. Although the small artificial pupil mitigates the effects of their natural aberrations, the best focus correction was achieved displaying spherical wavefronts on the LCoS device.

In the case of the foveal VA assessment, six programmed amounts of straylight were added to the intraocular straylight of each eye. On the other hand, VA was measured at 5 and 10 degrees in the nasal visual field with two additions to the intraocular straylight. In both cases, the maximum induced straylight amount was 82.4 deg^2sr^{-1} that corresponds to a nuclear cataract graded between 2 and 3 in the LCOSIII system[70]. Figure 3-5 shows the dependence of the averaged VA with straylight and eccentricity.
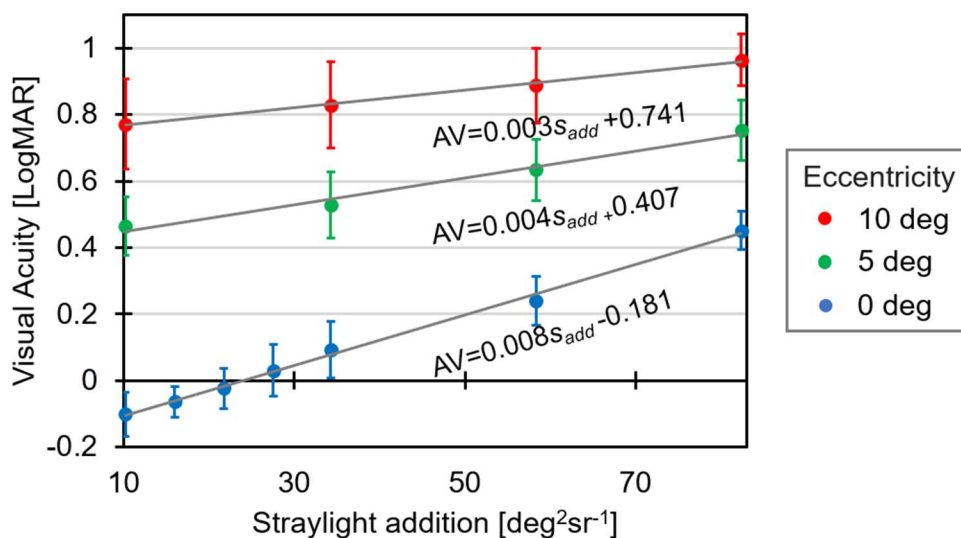
Figure 3-5. Averaged visual acuity as function of the added straylight and the eccentricities. Error bars are standard deviations.

According to the results, there is a linear increase of the LogMAR VA when the amounts of induced scattering were increased at both fovea and periphery. The increase

of the amount of intraocular straylight involves the increment of the root means squared of the induced aberrations, as explained in Section 2.1, with the subsequent increase of the LogMAR VA values[17,144]. Additionally, the slopes of the linear regressions in Figure 3-5 allow to conclude that the impact of straylight on VA reduces when eccentricity increases. This may explain the modest improvements often documented after cataract surgery in patients with AMD[140].

3.3 Straylight effects on contrast sensitivity

Generally, CS can provide more information about the cataract development than VA[59]. It becomes more dependent to the amount of straylight if glare sources are present which is known as glare sensitivity[54]. The differential CS test, based on sequential measurement of the CS for different glare situations, have been proposed to quantify the intraocular straylight[63,65,145]. The differential CS test was performed to subjectively verify the additions of the straylight amounts. Then, the CS was assessed as function of the artificially induced straylight at the fovea and two eccentricities. This experiment allows to understand the impact of the cataract surgery on patients with a retinal comorbidity on CS, which hasn't been documented as the VA.

Figure 3-6 shows the modified instrument to assess the CS. The stimuli were Gaussian-windowed sinusoidal gratings of 3 cycles/degree over 2 degrees on retina with a mean luminance of 0.3 cd/m^2. This frequency was selected because CS at low spatial frequency are most informative in clinical studies of cataracts[146]. The task for each subject was the recognition of the orientation (left for 45° or right for 315°) of the stimuli with different contrast, appearing for 0.3 seconds in the monitor followed by an acoustic signal. A QUEST[147,148] algorithm selected the stimulus contrast for each trial based on the previous answers to estimates the contrast threshold quickly. Each session of CS assessment consisted of 50 recognition tasks.
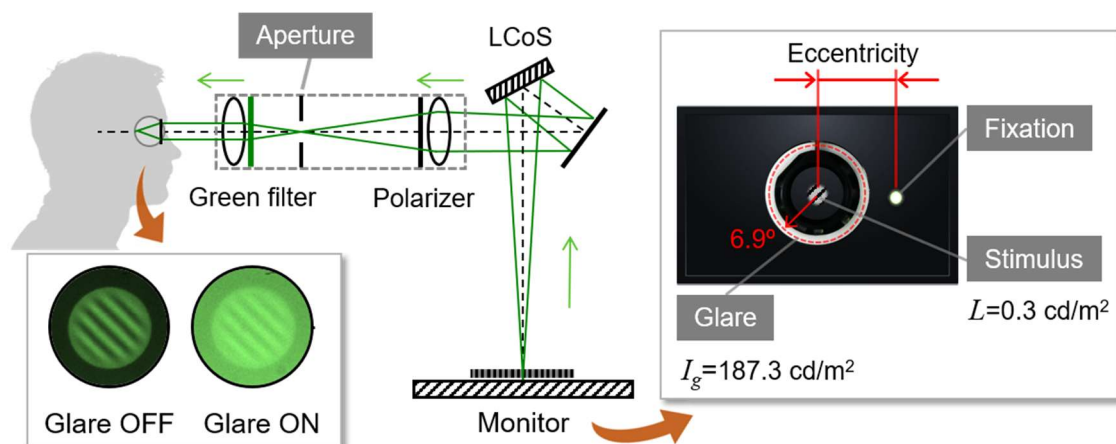
Figure 3-6. Visual simulator for two purposes: i. the subjective evaluation of the generated straylight by the differential (glare switched on and off) CS test; and ii. the assessment of the straylight effects on the CS at foveal and the near retinal periphery.

For the differential CS test, a ring lamp was placed in front of the monitor as glare source, composed by 36 white LEDs covered by a diffuser. However, the projection of the glare on the retina was blocked by a circular aperture at the image plane because the aim was to evaluate the changes in the stimulus contrast due to the straylight induced by the LCoS device. For the assessment of CS at several eccentricities, a low-luminance LED was placed in front the monitor to guide the gaze, and the glare source was removed.

3.3.1   Contrast sensitivity with glare sources

Sequential measurements of CS in three subjects (aged 30±1 years old) were performed with and without glare to subjectively evaluate the additions of the straylight amounts. Six programmed straylight amounts were induced. Each subject underwent four measurement sessions, two without and two with the glare annulus illuminated, for each straylight addition. The procedure was applied for four gradual straylight additions up to 39.1 $deg^2 sr^{-1}$.

Figure 3-7 shows the logarithmic values of CS for each subject, with (CS_{on}) and without (CS_{off}) glare, as function of the artificially induced straylight amounts. The impact of straylight on CS is higher when glare source is present. Linear regressions were applied with correlations coefficients higher than 0.9654.
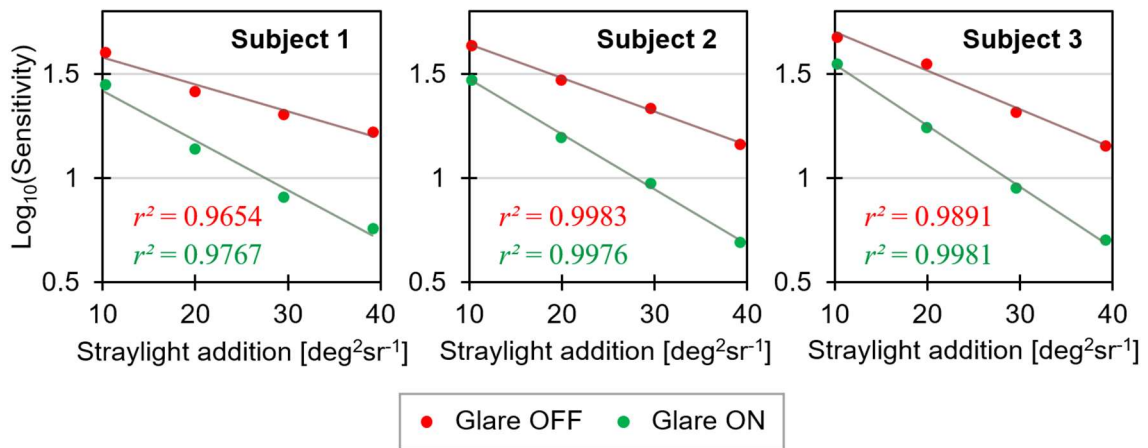
Figure 3-7. Logarithm of the CS as function of the added straylight for each subject and the two glare conditions.

The additions of straylight (*s*) measured with the optical integration method can be verified using the CS measurements by applying the Paulson-Sjöstrand formalism[64]. It is valid if there is not visual adaptation to straylight effects and the pupil size does not change during the measurements, which is fulfilled because the stimulus presentation time was short, and the glare source was not directly projected to retina. Thus, the ratio between sensitivities for each glare condition (CS_{on} and CS_{off}) is written in terms of the luminance parameters:

$$\frac{CS_{on}}{CS_{off}} = \frac{L}{L+I_g} \quad (3\text{-}4)$$

were L is the mean luminance of the sinusoidal stimulus and I_g is the veiling luminance that covers the stimulus area from the scattered light from glare source.

Moreover, I_g luminance can be quantified assuming the glare lamp as an annulus with uniform intensity I_G:

$$I_g = I_G \int_{\alpha_{min}}^{\alpha_{max}} 2\pi\alpha PSF(\alpha)d\alpha \qquad (3\text{-}5)$$

where α is the visual angle, α_{max} (6.8 degrees) and α_{min} (7.0 degrees) are the equivalent maximum and minimum angular radius respectively and PSF corresponds to the mimicked ocular response (see some examples at Figure 3-3a).

As a further simplification, the PSFs is approximated to the Stiles-Holladay equation[28] ($PSF = s\alpha^{-2}$, α in degrees). Thus, the veiling luminance becomes directly proportional to the induced straylight when the integral of Equation 3-5 is developed:

$$I_g = 2\pi I_G s Ln\left[\frac{\alpha_{max}}{\alpha_{min}}\right] \quad (3\text{-}6)$$

Thus, replacing Equation 3-6 in 3-4, the induced straylight is retrieved using the psychophysical and technical parameters:

$$s = \frac{1}{2\pi}\frac{L}{I_G}\left(Ln\left[\frac{\alpha_{max}}{\alpha_{min}}\right]\right)^{-1}\left(\frac{CS_{off}}{CS_{on}} - 1\right) (3\text{-}7)$$

Finally, Figure 3-8 shows the comparison between the induced straylight amounts measured with optical integration method and calculated applying the Equation 3-7 to the experimental CS_{off} and CS_{off} values. Their agreement is supported by the r^2 correlation coefficient. These results ratify the accuracy of the CS measurements for several straylight additions and their glare sensitivity as depicted in Figure 3-7.
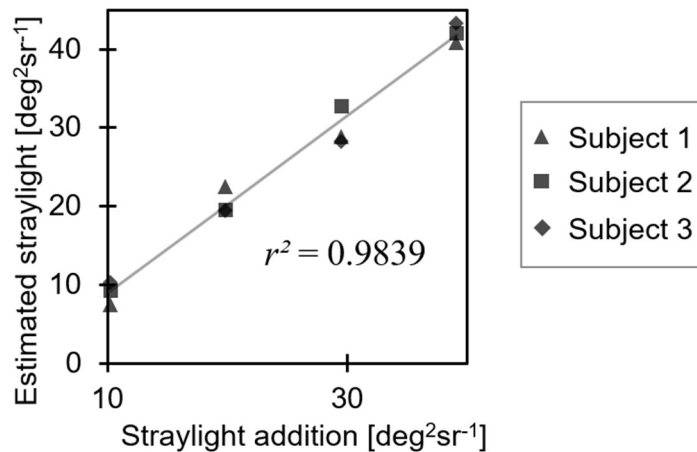
Figure 3-8. Relationship between the added straylight (s_{add}) and the subjectively estimated straylight through the differential CS test. Linear regression equation is $1.14s_{add}$-2.38.

3.3.2 Impact in the near retinal periphery

The effects of straylight and eccentricity on CS were measured in five volunteers aged 34 ± 12 years old, without any known ocular pathologies. CS was estimated at the fovea and two eccentricities in the nasal visual field (5 and 10 degrees). Moreover, for each eccentricity, three straylight amount were added up to 58.3 deg^2sr^{-1} without the presence of a glare source.
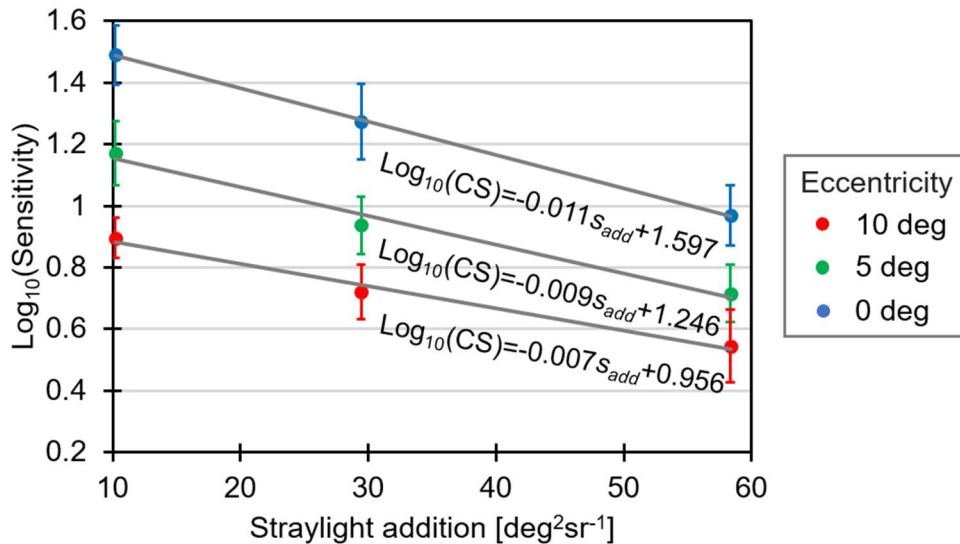
Figure 3-9. Averaged logarithm of the contrast sensitivity as function of the added straylight and the eccentricities. Error bars are standard deviations.

Figure 3-9 shows the dependence of the averaged CS with straylight and eccentricity. Linear regressions are supported in the previous analysis where more straylight additions were used (see Figure 3-7). CS is more sensitivity to the straylight addition that VA. For instance, the foveal CS decreases in 0.52 log units due to straylight induction of 50 deg^2sr^{-1} while the absolute difference between CS assessed at fovea and 5 degrees of eccentricity is 0.32 log units with the minimum straylight addition. In the case of VA, the increment in LogMAR units due to the addition of 50 deg^2sr^{-1} is only 63 % from the difference between the AV assessed at fovea and 5 degrees of eccentricity (see Figure 3-5) with the minimum straylight addition. Moreover, the impact of the additions of straylight on the CS values decreases when eccentricity increases. The measured CS values without induced scattering across the eccentricities differs to the previously reported values[149,150] mainly due to the differences in the stimuli's luminance and the size of the artificial pupil.

The results from both AV and CS tests validate the previously introduced model of the phase perturbations for the adjustable addition of intraocular scattering. Thus, this model will be implemented in further experiments to generate the realistic effect of cataracts.

4. WAVEFRONT SHAPING TO SEE THROUGH SCATTERING MEDIA

In this thesis, the wavefront shaping (WS) technique is proposed to extend the applicability of the AO systems in cataractous eyes. In Section 4.1, an instrument is presented using a liquid crystal spatial light modulator for both the generation of straylight and the implementation of the WS technique. In Section 4.2, the performance of the instrument is examined through the improvement of both PSF and images affected by diffusers and astigmatism.

4.1 Experimental implementation of the WS technique

Figure 4-1 shows the experimental setup for the simultaneous reproduction and compensation of intraocular straylight effects using the WS technique. The generation, testing and compensation of intraocular scattering are carried out by a single LCoS device (PLUTO; Holoeye, Germany) as a SLM. The LCoS's area was divided in two halves, conjugated by a telescope with unitary magnification (composed of a single lens and two mirrors). The cataractous phase maps are displayed in the first half and the testing phases (or the correcting phase maps) are displayed in the second one. The LCoS is illuminated by an expanded and collimated green laser beam with horizontal polarization. The Fraunhofer pattern of the exit pupil, after the second pass, is formed by a lens on an EMCCD camera (Luca; Andor, Belfast, UK).

Both halves of the LCoS were digitally aligned with a simple procedure. A random binary phase map, with a depth of modulation of π radians, is displayed on each LCoS's half. The phase map was rotated 180 degrees in the second half to compensate the inversion introduced by the conjugation. The coincidence between the pupils is evaluated trough the Strehl ratio of the PSF acquired by the camera. Thus, after a scan of relative pupil positions, they will be aligned when the maximum Strehl ratio is achieved, due to the flattening of the total wavefront. This procedure was repeated before each experiment.

The stepwise sequential algorithm[95] was adopted for the WS implementation because of its simplicity. According to this algorithm, the testing phase map is divided in regular segments where the phase of each segment is gradually changed between 0 to 2π radians, selecting the phase value (φ) that maximizes the intensity at the target (see Section 1.4.2). The target corresponded to the speckle grain with the highest energy, where generally the ballistic photons are reaching the camera. In principle, the LCoS has a large dynamical range for the phase modulation (up to 255 levels), however, the length of time for the compensation routine becomes impractical when large phase steps are considered. Here, the phase of each segment was changed in twelve phase steps while the intensity of a selected grain of speckle (i.e., the target) is recorded. Figure 4-2 shows two examples of those signals with high and low signal-to-noise ratio (SNR). The signals were fitted to a

cosine function for the accurately φ estimation, avoiding the noise introduced by the camera. Moreover, the φ value is approximated to sixteen values between 0 to 2π radians. The theoretical diffraction efficiency of this phase discretization for the correcting phase is 98.7%.
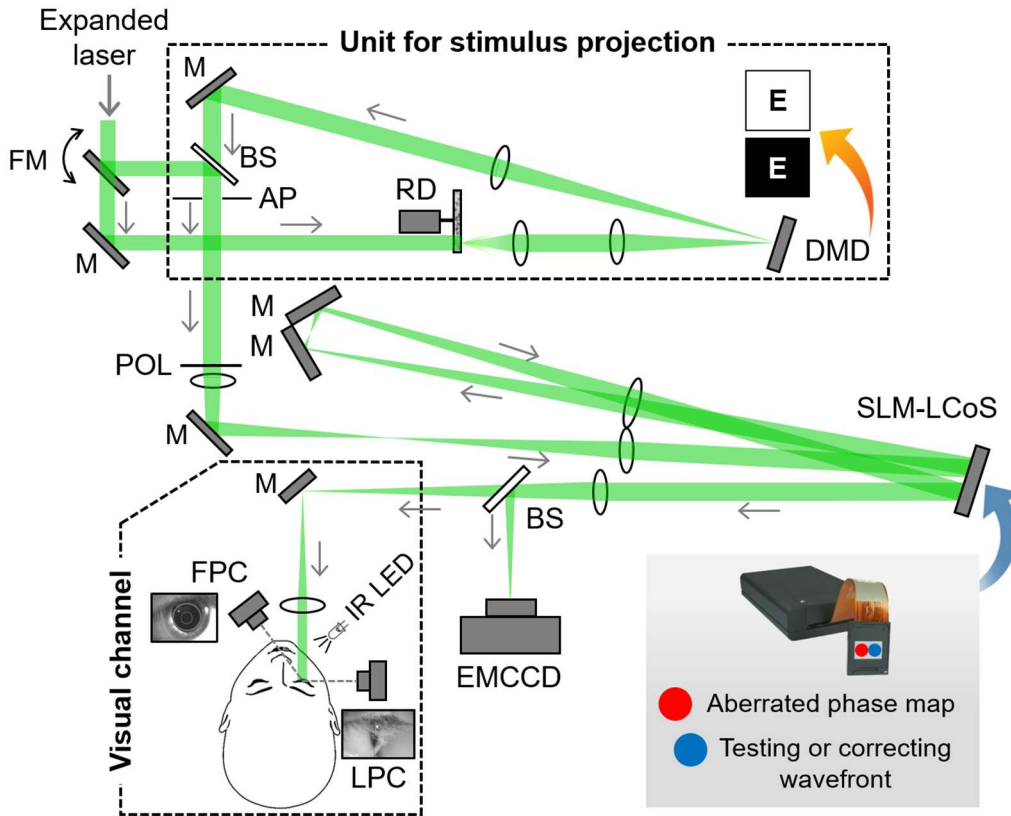
Figure 4-1. Experimental setup for the simultaneous generation, testing and compensation of the intraocular scattering using the WS technique. Labels description: FM, flip mirror; M, mirror; RD, rotating diffuser; BS, beam splitter; AP, aperture; POL, lineal polarizer; IR LED, infrared light-emitting diode; FPC and LPC, frontal and lateral pupil cameras, respectively.
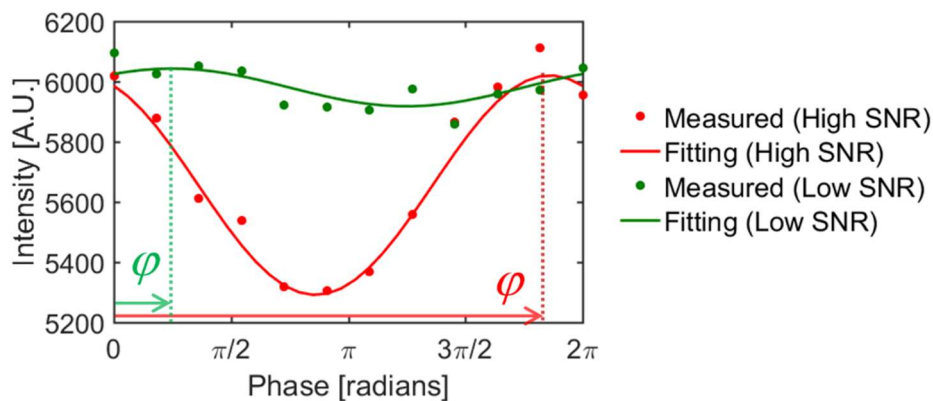
Figure 4-2. Examples of the intensity signal across the phase changes for a segment of the SLM. Signals were fitted for the accurately estimation of the φ phase that maximizes the intensity.

Once the PSF was optimized, its effects on the extended and incoherent images were evaluated. For this purpose, a stimulus projection unit was included in the setup, which is illuminated by the same laser beam used in the correction stage. High-contrast objects were displayed using a Digital Micromirror Device (DMD, ViALUX 1100; Texas Instruments Inc., USA) which is conjugated to a rotating diffuser that breaks the spatial coherence of the beam. A set of lenses translate the object to the image plane at the camera following the double-pass through the LCoS.

Furthermore, a visual channel was attached to the detection stage of the setup for the subjective evaluation of WS performance. The entrance pupil of the eye is conjugated with the LCoS by a telescope with a magnification of 0.43. Two complementary metal-oxide semiconductor cameras (CMOS; FPC and LPC in Figure 4-1) together with an infrared LED are used to monitor the transversal and axial position of the eye's pupil while the subject's head is supported by a chin and forehead rest. The methodology for the visual assessment under the simulated scattered and corrected conditions will be described in Section 5.1.3.

Three additional actions are required to complete the WS implementation. First, the temporal performance of the phase modulation by the LCoS was evaluated for several driver's setups to select the most appropriate for this application. Next, the influence of the zero-diffraction order must be suppressed for an accurate estimation of the correcting wavefront and the acquisition of the improved image. In addition, the inherent aberrations of the system were compensated to aim the WS correction at phase perturbations programmed using the LCoS or externally added. Finally, the experimental system was tested for the image retrieval through physical diffusers and aberrations displayed on the LCoS itself.

4.1.1 Evaluation of the temporal performance of the LCoS device

The speed of the WS technique is mainly limited by the temporal response of the LCoS device, which depends on the dynamical properties of the birefringence in the liquid crystal molecules and the voltage addressing sequence applied to each pixel. Previous studies[151,152] evaluated the polarimetric effects of the voltages sequences on the same LCoS model (PLUTO; Holoeye). The impact of three sequences ('0_6', '5_6' and '18_6') on the temporal performance of the phase modulation was also evaluated[153]. To reduce the length of time in the compensation task, the temporal performance of phase modulation was evaluated in the used LCoS device for the same three voltage sequences. In addition, for each sequence, the phase was calibrated following the procedure explained in the Section 3.1.1. Results of phase calibration are shown in Figure 4-3.

Figure 4-4 shows the setup and procedure for the temporal analysis of the phase modulation. A photodiode (PDA36A; Thorlabs Inc., Germany) is placed at the Fraunhofer diffraction plane to record the central intensity when flat wavefronts are displayed in each half of the LCoS. The photodiode is behind of a pinhole with a diameter

of 100 μm for the spatial filtering of the focal point and its signal was digitalized by an acquisition card (DAC, USB6210; National Instruments, USA) with a frame rate of 250 kHz. At time *t*=0s, a vertical binary grating with a period of four pixels is displayed on the second half of the LCoS. The re-distribution of energy in the diffraction orders produces a decrement in the photodiode signal.
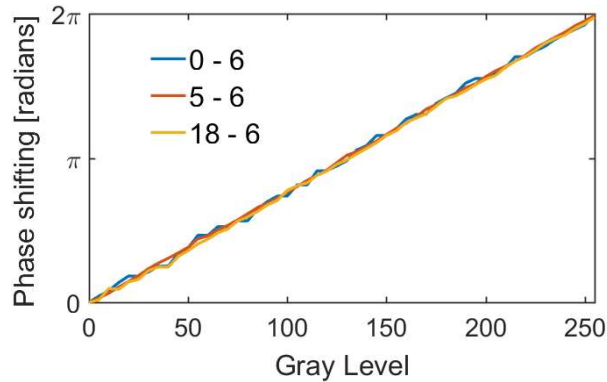
Figure 4-3. Phase shifting as function of the gray levels for several voltage addressing sequences programmed on the driver of the LCoS.
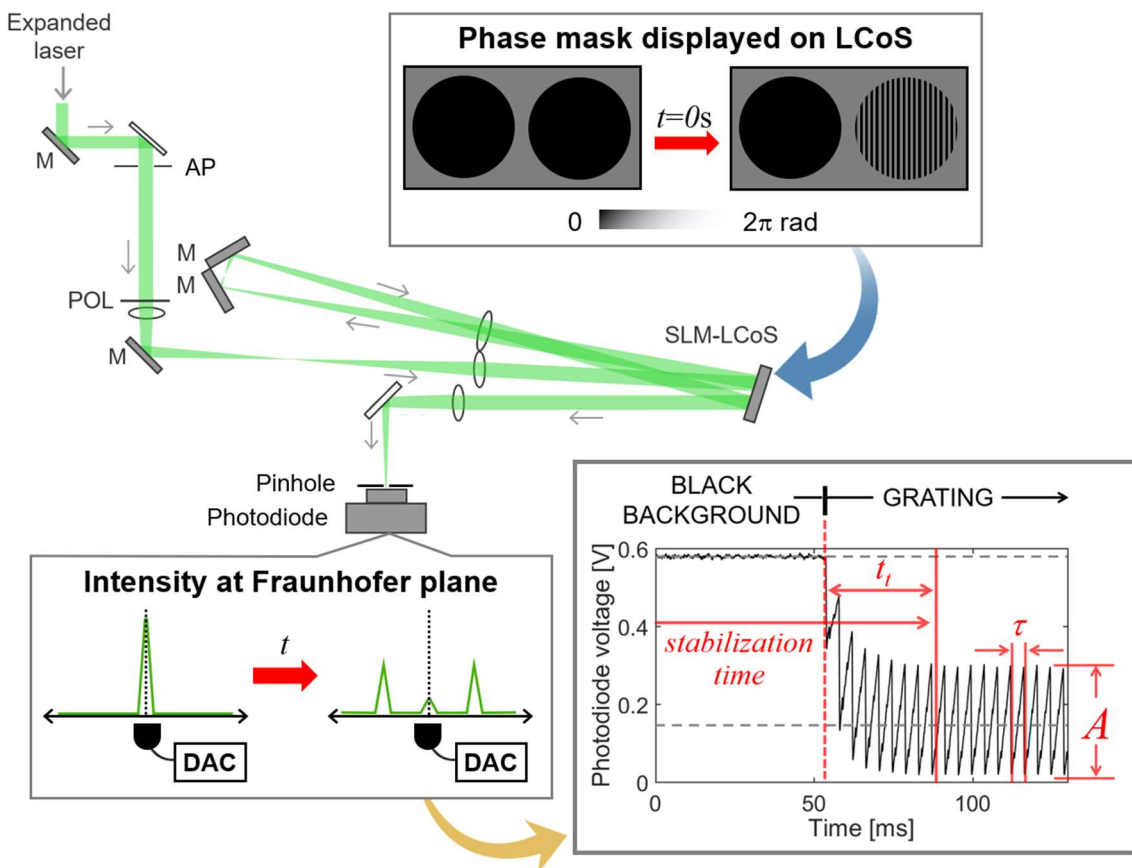
Figure 4-4. Temporal analysis of the LCoS's phase response by the parametrization of the intensity signal at the zero-diffraction order of a grating displayed on the second half of the LCoS.

The photodiode signal was parametrized in terms of: the transition time (t_t), associated to the LCoS's hardware and dynamical properties of the liquid crystal molecules; the *stabilization time*, is the sum of t_t and the required execution time of the Matlab routine that brings the information to the LCoS; and the amplitude (A) and the period (τ) of the wobbling, which is produced by the oscillations of the liquid crystal molecules induced by the digital driving[154,155]. These parameters are depicted in Figure 4-4 (inset).

Results of the parametrization (except A), for the three voltage sequences, are listed in the Table 4-1. The wobbling amplitude depends on the depth of the displayed grating as shown in Figure 4-5. These measurements are in agreement with the conclusions of previous studies[153,156].

Table 4-1. Parameters of the temporal response of the LCoS.

	Voltage addressing sequence		
	0_6	5_6	18_6
Maximum *stabilization time* (ms)	25 ± 7	29 ± 8	29 ± 7
Transition time t_t (ms)	16 ± 7	18 ± 9	14 ± 7
Period τ (ms)	2.3 ± 0.1	4.2 ± 0.1	16.6 ± 0.4
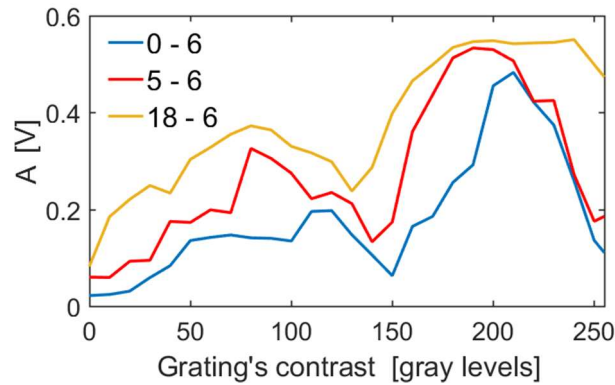
Figure 4-5. The wobbling amplitude and its dependence with the contrast of the gratings displayed on the LCoS.

In conclusion, the configuration '0_6' provides the highest temporal performance among the evaluated voltage addressing sequences. It reduces the wobbling and the stabilization time of the intensity signal when the phase maps are refreshing in the LCoS. However, the effective frame rate is 40 Hz instead of the nominal 60 Hz, according to the manufacturer. Therefore, this sequence will be used in the following experiments.

4.1.2 Suppression of the zero-diffraction order

The zero-diffraction order, understood as the undiffracted light after the pass by the LoCS, is mainly originated by the reflection in the cover glass of this device and the dead space between its pixels[157]. The overlapping of the zero-order diffraction with the low-intensity scattered light patterns has two effects: the performance reduction of the WS technique and the alteration in the evaluation of the uncorrected and corrected scattering effects on

imaging. Therefore, binary phase gratings were added to phase maps displayed on the LCoS, filtering the light propagated in the first order. The depth of modulation and period of both gratings were π radians and two pixels, respectively. Figure 4-6 shows the implementation of this methodology for each pass through the LCoS. In the first pass, a vertical grating is added to the cataractous phase maps. In the second pass, a horizontal grating is added to avoid the influence of others diffraction orders from the first pass, and in this case, a couple of mirrors re-direct the beam to the detection stage. The power of filtered light after the second pass is 16% of incoming light to the LCoS because of the diffraction efficiency of the binary phase gratings. Although the diffraction efficiency of blazed grating is almost 100%, binary gratings were chosen to minimize the impact on the angular range of the PSF.

This methodology is also useful for the representation of complex pupils in each half of the LCoS, which is particularly convenient to simulate the asymmetric double-pass through the ocular media in further experiments.
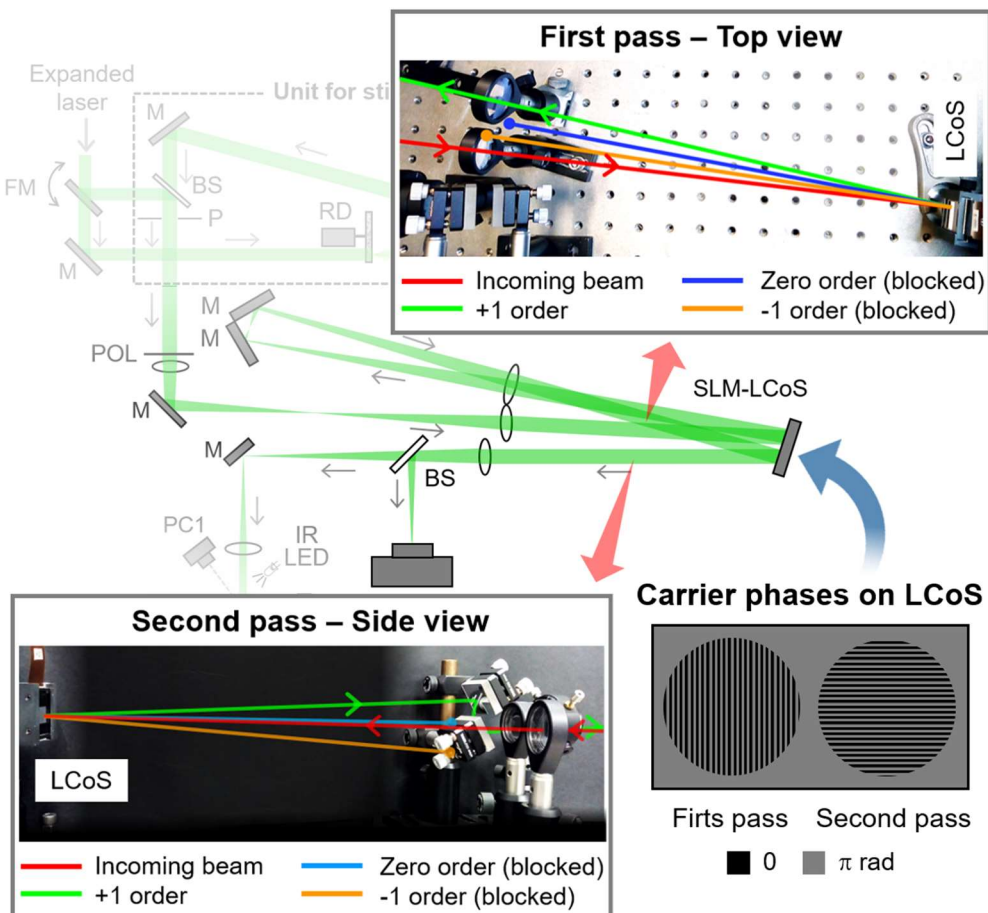
Figure 4-6. Experimental strategy to suppress the zero-diffraction order after each pass through the LCoS by adding carrier gratings. The mirrors to deflect the +1 diffraction order in the second pass are not shown in the sketch of the setup.

4.1.3 Compensation of the system's aberrations

The assembled optical system has inherent aberrations whose main source is the LCoS. The aberrations of this device, characterized by astigmatism, are originated from the technical limitations to polish the silica plate that supports the cells of liquid crystal[158]. Other sources of aberrations are oblique incidence of the beam on the LCoS and decentered illumination in the lens that conjugates both halves of the modulator.

The benefit after the pre-compensation of those aberrations is that the performance's analysis of the WS technique will be only aimed at the aberrations programmed in the LCoS or externally induced. Therefore, the pre-existing aberrations in the system were corrected applying an iterative procedure to increase the Strehl ratio. The compensating phase map was the summation of Zernike polynomials from 2nd to 5th order[15]. To estimate their coefficients, the PSF is recorded by the camera for several values of each coefficient, selecting and holding the value that maximizes the peak of the PSF (i.e., the Strehl ratio). The results of the compensating procedure, applied over a pupil with a diameter of 800 pixels, are shown in the Figure 4-7. At the end of the process, the Strehl ratio is enhanced 2.8-fold.
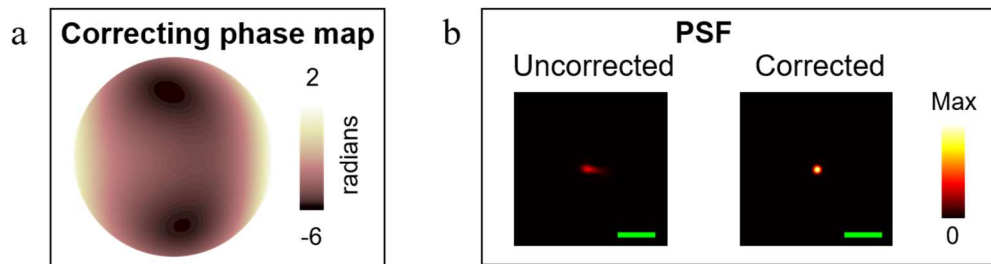
Figure 4-7. Compensation of the inherent aberrations of the system using the LCoS.

4.2 Evaluation of the WS performance

The performance of the developed instrument was evaluated by means of two experiments where the effects of the scattering and aberrations were separately corrected. Two physical diffusers were used to reproduce turbulence and turbidity conditions in the first experiment. In the second experiment, a cylinder phase map with two amplitudes were displayed on the first half of the SLM to be corrected by the second half. These experiments allow to test the ability of the WS technique to improve the quality of image under high-amplitude aberrations or high-scattering samples.

4.2.1 Seeing through physical diffusers

A demonstration of the WS performance was developed to retrieve the incoherent imaging through two physical holographic diffusers, following the experiment of Katz *et al.*[97]. The diffusers (Luminit, USA) provide gaussian light distributions with full widths at half maximum (FWHM) of 0.5 and 10 degrees. They allow to reproduce the effects of turbulence (FWHM≡0.5 degrees) and turbidity (FWHM≡10 degrees), as shown in Figure 4-8. While the diffuser with low FHWM only induced aberrations that blurs the image,

the diffuser with high FWHM strongly scattered the light with an approximated amount of straylight $Log_{10}[s] \equiv 2.4$ at 3.5 degrees.
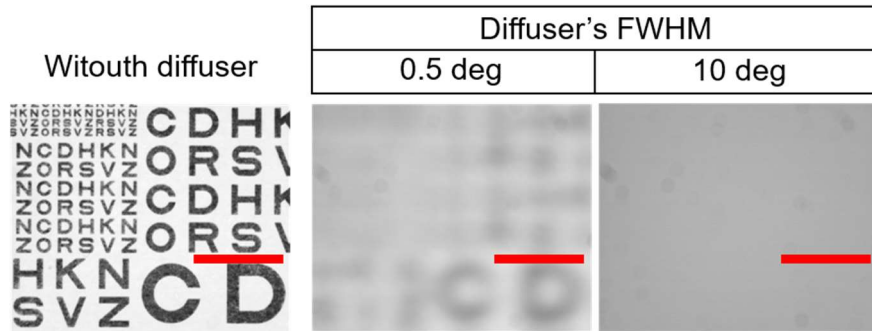
Figure 4-8. Optotypes with different angular size seen through the diffusers. Length of red bar is five degrees.
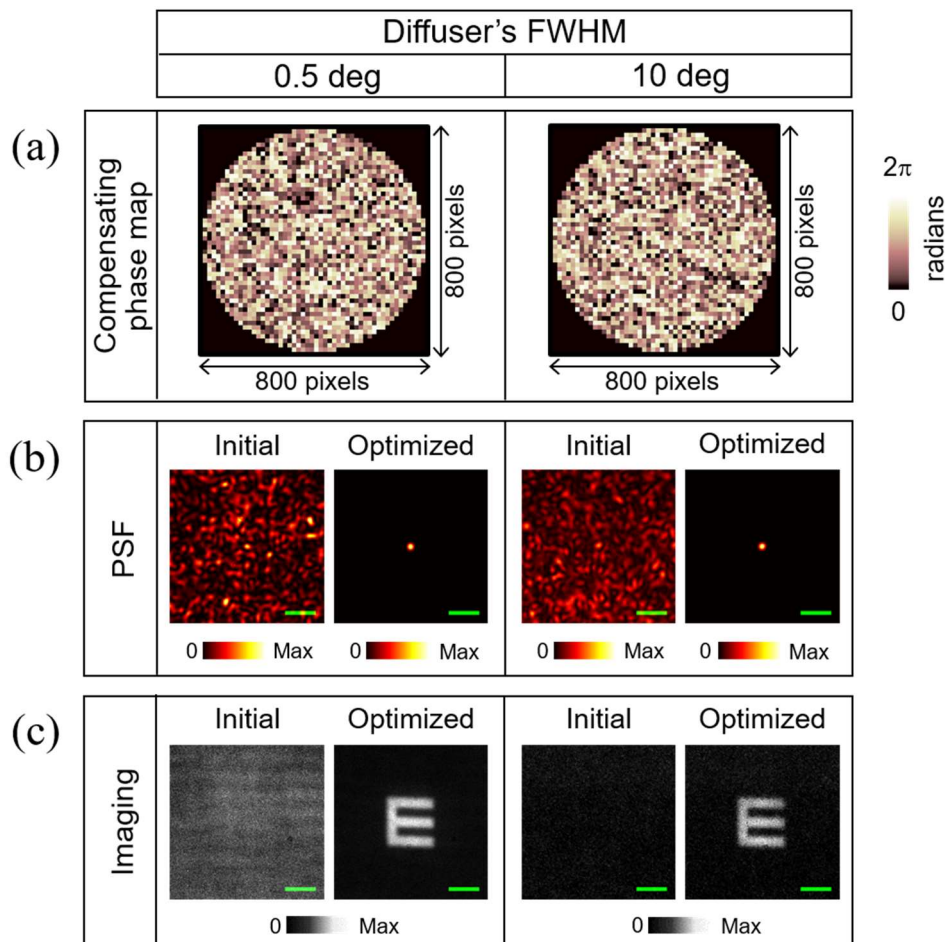
Figure 4-9. Minimization of the effects induced by physical diffusers. The length of the green bar is 5 arcmin.

The diffusers were placed in the AP plane of the experimental setup (see Figure 4-1), which is conjugated with the LCoS. While a flat wavefront is displayed in the first half of the modulator, the testing phase maps (contained in a matrix of 800x800 pixels) are displayed on the second half. Moreover, vertical and horizontal binary gratings were also

added for the suppression of the zero-diffraction order as it was explained in the previous section. The WS technique was implemented, filling the circular pupil of 1972 square segments with a size of 10x10 pixels in the matrix of the modulator. Figure 4-9a shows the compensating phase maps for both diffusers.

The initial and optimized PSFs are shown in Figure 4-9b. The PSF enhancements were 722 and 1141 for the diffuser with FWHM of 0.5 and 10 degrees, respectively. Moreover, the compensation effects were registered in extended images using spatially incoherent light, as shown in Figure 4-9c. After the optimization, an optotype with small angular size affected by the turbidity and turbulence becomes visible. In the case of the diffuser with 10 degrees of FWHM, the retrieved image looks noisy due to the required long exposure time (50 s) and maximum gain of the camera. The achieved improvement on both PSF and imaging proved the performance of the implemented WS technique to be applied in further experiments.

4.2.2 Simultaneous generation and correction of aberrations

In addition to the correction of the external induction of scattering and aberrations, a simple experiment was developed to compensate the aberrations displayed on the LCoS itself. Thus, two astigmatic phase maps representing astigmatisms of 0.5 D and 1 D were displayed on a half of the LCoS's area while in the second half were displayed the testing and correcting wavefronts. Once again, the WS was applied using 1972 segments of a pupil of 800x800 pixels of the LCoS, where the size of each segment was 10x10 pixels. Figure 4-10a shows the displayed the programmed aberrations and the corrector phase maps. Because the segment size was not sufficiently small to reproduce the high frequency oscillations in the aberrations, corrector wavefronts exhibits aliasing. It is more evident in the case of the astigmatism with high amplitude, as indicated by the red arrow in Figure 4-10a.

The comparison between the aberrated and optimized PSFs confirms the correction, shown in Figure 4-10b. The PSF correction has a direct impact on the improvement of the quality of an image seen after the double-pass through the LCoS. Figure 4-10c shows an uncorrected and corrected optotype for both amplitudes of astigmatism. The effect of the above referred aliasing in the phase maps is the appearance of 'parasitic' peaks around the central peak of the optimized PSF whose location depends on the segment size. In consequence, their effect on imaging are replicas of the object around the brightest image. Those effects on both the PSF and imaging are not shown in Figure 4-10b.

In conclusion, the instrument for imaging through scattering and aberrations using WS technique has been successfully tested. The experiments with external diffusers showed the ability of the instrument to compensate wavefront perturbations with low- and high- spatial frequencies corresponding to turbulence and turbidity conditions, respectively. Moreover, the WS performance for the compensation of aberrations depends on their amplitude and the segment size of the corrector wavefront. On the other hand,

the performance of the technique is mainly reduced by cross talk between pixels of the LCoS[159–161] and measurement noise. This instrument will be used in the following Chapter to minimize the effects of the simulated cataracts using the LCoS where scattering and aberrations are simultaneously induced.
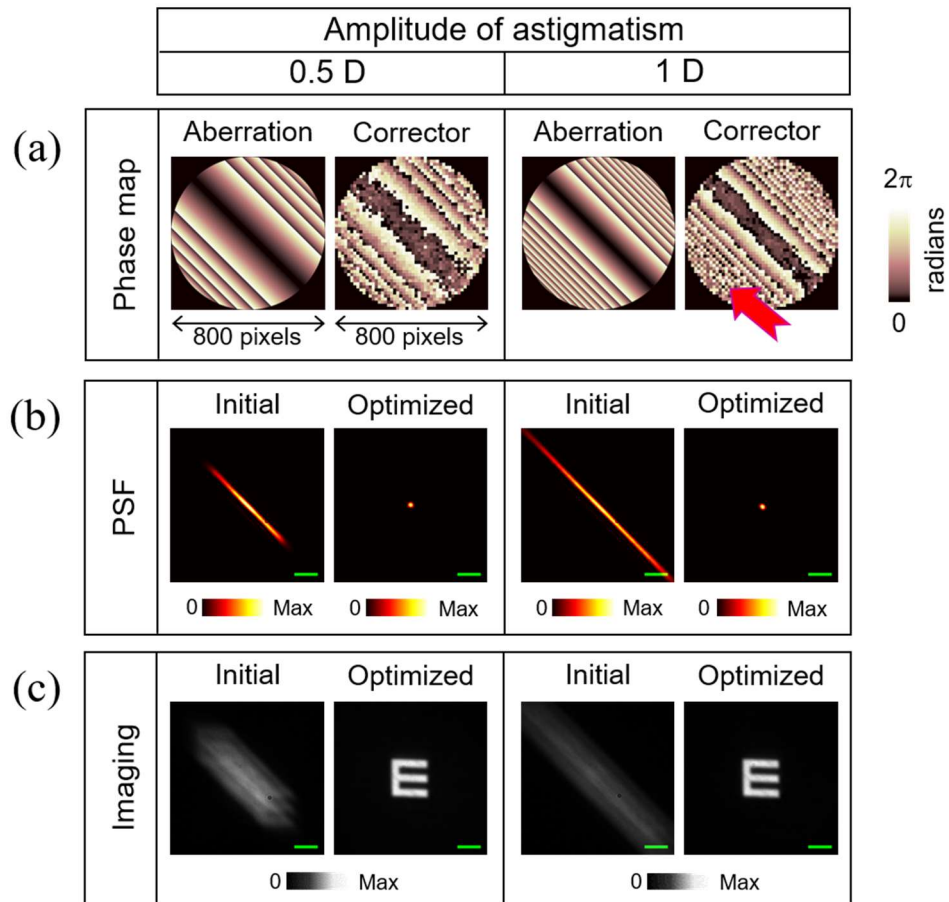
Figure 4-10. Compensation of the astigmatic phase maps displayed on the LCoS. The red arrow marks the aliasing in the corrector phase map. The length of the green bar is 5 arcmin.

5. CORRECTION OF CATARACTS USIGN WAVEFRONT SHAPING

In this Chapter, the calculated ocular phase maps were displayed on the LCoS device to test the performance of the WS technique in the correction of the effect of cataracts, simulating a single-pass through the ocular media.

The quality of the achieved correction was assessed using objective and subjective metrics. First, the enhancement of the PSF was estimated. In addition, two visually related optical metrics were evaluated: the visual Strehl ratio computed on the frequency domain and the correlation coefficient. The corresponding improvement on the visual acuity was also estimated in a group of healthy volunteers. The analysis of the WS performance is completed with the numerical calculation of the optimized wide-angle PSFs. Finally, based on the results, a complementary strategy to maximize the benefits of the WS correction was proposed.

5.1 Imaging through cataracts

The instrument used for the following experiments was presented in Section 4.1. The phase maps of three distinct straylights, generated using the model of phase perturbations (see Section 2.1), were displayed on the first half of the LCoS device while the testing or correcting phase maps were displayed in the other. Those straylight levels corresponding to a $Log_{10}[s]$ of 1.75, 2.00 and 2.25 at 3.5 degrees at retina, which can be clinically associated to nuclear opacifications ranked 3, 4 or higher in the LOCS-III scale[70]. In this way, the cataracts effects can be simultaneously reproduced and corrected using a single LCoS device. The size of both aberrated and correcting phase maps were 800 pixels, corresponding to an artificial pupil of 2.7 mm (diameter) because of the magnification of the telescope in the visual channel.

The testing wavefront was divided into regular segments by binning the pixels of the LCoS device. As one would expect, a high number of segments (i.e., small segment sizes) leads to high quality corrections[94], however, this could make inefficient the process increasing significantly the computational time. To find a trade-off between the quality of the correction and resolution, seven segment sizes were used for the correction: 80, 50, 40, 32, 25, 20 and 16 pixels of the modulator that correspond to 80, 208, 316, 491 812, 1266 and 1972 number of segments, respectively.

For the correction of each straylight level with each segment size, the following optical metrics were assessed: the enhancement of the PSF, the improvement on the Strehl ratio (calculated from the MTF), and the correlation coefficient of optotypes with different angular size. Additionally, the impact of the simulated effect of cataracts and its correction on the visual acuity were measured in healthy eyes. In this way, the

requirements for the suitable effect's correction of each amount of straylight were determined.

The methods to evaluate both optical and visual metrics are described in the following sub-sections. It is important to note that in the subsequent analysis, the angular sizes or spatial frequencies are referred to the retina plane of the subject, i.e. measured through the visual channel.

5.1.1 Enhancement of the PSF

Figure 5-1 shows the uncorrected and corrected coherent PSFs for the three straylight levels. For all the segment sizes, the corrected PSF consists of an energy peak, at the selected grain of speckle (i.e., the target) in the WS routine, over a background of uncorrected light.
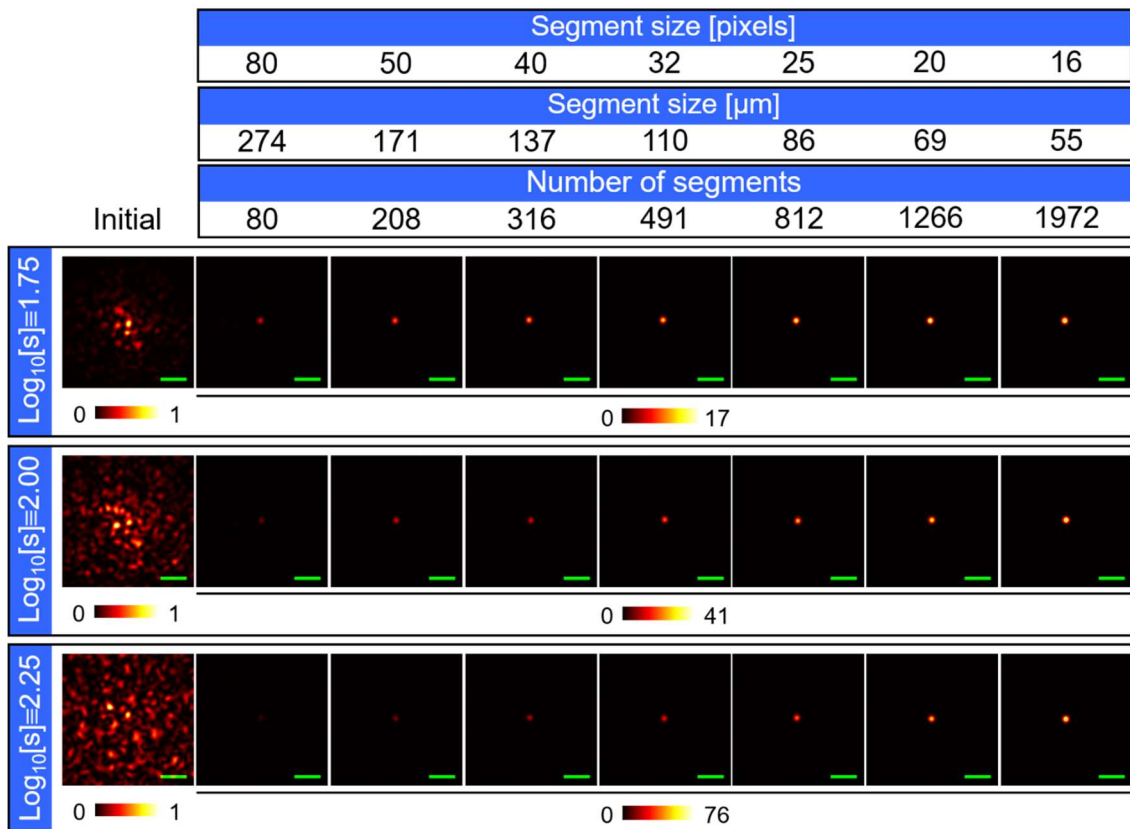
Figure 5-1. Effect of the WS correction on the PSF for each amount of straylight and several segment sizes. Length of green bar is 5 arcmin.

Figure 5-2 depicts the enhancement of the PSF, i.e. the ratio between the optimized intensity at target and the initial average of intensity around that position, as a function of the segment size. The shown values correspond to the average of three correction tests for each segment size and amount of straylight induced. This relationship is linear in the case of high-scattered samples (e.g., a layer of rutile pigment)[95], however, does not correspond to the simulated cataracts, even in the advanced stage. Evidently, the enhancement increases with the amount of straylight due to the reduction of the maximum

intensity at the uncorrected PSF. An enhancement threshold is observed for the correction of the lowest straylight level (Log$_{10}$[s]≡1.75) when the number of segments is larger than 1266 (or equivalently, segment sizes lower than 20 pixels).
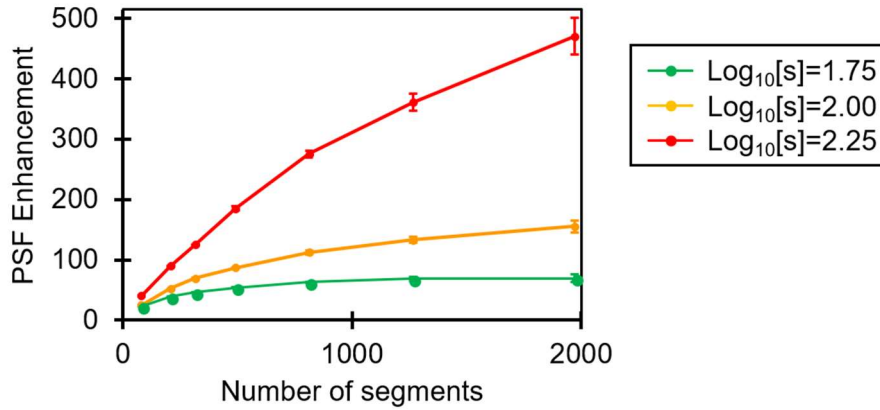
Figure 5-2. Evolution of the PSF enhancement with the segment sizes for each amount of straylight.

5.1.2 Objective evaluation of the improvement in imaging

Apart from the study of the PSF, there is a special interest on the improvement of spatially incoherent imaging. For this purpose, images of high-contrast binary objects with different angular sizes were acquired through the simulated cataracts and their corrections. Figure 5-3 shows an optotypes of an angular size of 7.6 arcmin uncorrected and corrected. An increase in straylight leads to a blur and reduces the intensity of images. Consequently, the correction would sharpen the image and increase its intensity. The correction's impact depends heavily on the segment size.

Two visually related optical quality metrics were used to evaluate the WS impact on the quality of image: the logarithm of the visual Strehl ratio and the correlation coefficient.

Log visual Strehl ratio computed from the MTF

The logarithm of the visual Strehl ratio computed in the frequency domain (LogVSMTF) can account up to 86% of the variance in high contrast LogMAR acuity[162,163]. Unlike Strehl ratio (Equation 2-4), the definition of this LogVSMTF includes a weighting of the radially averaged MTF by the neural contrast sensitivity function (*NCSF*)[6,7], as follows:

$$\text{LogVSMTF} = \text{Log}_{10}\left[\frac{\int_0^{f_{cutoff}} MTF(f)NCSF(f)df}{\int_0^{f_{cutoff}} MTF_{dl}(f)NCSF(f)df}\right] \quad (1)$$

where *f* is the spatial frequency, *f$_{cuttoff}$* is the cut-off frequency and *MTF$_{dl}$* is the diffraction-limited MTF. Here, *MTF$_{dl}$* corresponds to the MTF of the system with the compensation of the LCoS's aberrations.

Segment size [pixels]						
80	50	40	32	25	20	16
Segment size [µm]						
274	171	137	110	86	69	55
Number of segments						
80	208	316	491	812	1266	1972
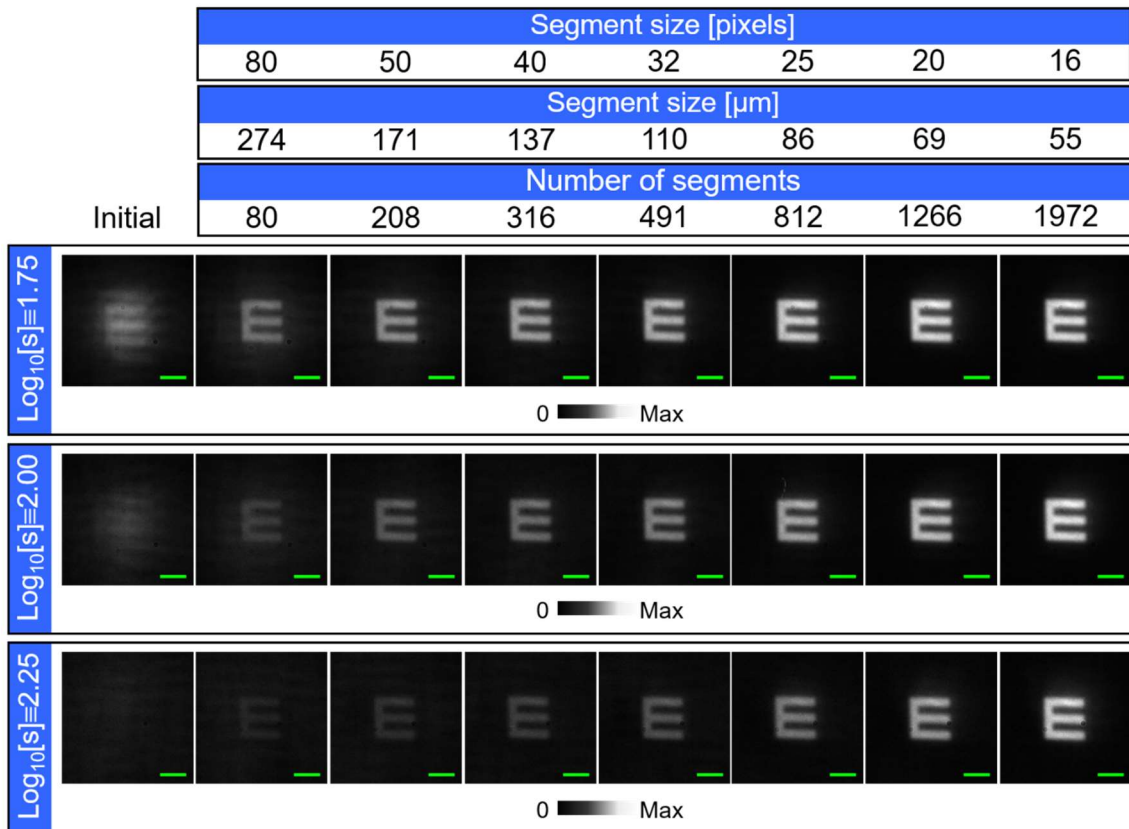
Figure 5-3. Imaging through the uncorrected and corrected generated intraocular scattering. Length of green bar is 5 arcmin.

The limited dynamic range of the camera could overestimate the MTFs directly calculated as the discrete Fourier transform of the acquired PSFs (Figure 5-1). Therefore, the MTFs was estimated imaging three or four bar-target patterns[164]. Essentially, in this frequency-by-frequency methodology, the MTF's amplitude at the fundamental frequency of the square-wave input is calculated as the ratio between the spectrum magnitudes of the output and the input bar-target. In our case, the radially averaged MTF was approximated to the average of the horizontal and vertical profiles. Moreover, the MTFs were discretized in seventeen spatial frequencies from 3 to 80 cpd. Figure 5-4 shows the estimated radially averaged MTFs.

As one would expect, MTF is severely reduced as the induced straylight increases. For each amount of straylight, the corrected MTF depends on the resolution (or sampling) of the correcting phase maps. In addition, WS process retrieves the MTF for spatial frequencies less than 60 cpd whose range has a visual impact.
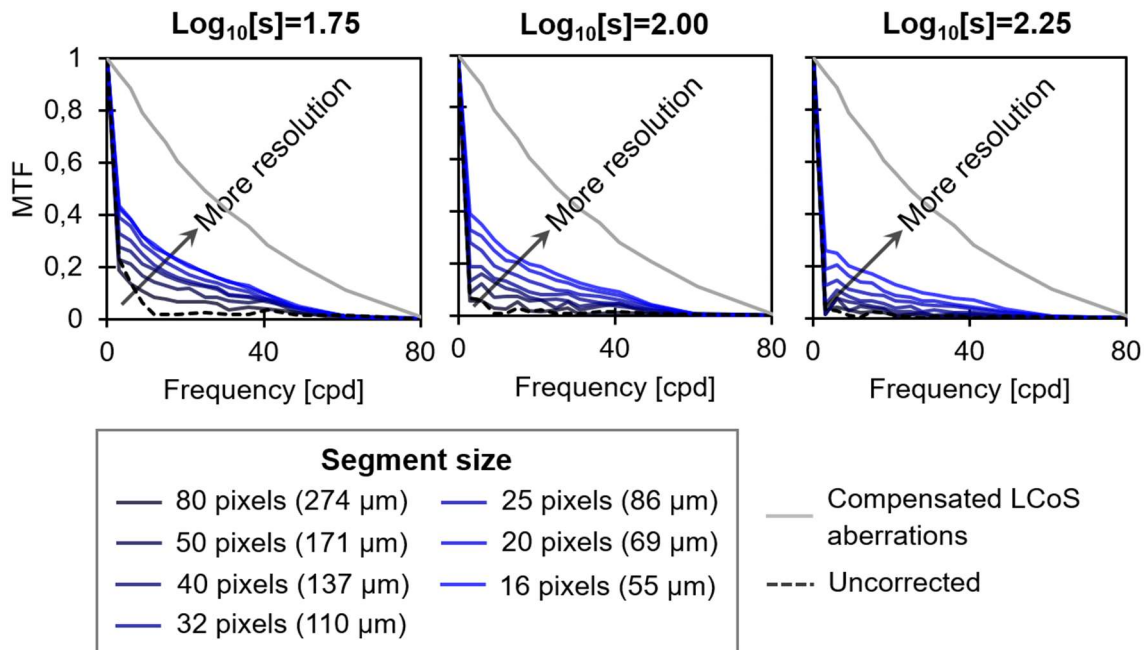
Figure 5-4. Uncorrected and corrected MTF for each amount of straylight and several segment sizes.

Figure 5-5 shows the LogVSMTF for the single-value inspection of uncorrected and corrected MTFs. In the case of a weak cataracts state (i.e., $Log_{10}[s] \equiv 1.75$), the LogVSMTF increases linearly with the logarithmic decrease of the segment size before it reaches a threshold, in line with the enhancement of the PSF (see Figure 5-2). The LogVSMTF curves of the other programmed amounts of straylight follow this tendency for lower segment sizes. The results suggest that the WS technique has a considerable impact on visual performance.
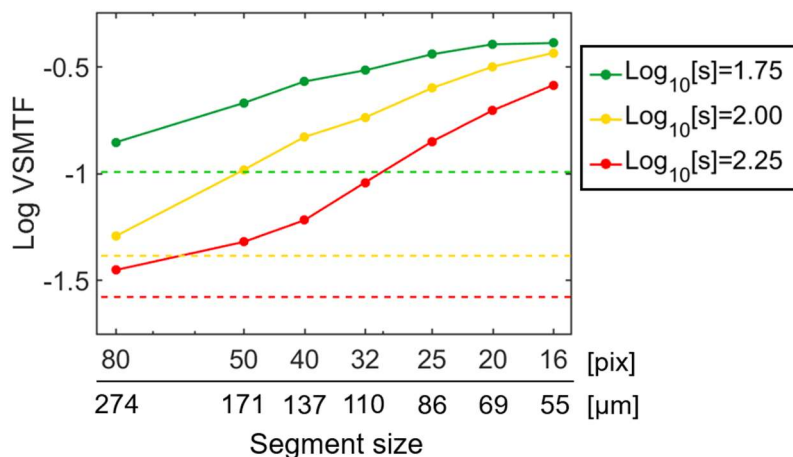
Figure 5-5. LogVSMTF on the frequency domain for each amount of straylight and the segment sizes. Dashed lines represent the uncorrected values.

Calculation of correlation coefficients

Pearson's coefficient, or correlation coefficient CR, is used for comparing discrepancies between two images. Likewise, it is a good descriptor of the visual acuity in highly

aberrated eyes[165]. Mathematically, CR is defined as the covariance of the reference (O) and degraded (I) images divided by the product of their standard deviations[166]:

$$CR = \frac{\sum_{i=1}^{M}(O_i-\bar{O})(I_i-\bar{I})}{\sqrt{\sum_{i=1}^{M}(O_i-\bar{O})^2}\sqrt{\sum_{i=1}^{M}(I_i-\bar{I})^2}} \qquad (2)$$

where M is the number of elements of both digitalized images. This metric is ranged from 0 to 1, the former when the images are completely uncorrelated and the latter when they are identical. Here, the reference image corresponds to the object recorded without straylight additions.

Initially, the CR of high-contrast optotypes for ten angular sizes were calculated for the three of straylight amounts and several segment sizes, as shown in Figure 5-6. In general, WS improves the CR up to values close to one. The higher CR values corresponds to lower segment sizes and large sized optotypes. Conversely, the CR is reduced for high binning sizes and large sized optotypes, as shown in some examples marked by an arrow in Figure 5-6, due to the contrast reduction. In those cases, the uncorrected scattering after the optimization process produces a luminance veil originating from the large sized optotypes itself.
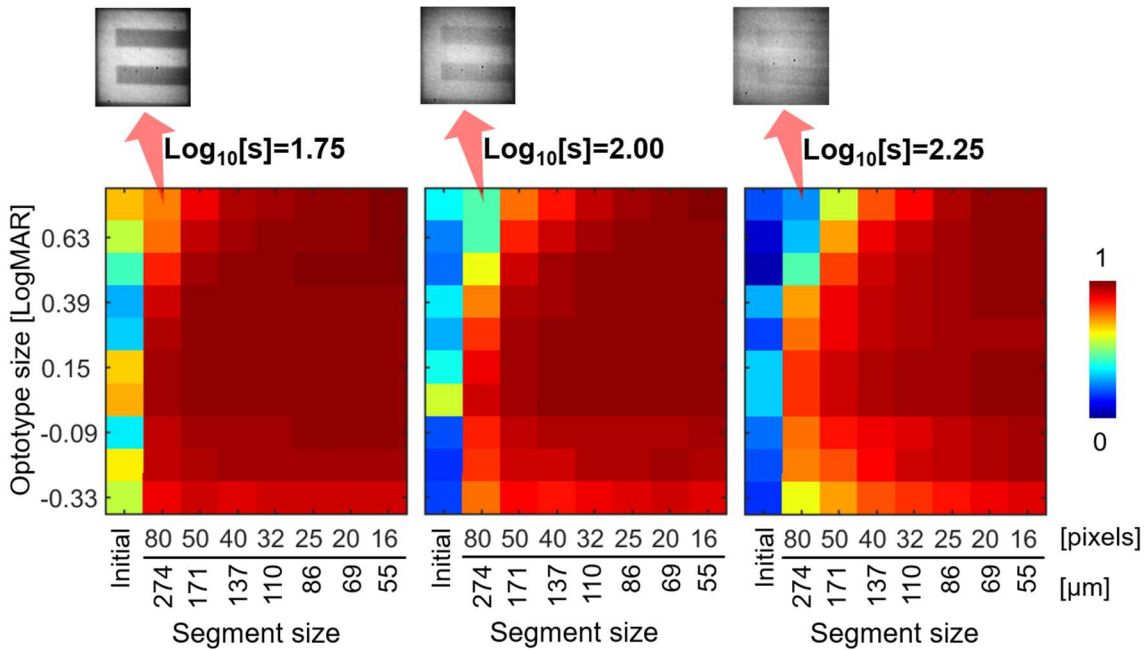
Figure 5-6. Correlation coefficients calculated on uncorrected (initial) and corrected optotypes for several angular sizes. The correlation decreases for large sized optotypes as consequence of the loss of contrast.

An additional experiment was carried out to estimate the dependence of the CR with the alignment between the aberrated and correcting phase maps. The correcting phase (displayed on a half of the modulator) was digitally displaced Δx microns in the horizontal axis with respect to the position of the aberrated phase (displayed on the other half). Figure 5-7a depicts the CR estimations for each Δx value, the three amounts of straylight

and the previously considered segment sizes using an optotype with angular size of 0.03 LogMAR. The different segment sizes are delimited with black rectangles within the CR maps. It is important to point out that the Δx values are referred at the pupil of the eye which is conjugated with the LCoS's pupil with a magnification of 0.43.

In general, the full width at half maximum (FWHM) of the CR profiles, across the Δx shifts- increases with the segment sizes. Theoretically, for high-scattering samples of 'zero' thickness, the correction will still work within a range of Δx determined by the maximum between the segment size and the transverse correlation length of the aberrated wavefront[97]. Therefore, the FWHM tends to be adjusted to the segment size (in microns) when the amount of straylight is increased because the effect of weak and intermediate cataracts cannot be described as high scattering samples, as it was previously disclosed (see Section 5.1.1).
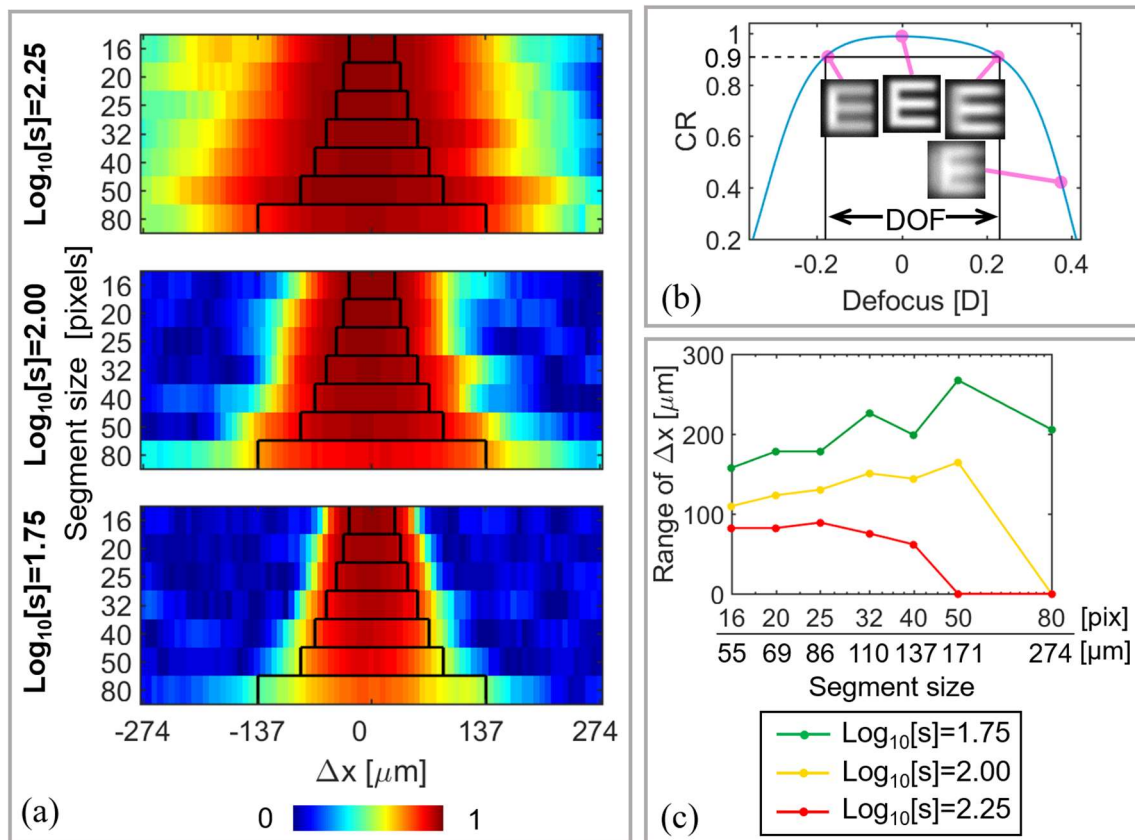
Figure 5-7. (a) Correlation coefficients across the Δx lateral shifts between cataractous and corrector phase maps and segment sizes for different straylight amounts; (b) Through-focus correlation coefficient calculated on a numerical simulated optotype; and (c) range of the lateral shifts where the correlation coefficients are higher than 0.9 in (a) for each amount of straylight.

Additionally, the CR surfaces shown in Figure 5-7a provide relevant information about the requirements of the pupil alignment for the projection of the corrector wavefront on the cataractous eye. It provides an estimation on the range of Δx where the optotype remains recognizable by the coupled system eye-brain. For each straylight amount and

segment size, the width of Δx that contains the CR values above a set threshold was assessed. To determine the threshold, the through-focus CR for a healthy eye ($Log_{10}[s] \equiv 0.7$) was numerically calculated using the current experimental parameters, picking out the value at the reported subjective depth-of-field (DOF) which is approximately 0.42 D for the considered pupil size[167]. The spatial features of both the LCoS and the camera were replicated in the matrices for the calculation of the through-focus PSFs applying the Fast Fourier transform[39]. Those PSFs were convolved with an optotype with an angular size of 0.03 LogMAR (the same used in the results shown in Figure 5-7a). The CR values were calculated for the convolved images by applying the Equation 5-2 to obtain the through-focus profile shown in Figure 5-7b. As a result, the CR threshold was 0.90. Finally, the Δx range where the optotype is recognizable, i.e. where CR is higher than the threshold, are shown in Figure 5-7c.

Assuming that the misalignment between the pupil of the cataractous eye and the corrector phase is caused by the fixational eye movements (FEMs), the following analysis on the ranges of Δx (Figure 5-7c) will determine if a corrector based on WS needs of a pupil tracker and, if yes, its requirements. FEMs are involuntary movements to overcome the loss of vision related to uniform stimulation of the retinal receptors[111] when the subject is staring at an object. Those movements are[168]: tremors, high frequency (~90 Hz) and wave-like motions with amplitude ranged from 0.08 to 0.7 deg/s (comparable to the diameter of a cone); drift, slow motions (less than 0.5 deg/s) with large amplitude ranged from 3 to 30 arcmin, moving away the target's image from the fovea; and microsaccades, fast (up to 120 deg/s) and jerk-like motions with amplitudes of up to 60 arcmin that compensate drift. The current analysis is based on the recent FEM's report[169] over a large healthy population using a high-speed pupil tracker and stabilizing the subject with the chin and forehead rest. Statistics of the pupil positions in the horizontal and vertical directions are 190±121 μm and 93±33 μm, respectively. Comparing those values with the ranges of Δx (Figure 5-7c), it is possible to infer that the correction of straylight effects generally will require pupil stabilization because the tolerance to misalignment were found to be lower than the FEM's amplitude, except in the case of the lowest straylight amount and larger segment sizes. Moreover, according to the same report[169], the incorporation of a pupil stabilization loop running at 30 Hz ensures a residual RMS of the FEMs to 30 μm, which is enough to correct the effects of straylight even for the higher amounts. The above can be extended to older subjects, who present high prevalence of cataracts[1], because there is no evidence that the age-related changes in the oculomotor affects the FEM[170].

Nevertheless, these reports didn't account for the blurring and contrast reduction of the target in the retina due to the scattering effects, which could increase the FEM's amplitude, hence, further research is necessary to determine the actual frequency of the pupil.

5.1.3 Subjective evaluation of the correction

In addition to objective metrics, the impact of the PSF correction on the visual acuity (VA) was assessed using the visual channel of the experimental setup (see Figure 4-2). The measurements were performed in the right eye of three trained subjects, without any known ocular pathologies, whose age and refraction were as follows: S1, 34, sphere -1.98 D, cylinder -0.38 D; S2, 28, sphere -0.52 D, cylinder -0.17 D; and S3, 31, sphere -1.94 D, cylinder -0.28 D. The spherical error for each eye was corrected using the LCoS device. The diameter of the artificial pupil is 2.7 mm. This size minimizes the effect of the natural aberrations of the eye and prevents the occlusion of the artificial pupil by the natural one, which is larger during the measurement due to the low light conditions in the experimental room.

For the threshold size measurement, a best parameter estimation by sequential testing (Best PEST) procedure was implemented[171]. The Best PEST method is a rapid and examiner-independent method where the step size of each trial is adjusted according to the information already gathered. The adjustment is guided by a psychometric function with a logistic shape and constant slope. The main goal is to search the angular size at the steepest slope of that function. The VA was set as the threshold size after 45 trials, enough for the convergence of the method, and converted to LogMAR units. For each trial, the task of the subject was to determine the orientation of a tumbling E typing the arrows of the keyboard. The stimuli were displayed on the DMD for 0.3 seconds after an acoustic signal. The available stimulus's sizes were linearly spaced from 0.45 to 44.55 arcmin.

VA is affected by two factors: quality of the, projected on the retina, image and luminance[172,173]. However, there is a luminance range where the VA is almost constant[172]. Therefore, in order to focus the subjective evaluation exclusively on the quality of the image, the VA with the natural aberration of each subject (except defocus) was preliminary assessed through an extended luminance range using neutral density filters. The luminance was estimated using a CMOS camera previously calibrated with a luminance meter (LS-100; Konica-Minolta Inc, Japan). Figure 5-8a shows the averaged VA for each subject after three measurements as well as the inter-subject average. The cyan bar depicts the corresponding luminance range of the stimulus seen through the corrected straylight effects. In that range, VA is almost constant ensuring that the observed are solely related to the optical quality of the retinal images. The average VA values agree with the reported measurements in the literature[174] using also an Maxwellian artificial pupil with a similar diameter (2.5 mm).

Based upon the above considerations, VA was measured before and after the WS correction. In addition, to equalize the luminance of the best corrected stimulus (i.e., the lowest binning size) for all amounts of straylight, the intensity was reduce using neutral density filters with optical densities of 0.4 and 0.3 when the $Log_{10}[s]$ is equals to 1.75 and

2.00, respectively. This procedure ensured that the stimuli luminance was within the cyan range, marked in the Figure 5-8a, throughout all VA assessments after the WS correction.

Figure 5-8b shows the inter-subject average VA for different segment sizes. Three tests were performed for each subject. These measurements validate both the procedure and the criteria for the estimation of the misalignment ranges between the aberrated and correcting wavefronts (see Figure 5-7c), based on the correlation analysis using an optotype with angular size of 0.03 LogMAR. The null ranges of Δx in Figure 5-7c, for $Log_{10}[s]$ equal to 2.00 and 2.25 and larger segment sizes, suggest that in those conditions the VA would be larger than 0.03 LogMAR, as confirmed by Figure 5-8b.
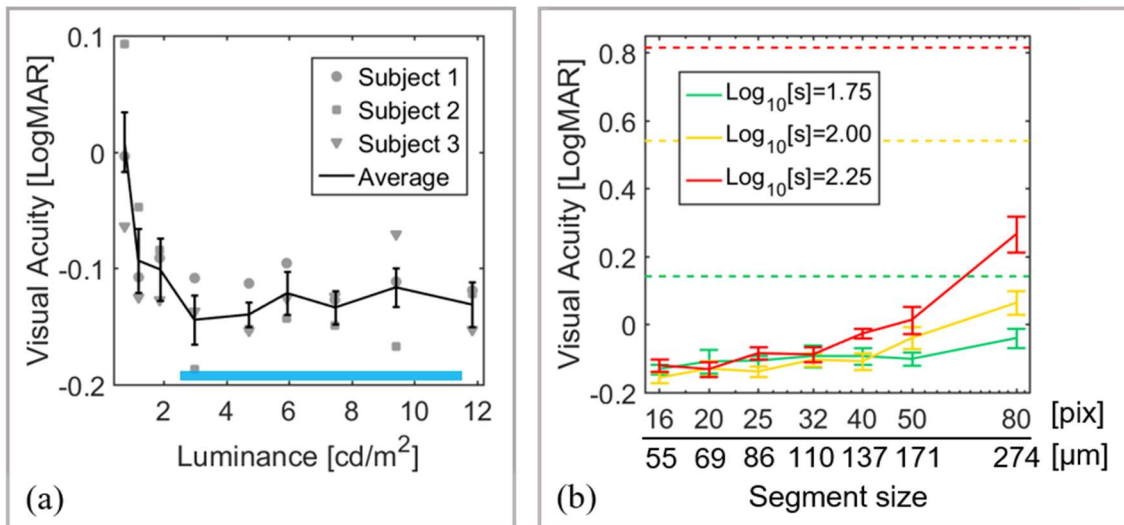
Figure 5-8. (a) High-contrast visual acuity as a function of the stimulus luminance. The cyan line delimits the adjusted luminance range of the corrected stimulus. (b) Averaged uncorrected (dashed lines) and corrected visual acuity across the three subjects versus the segment sizes for the three amounts of straylight. Error bars are inter-subject standard deviations.

According to the measurements, WS correction has a high impact on the VA, even for large segment sizes and high amounts of straylight. This is because, regardless of the straylight amount, the corrected PSF is a peak over a background and its relative height depends on the segment size (see Figure 5-1 and 5-2). Thus, while the protruding peak of energy deblurs the retinal image, the uncorrected scattering (the background in the PSF) results to a contrast reduction. Therefore, the VA is reduced when the segment size increases due to the loss of contrast. In fact, the contrast is not only reduced for small fields, but also on large fields too, as seen in Figure 5-6. In conclusion, the lack of contrast would be a serious limitation in the correction of cataracts using the WS technique. A detailed explanation and repercussions of this phenomena will be given in the following section.

5.2 Limits of the correction

As disclosed through both the objective and subjective metrics, WS technique primarily deblurs the retinal images and did not enhance completely their contrast. For a better

understanding of this performance, the uncorrected and corrected wide-angle PSFs were numerically calculated. Moreover, a physical simulation of a daytime scene as seen through a corrector of cataracts based on WS, was carried out. A solution to overcome this limitation is proposed.

5.2.1 Numerical calculations

The WS implementation and the subsequent experiments, were carried out to evaluate the improvement on resolution. Thus, in order to increase the sampling of the camera, a narrow field of view (~43 arcmin) was required. In addition, the restricted dynamic range of the camera did not allow the detailed inspection of the complete angular range of the PSF at the retinal plane (~4.5 degrees). Therefore, to evaluate the WS's effects on straylight, the uncorrected and corrected wide-angle PSFs were calculated for the three induced amounts of straylight, adopting the experimental parameters in the numerical simulation of the WS routine. The propagation of the optical field was calculated using the Fast Fourier transform[39] (see Section 1.1.3). Figure 5-9 shows the radially averaged PSF where the triangles mark the diffraction angles (ρ) associated to each binning size in the correcting wavefront. The ρ angle is given by $\sin^{-1}(\lambda/b)$, where λ and b are the wavelength and the segment size, respectively.
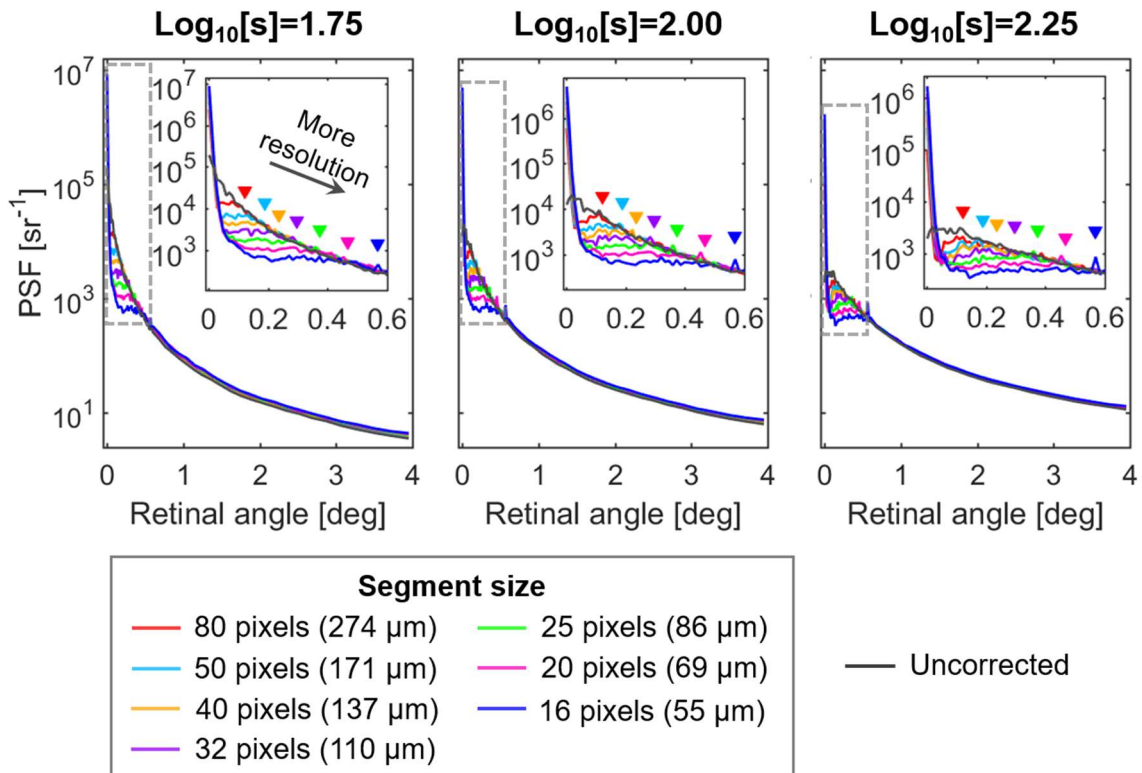
Figure 5-9. Numerical calculation of the correction's effects on the radially averaged wide-angle PSF with several segment sizes for the three considered amounts of straylight.

As shown in the magnified windows in Figure 5-9, the impact of the WS on the PSF is limited to the angular range of ρ where the light is spatially redistributed to form the central peak. In this way, the focus is recovered. However, WS did not correct straylight

and it would still affect the quality of vision. In principle, the ρ angle could be extended reducing the segment size as far as the SLM resolution, however, the minimum segment size will be constrained by the frame rate of both the SLM and the stabilization of the eye's pupil.

5.2.2 Overcoming the effects of the remaining scattering

The effects of the partial correction by the WS on a daytime scene are illustrated trough the sequence of images shown in Figure 5-10. Let's suppose that a subject with advanced cataracts (e.g., $Log_{10}[s]\equiv2.25$) is in front of a stairs whit lamps around (Figure 5-10a). The scene is indistinguishable due to cataracts, whose effects include blur, loss of contrast and reduction in intensity (Figure 5-10b). If the subject sees the stairs through an adaptive optics corrector based on WS (Figure 5-10c), the scene will look deblurred and more luminous, but the contrast will still be reduced due to straylight originating from the lamps or any bright point (e.g., diffuse reflections of the lamps). Hence, the localized impact of the WS technique couldn't be enough to improve the subject's perception.

Original scene
(a)

Cataract effects
(b)

Low-contrast corrected image
(c)
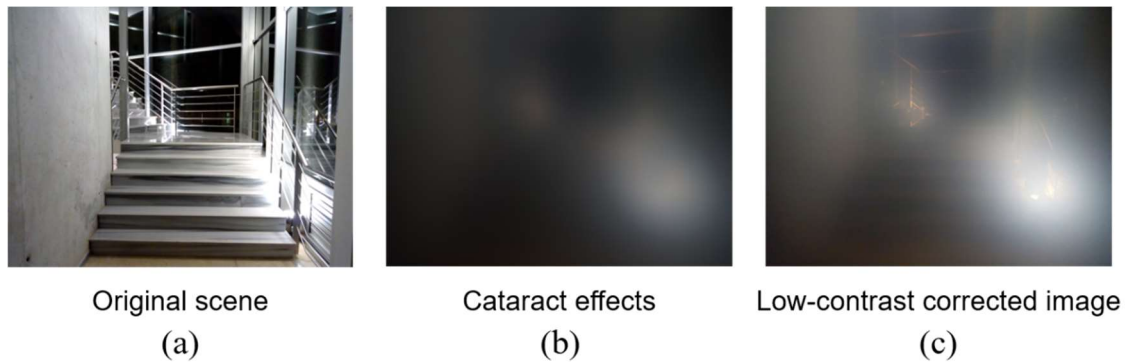
Figure 5-10. Scene seen through: (a) clear optics, (b) simulated cataracts and (c) corrected cataracts using WS.

To overcome this limitation, a simplification of the image projected on the retina is proposed. It would be carried out by an auxiliary camera and an appropriated real-time processing, attached to the WS corrector, with the following functions: to remove the glare sources and to identify the key information into the scene. Moreover, the simplified and corrected scene would be projected on the retina through a head-mounted display (HMD), being imposed to the image under the effect of cataracts to preserve some insight of the environment, e.g. surrounding luminance level.

The proposed simplification of Figure 5-10a is shown in Figure 5-11a. In this case, an edge-detection operation was simulated, creating a binary image where the structure of the stairs could be identified. As an experimental demonstration, this simplified image was introduced in the stimulus projection unit of the developed instrument (Figure 4-2) to be recorded under the partially compensated effects of straylight ($Log_{10}[s]\equiv2.25$) using a binning size of 55 μm. Figure 5-11b shows the retrieved simplified stimulus that was digitally added to the Figure 5-10b, simulating how it would be seen through the HMD.

Scene's simplification   High-contrast corrected image
        (a)   (b)
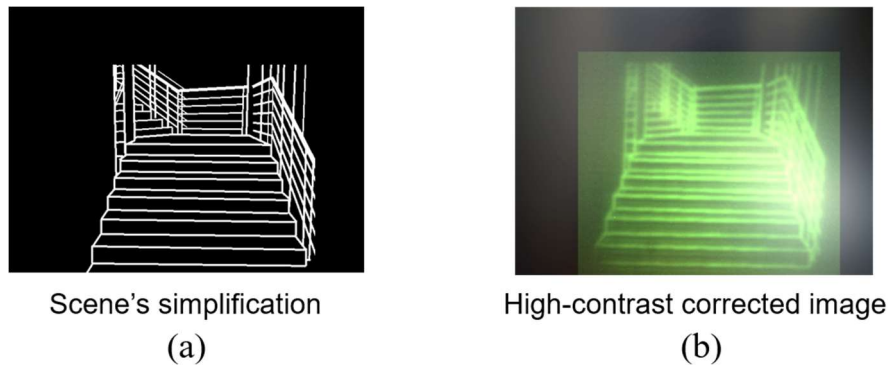
Figure 5-11. (a) Proposed simplification of the scene shown in Figure 5-10a like edge-detection process. (b) Experimental image of the simplified stimulus recorded through the instrument correcting an advanced cataract.

The original scene (Figure 5-10a) was acquired with a smartphone camera with clear optics. A round glass diffuser (DG-1500; Thorlabs GmbH, Germany) was put in front of the camera to reproduce both the uncorrected and the corrected effects of cataracts. The Fraunhofer pattern associated to this diffuser (shown in Figure 5-12a) consists of a high-intensity central peak over speckle. It mimics an optimized PSF by the WS method, producing a well-focused image added to the scattered light (Figure 5-10c). The generated amount of straylight (at 3.5 degrees) by this diffuser was $Log_{10}[s] \approx 2.25$, calculated from the normalized wide-angle PSF shown in Figure 5-12b. The enhancement of the PSF by this simulated correction is 4500. An estimated segment size of 36 μm is required to achieve that enhancement, according to a projection of the values shown in Figure 5-2. Finally, to simulate the uncorrected effect of cataracts, blur was added applying a digital gaussian filter to the Figure 5-10c and the brightness was reduced.
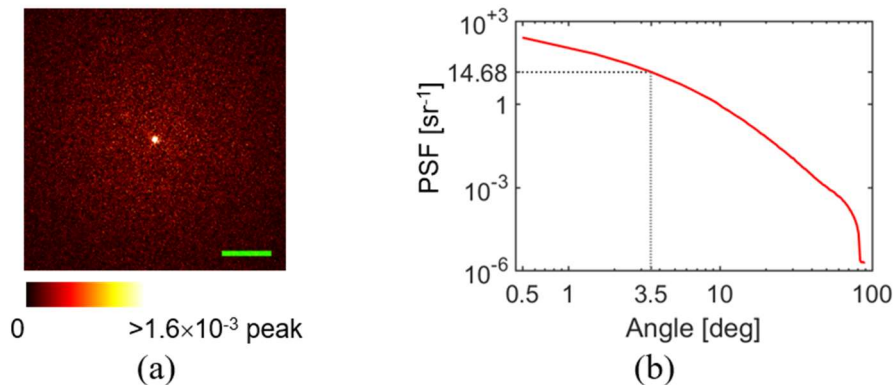
Figure 5-12. Optical response of the DG-1500 diffuser: (a) over-exposed bidimensional PSF and (b) the normalized wide-angle PSF estimated using the experimental data reported by the manufacturer[175]. Length of green bar is 5 arcmin.

6. PERFORMANCE OF THE WAVEFRONT SHAPING TECHNIQUE IN A DOUBLE-PASS SETUP AND FUTURE WORK

Considering that *in vivo*, the eye's responses are acquired using a double-pass through the ocular media, the performance of the WS technique was evaluated in this configuration using the instrument previously described in Chapter 4. Based on the obtained results, further requirements are discussed for the *in vivo* correction of the effect of cataracts.

6.1 Reproducing the double-pass PSF

Throughout the experiments performed in Chapter 5, the test beam was assumed to pass one time through the ocular media. However, the *in-vivo* WS application will require the double-pass (DP) technique to record the short-exposure ocular PSF. Therefore, the performance of the currently applied WS procedure was evaluated in a DP setup using the same instrument. The entrance and exit pupils of the DP were displayed in each half of the LCoS's area. Because the instrument allowed the complex modulation of optical field, unequal entrance and exit pupil sizes were reproduced.

Figure 6-1 illustrates the image formation process in the DP technique[176]. Following this formalism, the short-exposure double-pass PSF (DP PSF) is the squared modulus of the correlation between the first-pass (h_1) and second-pass (h_2) impulse responses:

$$DP\ PSF(x'', y'') = \left| \iint_{-\infty}^{\infty} h_2(x' + mx'', y' + my'') h_1(x', y') e^{iR(x', y')}\, dx' dy' \right|^2 \text{ (6-1)}$$

where m is the modulus of the magnification in the first pass ($m = |s'/s|$) and $R(x', y')$ denotes the random phases induced when light is backscattered from the mosaic of photoreceptors in the retina.

Physically, h_1 and h_2 impulse responses describe the effects of the diffraction at the pupil, aberrations and scattering on an idealized point source represented by the Dirac delta function $\delta(x, y)$. Considering a shift invariant optical system, h_1 and h_2 responses can be calculated as the Fourier transformation of the entrance $P_1(\xi_1, \eta_1)$ and exit $P_2(\xi_2, \eta_2)$ pupil functions respectively. Note that, according to the Figure 6-1, the wave aberrations (W) are the same for both passes, except for the change of sign. In the same way, the sign of the phase map displayed in the LCoS's half that corresponds to the second pass was changed.
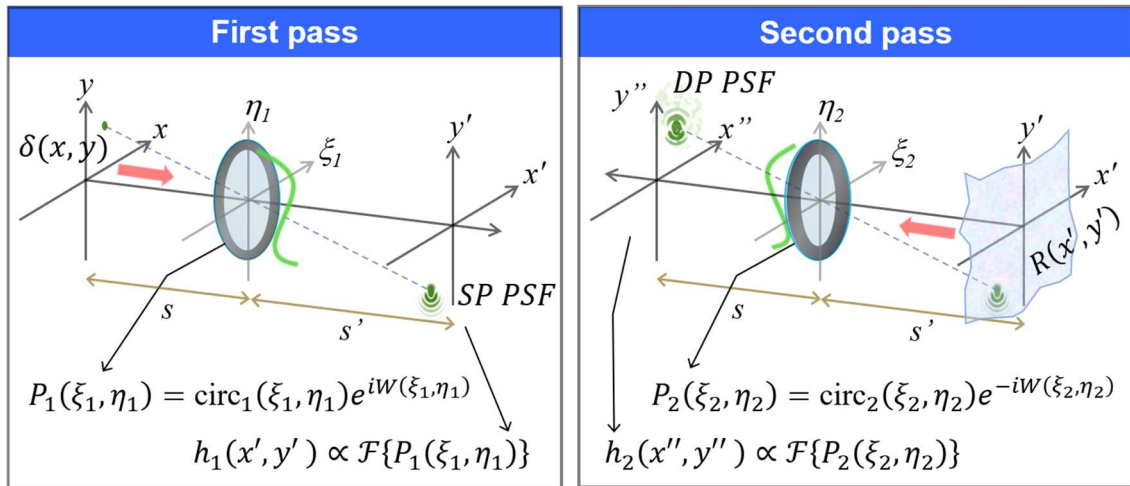
Figure 6-1. Image formation of a point spource $\delta(x, y)$ through a double-pass by an optical element with wavefront W. This corresponds to an asymetric setup because the unequal sizes of the entrance and exit pupils, which are given by the $\text{circ}_1(\xi_1, \eta_1)$ and $\text{circ}_2(\xi_2, \eta_2)$ functions, respectively.

The surface R in Equation 6-1 includes the effects of the light's interaction with the ocular fundus on the DP PSF. It adds speckle to the DP PSF under spatially coherent illumination[177]. One of the objectives of the following set of experiments is to evaluate the impact of this phenomenon on the WS correction. For this reason, a holographic diffuser (Luminit, USA) was placed at the focal plane on the conjugation path of the LCoS's areas (see Figure 4-1). This element produces a gaussian distribution of the light with a FWHM of one degree. Figure 6-2 depicts the effects of the diffuser's inclusion on the mimicked DP PSF of a young eye (i.e., $\text{Log}_{10}[s]\equiv0.8$ at 3.5 degrees). For this example, the programmed sizes of the entrance and exit pupils are 1 and 2.7 mm, respectively. The appearance of the simulated DP PSF (see Figure 6-2b) corresponds to the real short-exposure DP PSF using coherent sources[177,178].
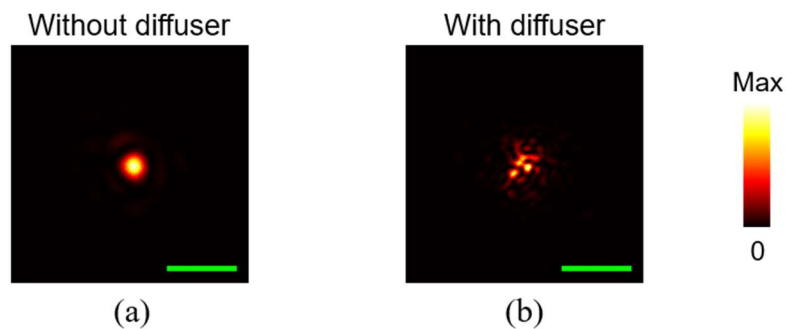
Figure 6-2. Experimentally reproduced asymmetrical DP PSF for a young eye (a) without and (b) with the effect of the light's interaction in the retina. Length of green bar is 5 arcmin.

6.2 WS correction in double-pass

The correcting wavefronts for three simulated cataractous eyes, with logarithmic amounts of straylight equal to 1.75, 2.00 and 2.25, were experimentally estimated considering four combinations of the entrance and exit pupil sizes:

- C1: The size of both entrance and exit pupils are 2.7 mm.
- C2: The size of the entrance and exit pupils are 1.0 and 2.7 mm, respectively. To reduce the impact of the aberrations on retinal focus, the entrance pupil size was reduced to 1.0 mm. This approach is commonly used in adaptive optics systems as an approximation to a single-pass measurement[179].
- C3: The size of the entrance and exit pupils are 0.5 and 2.7 mm, respectively. As the chosen straylight amounts are higher, to reduce even further the impact of the aberrations in the first pass, the entrance pupils size was reduced to 0.5 mm.
- C4: The size of the entrance and exit pupils are 2.7 and 0.5 mm, respectively. Unlike the previous setups, in this case the testing wavefront is projected within the incoming beam.

The testing wavefront was always assessed over the larger pupil of each shown configuration, which is contained in a matrix of 800×800 pixels in the LCoS. The correction's procedure for the DP PSF is the same of the previous experiments where, basically, the phase of each pupil segment is tuned to maximize the intensity in a selected grain of speckle. The segment size was fixed to 56 μm or 16 pixels of the LCoS. Figure 6-3 shows both uncorrected and corrected DP PSFs as well as their enhancements for the three amounts of straylight and each combination of the pupil sizes.

According to the Figure 6-3, after the WS application, the DP PSFs were improved for both symmetric and asymmetric setups. The enhancements are higher than those obtained in the previous Chapter (see Figure 5-2), confirming the increased deterioration of the DP PSF as consequence of the scattering in both the ocular media and the retina. However, the correction on the DP PSFs can't be associated to the improvement on the quality of vision, which occurs in a single-pass. To evaluate the enhancement on the single-pass (SP) PSF, the correcting wavefronts, properly conditioned for each configuration, were conjugated to the cataractous phase map in each half of the LCoS without the diffuser that simulates the retina, as it was done in previous Chapter. In this case, the size of the pupil is 2.7 mm. Figure 6-4 shows the effects of the DP correction on SP PSFs, including (in parenthesis) the coefficient between the Strehl ratios of the modified and uncorrected SP PSFs for each amount of straylight.

Clearly, the correction performed on the DP PSF using coherent light does not enhance the SP PSF. In fact, the correcting wavefronts in DP decrease the Strehl ratios of the SP PSF. The interaction of the light with the retina has a strong influence in the correction of the DP PSF using WS. As an evidence, those configurations (C2, C3 and C4) addressed to minimize the effect of the aberration in one pass did not improve the SP PSF. Another factor that has influence in those results is the difference of the pupil illumination during the correction in DP and the test of the corrector wavefront in SP. Under spatially coherent illumination and a short exposure regime, the pupil is illuminated with a non-uniform pattern due to the scattered light in the retina. It can

darken some regions of the pupil which cannot be corrected by WS routine in DP. Now, when the pupil is uniformly illuminated in the SP experiment, the previously darkened regions will contribute scattered light to the SP PSF. In consequence, a suitable solution to obtain a visual benefit from a WS correction in DP is to reduce the spatial coherence of the sources, suppressing the speckle in the DP PSF and making uniform the pupil's illumination.
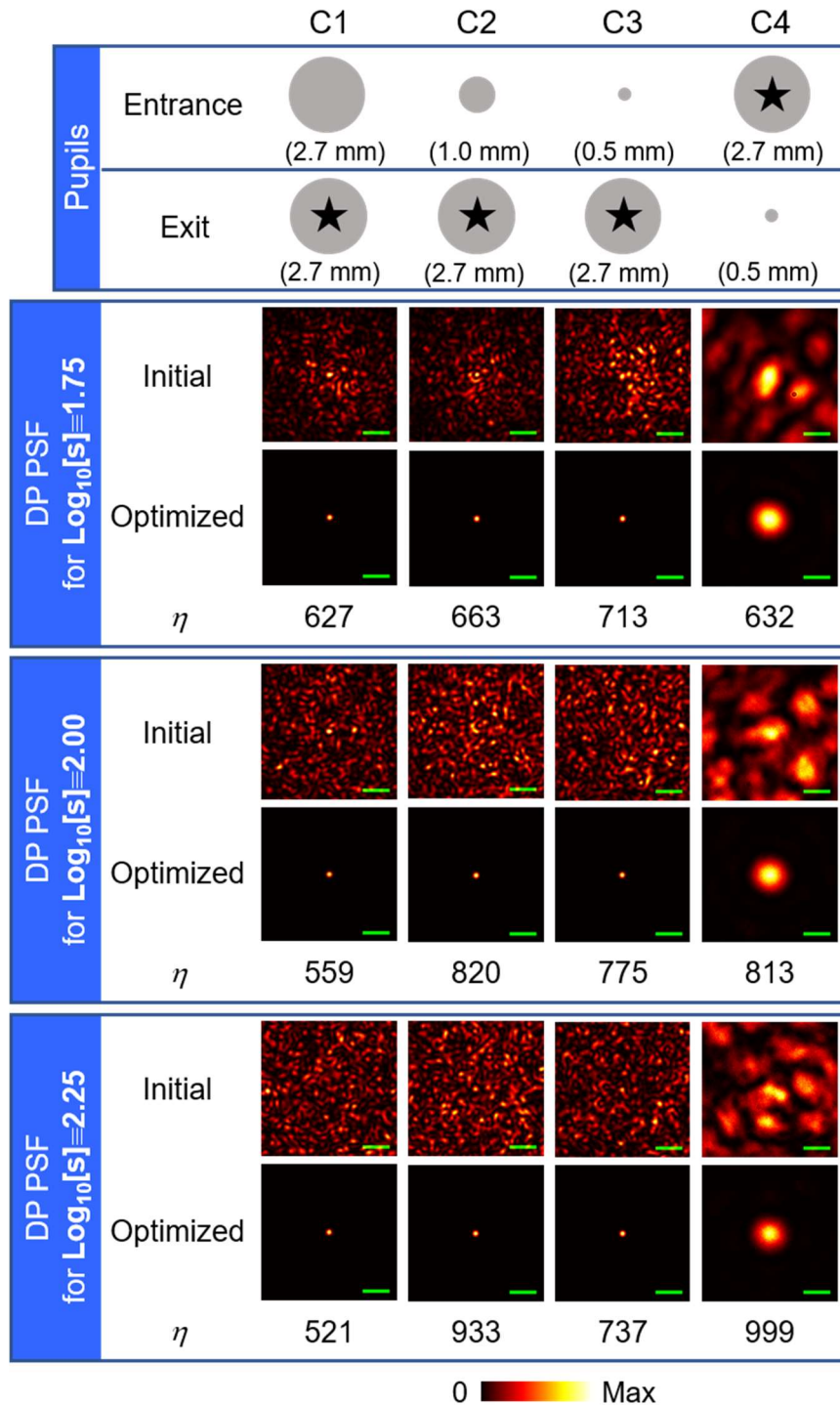
Figure 6-3. Uncorrected and corrected DP PSFs using WS technique for the considered combinations of entrance and exit pupil sizes (in parenthesis). The star marks the pupil where the testing wavefront was projected. Length of green bar is 5 arcmin.
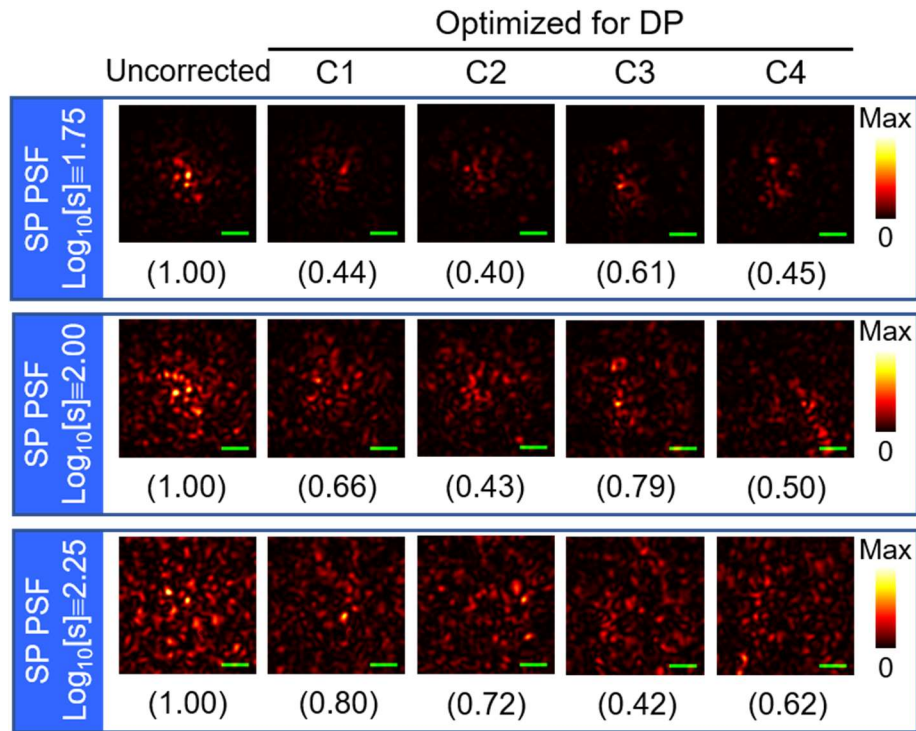
Figure 6-4. SP PSFs after the projection of the estimated corrector wavefronts in DP on the ocular phase maps. Length of green bar is 5 arcmin.

6.3 Future work

The main motivation of this thesis was the *in vivo* correction of cataracts using the WS technique. Hence, the following tasks are suggested to implement the WS technique in double-pass, what is relevant to the quality of vision:

- Incorporation of fast SLMs

A LCoS device was used for the simultaneous generation and correction of the intraocular scattering. Despite its limited frame rate, this device was very useful due to its high spatial resolution. However, a feasible *in-vivo* correction will need faster devices such as Digital Micromirror Device (DMD) whose typical frame rates are tens of kHz.

- The wavelength's selection of the testing beam

Longer wavelengths (i.e., > 600 nm) are suitable to be used in current adaptive optics systems because it produces high reflectance of the ocular fundus and the subject's comfort in the case of the infra-red where the eye is less sensitive[180,181]. On the other hand, the amount of straylight increases for longer wavelengths mainly due to the retinal diffusion instead of scattering in the ocular media[132], the phenomenon of interest. Thus, a study is necessary to solve this paradox between the minimization of the effects originated in the retina and the amplitude of the intensity signal.

- Reduction of the speckle in the DP PSF

The reduction of the speckle would allow: to isolate the effects of the ocular media, to make uniform the pupil illumination for the WS correction in DP, and to simplify the mathematical description of the DP PSF. Current methods to reduce the speckle at the DP PSF are based on time[129], space[182,183] and wavelength diversity. Space and time diversity approaches require some extension of the acquisition time to average the speckle, being generally larger for the time diversity. In principle, wavelength diversity, referred to the use of broadband lasers with low coherence length, can reduce the speckle in a short exposure time. However, several authors use additional methods for an effective reduction[178,182], reducing the rate of the correction. As a consequence, the selection of a method for the speckle suppression must be evaluated because its direct impact on the temporal frequency of the wavefront correction.

- Re-evaluation of the merit function

If speckle is reduced, the DP PSF will be mainly influenced by the scattering in the ocular media. At this point, the merit function that guides the WS routine must be re-evaluated. In eyes with a moderate amount of scattering, the DP PSF can be approximated to a diffraction-limited PSF correlated with the SP PSF when the entrance pupil size is sufficiently reduced[179]. In that case, the suggested goal of the WS routine is simply to maximize the Strehl ratio of the DP PSF. Nevertheless, it could not be applicable to the case of cataractous eyes because of advanced deterioration of the SP PSF even for small pupils. Therefore, the following disclosed challenge is the re-definition of the merit function to ensure the improvement of the quality of vision above the mere DP PSF compensation.

7. CONCLUSIONS

These are the main conclusions of the work:

1. A new model for designing random phase maps that replicate the angular distribution of intraocular straylight (i.e., the ocular PSF values at large retinal angles) was developed. The generated amounts of straylight by this model were experimentally verified using a setup with a liquid crystal display as spatial phase modulator.

2. The model was extended to accurately reproduce the ocular PSF in the whole angular range, including the domain of the HO aberrations. The aging effects on HO-RMS and SR, the wavelength dependence of straylight and the appearance of the ciliary corona were numerically replicated being compared with clinical and experimental results previously reported.

3. A visual simulator was developed to induce scatter by displaying the generated phase maps based on a LCoS device. Visual tests (on the fovea and two retinal eccentricities) were performed inducing several amounts of straylight. Visual acuity (in LogMAR units) linearly increases with the amount of straylight. Moreover, the logarithm of contrast sensitivity (at 3 cycles per degree) is linearly reduced as the amount of straylight increases.

4. An instrument for the simultaneous generation of the straylight effects and their correction using the WS technique was developed. The instrument uses a double-pass through a single LCoS-SLM. Its performance was proved by retrieving the image under turbulence and turbid effects.

5. The effects of three induced amounts of straylight, associated to three cataract levels, were corrected using seven segment sizes (from 55 to 274 μm) of the testing and correcting wavefronts. The corrections were initially performed considering a single-pass through the ocular media, providing the most promising performance of this technique.

6. In general, the main effect of the WS correction was deblurring. However, the quality of the correction, related to the maximum intensity of the optimized PSF, was dependent of the segment size. A threshold of both the enhancement of the PSF and the visual SR was found when the effects of weak cataract (i.e., $Log_{10}[s] \equiv 1.75$) were corrected using segment sizes lower than 69 μm.

7. The range of lateral displacements between to the cataractous phase maps and the correcting wavefronts where a small sized optotype could be recognized was estimated for each straylight amount by an analysis on the correlation coefficients.

Those ranges were 158, 110 and 82 μm for $Log_{10}[s]$ equivalent to 1.75, 2.00 and 2.25, respectively. Because the amplitude of the fixational eye movements are higher than those ranges, a pupil tracker could be required in a future *in-vivo* implementations of scatter correction.

8. The WS technique did not have impact on the corrected amount of straylight because its angular range of influence is narrow (up to 0.56 degrees), which was determined by the spatial resolution of the correcting wavefront. A possible strategy on the image projection was proposed to overcome the contrast reduction because of the uncorrected scattering.

9. The instrument was modified to evaluate the performance of the WS technique simulating symmetric and asymmetric double-pass through the ocular media. The WS correction was influenced by the scattering at the retina when coherent light was used. This affected the improvement of the quality of vision.

A. APPENDIX: PHASE CALIBRATION OF THE LIQUID CRYSTAL DEVICE

The phase calibration of the LCoS device is the linearization process of the phase modulation (between 0 and 2π radians) as function of the gray levels programmed on the computer. An accurate evaluation of the phase modulation is necessary for the calibration process. Here, the phase modulation is evaluated implementing a simple interferometric method[184], which is based on the projection of a binary grating on a half of the LCoS area while uniform background with σ gray level is projected on another half. An interference pattern arises as result of the propagation of both halves when the LCoS is illuminated by a monochromatic and spatially coherent laser beam. A horizontal polarizer oriented with the director axis of the parallel aligned liquid crystal molecules, is placed in front of the camera to avoid the effects of the unmodulated light by the LCoS. The displacement of the straight fringes is directly related to the average phase introduced by each σ gray level. The height of the binary grating is selected to maximize the fringe contrast. Figure A-1 shows the optical layout of the experimental setup and the fringes for several σ values.
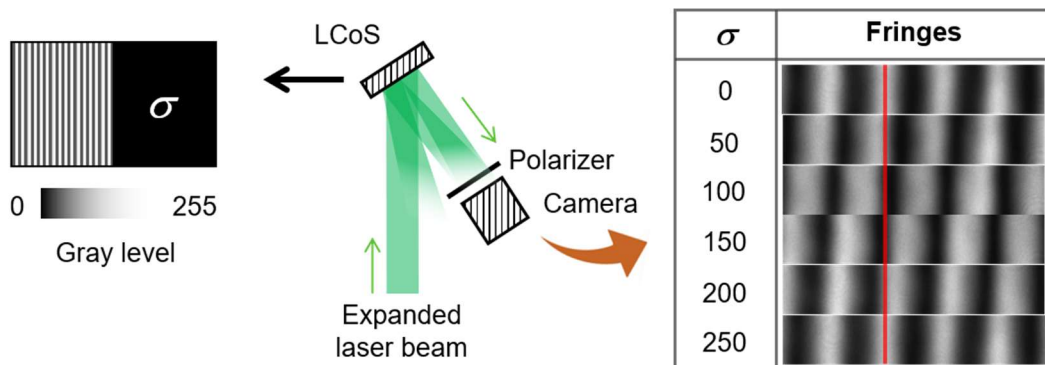
Figure A-1. Setup for the phase calibration of the LCoS. The phase induced by the σ gray level is assessed through the shifting fringes produced by the interference between both LCoS's halves (café wall illusion can be observed in the stacked fringes). The linear polarizer in front of the camera selects only the modulated light.

The LCoS driver internally converts the gray levels to voltage signals through a look-up table (LUT). For the calibration process, the parameters of the LCoS driver are fixed: voltage sequence (5_6, given by default), and the maximum (3.92 V) and minimum (1.22 V) operative voltages applied to each cell. The phase is initially evaluated as function of gray levels setting a linear LUT. This first result is used for the linearization of the phase response through the LUT correction[184]. Figure A-2 shows the LUT and phase modulation before and after the calibration. Thus, the performance of wrapped phase elements displayed on the LCoS is optimized.
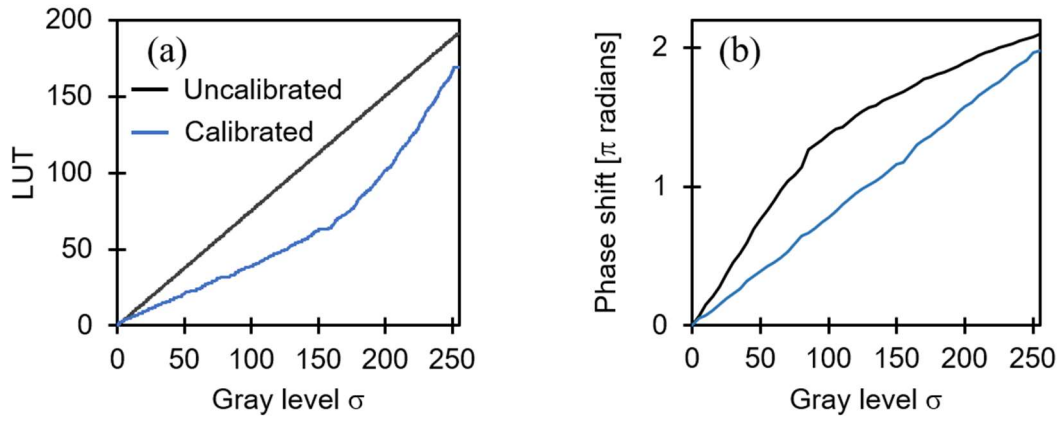
Figure A-2. Uncalibrated and calibrated: (a) look-up table (b) phase modulation.

BIBLIOGRAPHY

1. R. R. A. Bourne, S. R. Flaxman, T. Braithwaite, M. V Cicinelli, A. Das, J. B. Jonas, J. Keeffe, J. H. Kempen, J. Leasher, H. Limburg, K. Naidoo, K. Pesudovs, S. Resnikoff, A. Silvester, G. A. Stevens, N. Tahhan, T. Y. Wong, … Y. Zheng, "Magnitude, temporal trends, and projections of the global prevalence of blindness and distance and near vision impairment: a systematic review and meta-analysis," Lancet. Glob. Heal. **5**, e888–e897 (2017).

2. M. J. Cox, "Optics of the Human Eye D.A. Atchison, G. Smith; Butterworth-Heinemann, Oxford, 2000, 269 pages, ISBN 0-7506-3775-7, f27.50," Ophthalmic Physiol. Opt. **21**, 426–426 (2001).

3. J. F. Koretz, C. A. Cook, and J. R. Kuszak, "The zones of discontinuity in the human lens: development and distribution with age," Vision Res. **34**, 2955–62 (1994).

4. M. Bahrami, M. Hoshino, B. Pierscionek, N. Yagi, J. Regini, and K. Uesugi, "Optical properties of the lens: An explanation for the zones of discontinuity," Exp. Eye Res. **124**, 93–99 (2014).

5. S. J. Ryan, "Anatomy and Physiology," in *Retina*, David R. Hinton, ed. (Elsevier/Mosby, 2006).

6. F. W. Campbell and D. G. Green, "Optical and retinal factors affecting visual resolution," J. Physiol. **181**, 576–593 (1965).

7. A. B. Watson and A. J. Ahumada, "A standard model for foveal detection of spatial contrast," J. Vis. **5**, 6 (2005).

8. H. von Helmholtz, *Popular Scientific Lectures* (Dover, 1962).

9. P. Artal, A. Guirao, E. Berrio, and D. R. Williams, "Compensation of corneal aberrations by the internal optics in the human eye," J. Vis. **1**, 1 (2001).

10. P. Artal and A. Guirao, "Contributions of the cornea and the lens to the aberrations of the human eye," Opt. Lett. **23**, 1713 (1998).

11. P. Artal, E. Berrio, A. Guirao, and P. Piers, "Contribution of the cornea and internal surfaces to the change of ocular aberrations with age.," J. Opt. Soc. Am. A, **19**, 137–43 (2002).

12. R. A. Applegate, W. J. Donnelly, J. D. Marsack, D. E. Koenig, K. Pesudovs, and K. Pesudovs, "Three-dimensional relationship between high-order root-mean-square wavefront error, pupil diameter, and aging," J. Opt. Soc. Am. A **24**, 578–87 (2007).

13. M. Lombardo and G. Lombardo, "New methods and techniques for sensing the wave aberrations of human eyes," Clin. Exp. Optom. **92**, 176–186 (2009).

14. P. M. Prieto, F. Vargas-Martín, S. Goelz, and P. Artal, "Analysis of the performance of the Hartmann–Shack sensor in the human eye," J. Opt. Soc. Am. A **17**, 1388–1398 (2000).

15. L. N. Thibos, R. A. Applegate, J. T. Schwiegerling, R. Webb, and VSIA Standards Taskforce Members. Vision science and its applications, "Standards for reporting the optical aberrations of eyes," J. Refract. Surg. **18**, S652-60 (2002).

16. R. J. Noll, "Zernike polynomials and atmospheric turbulence," J. Opt. Soc. Am. **66**, 207 (1976).

17. R. A. Applegate, C. Ballentine, H. Gross, E. J. Sarver, and C. A. Sarver, "Visual Acuity as a Function of Zernike Mode and Level of Root Mean Square Error," Optom. Vis. Sci. **80**, 97–105 (2003).

18. G. M. Perez, S. Manzanera, and P. Artal, "Impact of scattering and spherical aberration in contrast sensitivity," J. Vis. **9**, 19–19 (2009).

19. G. Dai, "Wavefront expansion basis functions and their relationships," J. Opt. Soc. Am. A **23**, 1657 (2006).

20. J. P. Trevino, J. E. Gómez-Correa, D. R. Iskander, and S. Chávez-Cerda, "Zernike vs. Bessel circular functions in visual optics," Ophthalmic Physiol. Opt. **33**, 394–402 (2013).

21. P. Artal, "Image Formation in the Living Human Eye," Annu. Rev. Vis. Sci. **1**, 1–17 (2015).

22. T. J. T. P. van den Berg and K. E. W. P. Tan, "Light transmittance of the human cornea from 320 to 700 nm for different ages," Vision Res. **34**, 1453–1456 (1994).

23. T. J. T. P. van den Berg, L. J. van Rijn, R. Michael, C. Heine, T. Coeckelbergh, C. Nischler, H. Wilhelm, G. Grabner, M. Emesz, R. I. Barraquer, J. E. Coppens, and L. Franssen, "Straylight Effects with Aging and Lens Extraction," Am. J. Ophthalmol. **144**, 358–363 (2007).

24. T. J. T. P. van den Berg, J. K. Ijspeert, and P. W. T. de Waard, "Dependence of intraocular straylight on pigmentation and light transmission through the ocular wall," Vision Res. **31**, 1361–1367 (1991).

25. T. J. T. P. van den Berg, L. Franssen, and J. E. Coppens, "Ocular media clarity and straylight," in *Encyclopedia of the Eye* (Elsevier/Academic Press, 2010), pp. 173–183.

26. T. J. T. P. van den Berg and H. Spekreijse, "Light scattering model for donor lenses as a function of depth," Vision Res. **39**, 1437–1445 (1999).

27. L. T. Chylack, J. K. Wolfe, D. M. Singer, M. C. Leske, M. A. Bullimore, I. L. Bailey, J. Friend, D. McCarthy, and S.-Y. Wu, "The Lens Opacities Classification System III," Arch. Ophthalmol. **111**, 831 (1993).

28. W. S. Stiles and B. H. Crawford, "The Effect of a Glaring Light Source on Extrafoveal Vision," Proc. R. Soc. B Biol. Sci. **122**, 255–280 (1937).

29. T. J. T. P. van den Berg, "On the relation between intraocular straylight and visual function parameters," Invest. Ophthalmol. Vis. Sci. **35**, 2659–2661 (1994).

30. J. J. Vos, "On the cause of disability glare and its dependence on glare angle, age and ocular pigmentation," Clin. Exp. Optom. **86**, 363–370 (2003).

31. J. J. Vos, "Reflections on glare," Light. Res. Technol. **35**, 163–176 (2003).

32. J. J. Vos, B. L. Cole, H.-W. Bodmann, E. Colombo, T. Takeuchi, and T. J. T. P. van den Berg, *CIE Equations for Disability Glare* (2002).

33. J. A. Stratton, *Electromagnetic Theory* (IEEE Press, 2007).

34. I. Kelly-Pérez, N. c. Bruce, L. R. Berriel-Valdos, A. Werner, and J. A. Delgado Atencio, "Computational model of the effect of light scattering from cataracts in the human eye," J. Opt. Soc. Am. A **30**, 2585–2594 (2013).

35. M. J. Costello, S. Johnsen, K. O. Gilliland, C. D. Freel, and W. C. Fowler, "Predicted Light Scattering from Particles Observed in Human Age-Related Nuclear Cataracts Using Mie Scattering Theory," Investig. Opthalmology Vis. Sci. **48**, 303 (2007).

36. H. C. van de Hulst, *Light Scattering by Small Particles* (Dover , 1981).

37. J. E. Coppens, L. Franssen, and T. J. T. P. van den Berg, "Wavelength dependence of intraocular straylight," Exp. Eye Res. **82**, 688–692 (2006).

38. J. W. Goodman, *Introduction to Fourier Optics* (Roberts & Co, 2005).

39. D. Mas, J. Garcia, C. Ferreira, L. M. Bernardo, and F. Marinho, "Fast algorithms for free-space diffraction patterns calculation," Opt. Commun. **164**, 233–245 (1999).

40. M. Sypek, "Light propagation in the Fresnel region. New numerical approach," Opt. Commun. **116**, 43–48 (1995).

41. C. Kniestedt and R. Stamper, "Visual acuity and its measurement," Ophthalmol. Clin. North Am. **16**, 155–170 (2003).

42. D. G. Pelli and P. Bex, "Measuring contrast sensitivity," Vision Res. **90**, 10–14 (2013).

43. R. Michael and A. J. Bron, "The ageing lens and cataract: a model of normal and pathological ageing," Philos. Trans. R. Soc. Lond. B. Biol. Sci. **366**, 1278–92 (2011).

44. F. Boscia, I. Grattagliano, G. Vendemiale, T. Micelli-Ferrari, and E. Altomare, "Protein oxidation and lens opacity in humans," Invest. Ophthalmol. Vis. Sci. **41**, 2461–5 (2000).

45. G. B. Benedek, "Theory of transparency of the eye," Appl. Opt. **10**, 459–73 (1971).

46. D. Kaimbo Wa Kaimbo, "Cataracts: Epidemiology, Morphology, Types and Risk Factors," in *Cataracts and Cataract Surgery : Types, Risk Factors, and Treatment Options*, Didier Navarro, ed. (Nova Science Publishers, 2013), p. 163.

47. T. Kuroda, T. Fujikado, N. Maeda, T. Oshika, Y. Hirohara, and T. Mihashi, "Wavefront analysis in eyes with nuclear or cortical cataract," Am. J. Ophthalmol. **134**, 1–9 (2002).

48. T. Kuroda, T. Fujikado, N. Maeda, T. Oshika, Y. Hirohara, and T. Mihashi, "Wavefront analysis of higher-order aberrations in patients with cataract," J. Cataract Refract. Surg. **28**, 438–44 (2002).

49. T. Fujikado, T. Kuroda, N. Maeda, S. Ninomiya, H. Goto, Y. Tano, T. Oshika, Y. Hirohara, and T. Mihashi, "Light scattering and optical aberrations as objective parameters to predict visual deterioration in eyes with cataracts," J. Cataract Refract. Surg. **30**, 1198–1208 (2004).

50. T. Mihashi, Y. Hirohara, K. Bessho, N. Maeda, T. Oshika, and T. Fujikado, "Intensity analysis of Hartmann-Shack images in cataractous, keratoconic, and normal eyes to investigate light scattering," Jpn. J. Ophthalmol. **50**, 323 (2006).

51. C. Z. Wu, H. Jin, Z. N. Shen, Y. J. Li, and X. Cui, "Wavefront aberrations and retinal image quality in different lenticular opacity types and densities," Sci. Rep. **7**, 15247 (2017).

52. K. Pesudovs and D. B. Elliott, "Refractive error changes in cortical, nuclear, and posterior subcapsular cataracts," Br. J. Ophthalmol. **87**, 964–7 (2003).

53. D. B. Elliott and P. Situ, "Visual acuity versus letter contrast sensitivity in early cataract," Vision Res. **38**, 2047–2052 (1998).

54. D. B. Elliott, J. Gilchrist, and D. Whitaker, "Contrast sensitivity and glare sensitivity changes with three types of cataract morphology: are these techniques necessary in a clinical evaluation of cataract?," Ophthalmic Physiol. Opt. **9**, 25–30 (1989).

55. R. Hess and G. Woo, "Vision through cataracts," Invest. Ophthalmol. Vis. Sci. **17**, 428–35 (1978).

56. A. P. Ginsburg, "Contrast sensitivity: determining the visual quality and function of cataract, intraocular lenses and refractive surgery.," Curr. Opin. Ophthalmol. **17**, 19–26 (2006).

57. C. Paz Filgueira, R. F. Sánchez, L. A. Issolio, and E. M. Colombo, "Straylight and Visual Quality on Early Nuclear and Posterior Subcapsular Cataracts," Curr. Eye Res. **41**, 1209–1215 (2016).

58. T. Bal, T. Coeckelbergh, J. Van Looveren, J. J. Rozema, and M.-J. Tassignon, "Influence of Cataract Morphology on Straylight and Contrast Sensitivity and Its Relevance to Fitness to Drive," Ophthalmologica **225**, 105–111 (2011).

59. D. B. Elliott, M. A. Hurst, and J. Weatherill, "Comparing clinical tests of visual function in cataract with the patient's perceived visual disability," Eye **4**, 712–717 (1990).

60. B. E. K. Klein, R. Klein, K. L. P. Linton, Y. L. Magli, and M. W. Neider, "Assessment of Cataracts from Photographs in the Beaver Dam Eye Study," Ophthalmology **97**, 1428–1433 (1990).

61. J. Flammer and H. Bebie, "Lens Opacity Meter: A New Instrument to Quantify Lens Opacity," Ophthalmologica **195**, 69–72 (1987).

62. D. W. Richards, S. R. Russell, and D. R. Anderson, "A method for improved biometry of the anterior chamber with a Scheimpflug technique," Invest. Ophthalmol. Vis. Sci. **29**, 1826–35 (1988).

63. A. Pennos, H. Ginis, A. Arias, D. Christaras, and P. Artal, "Performance of a differential contrast sensitivity method to measure intraocular scattering," Biomed. Opt. Express **8**, 1382–1389 (2017).

64. L. E. Paulsson and J. Sjöstrand, "Contrast sensitivity in the presence of a glare light. Theoretical concepts and preliminary clinical studies," Invest. Ophthalmol. Vis. Sci. **19**, 401–6 (1980).

65. J. Thaung, C. Beckman, M. Abrahamsson, and J. Sjöstrand, "The "light scattering factor". Importance of stimulus geometry, contrast definition, and adaptation," Invest. Ophthalmol. Vis. Sci. **36**, 2313–7 (1995).

66. H. Ginis, O. Sahin, A. Pennos, and P. Artal, "Compact optical integration instrument to measure intraocular straylight," Biomed. Opt. Express **5**, 3036–41 (2014).

67. H. Ginis, G. M. Pérez, J. M. Bueno, and P. Artal, "The wide-angle point spread function of the human eye reconstructed by a new optical method," J. Vis. **12**, 1–10 (2012).

68. H. Ginis, I. Pentari, D. de Brouwere, D. Bouzoukis, I. Naoumidi, and I. Pallikaris, "Narrow angle light scatter in rabbit corneas after excimer laser surface ablation," Ophthalmic Physiol. Opt. **29**, 357–362 (2009).

69. P. Artal, A. Benito, G. M. Pérez, E. Alcón, Á. De Casas, J. Pujol, and J. M. Marín, "An Objective Scatter Index Based on Double-Pass Retinal Images of a Point Source to Classify Cataracts," PLoS One **6**, e16823 (2011).

70. O. Sahin, A. Pennos, H. Ginis, L. Hervella, E. A. Villegas, B. Cañizares, J. M. Marin, I. Pallikaris, and P. Artal, "Optical Measurement of Straylight in Eyes With Cataract," J. Refract. Surg. **32**, 846–850 (2016).

71. W. L. Wong, X. Li, J. Li, C.-Y. Cheng, E. L. Lamoureux, J. J. Wang, C. Y. Cheung, and T. Y. Wong, "Cataract Conversion Assessment using Lens Opacity Classification System III and Wisconsin Cataract Grading System," Investig. Opthalmology Vis. Sci. **54**, 280 (2013).

72. B. F. Valbon, M. R. Alves, and R. Ambrósio Jr, "Correlações entre straylight, aberrometria, opacidade e densitometria do cristalino em pacientes com catarata," Rev. Bras. Oftalmol. **72**, 244–248 (2013).

73. R. Michael, L. J. van Rijn, T. J. T. P. van den Berg, R. I. Barraquer, G. Grabner, H. Wilhelm, T. Coeckelbergh, M. Emesz, P. Marvan, and C. Nischler, "Association of lens opacities, intraocular straylight, contrast sensitivity and visual acuity in European drivers," Acta Ophthalmol. **87**, 666–671 (2009).

74. F. J. Ascaso and V. Huerv, "The History of Cataract Surgery," in *Cataract Surgery* (InTech, 2013).

75. C. E. Gilbert, G. V. S. Murthy, S. Sivasubramaniam, F. Kyari, A. Imam, M. M. Rabiu, M. Abdull, and A. Tafida, "Couching in Nigeria: Prevalence, Risk Factors and Visual Acuity Outcomes," Ophthalmic Epidemiol. **17**, 269–275 (2010).

76. M. A. Bamashmus, "Traditional Arabic technique of couching for cataract treatment in Yemen," Eur. J. Ophthalmol. **20**, 340–4 (2010).

77. D. Pascolini and S. P. Mariotti, "Global estimates of visual impairment: 2010," Br. J. Ophthalmol. **96**, 614–618 (2012).

78. E. Chan, O. A. R. Mahroo, and D. J. Spalton, "Complications of cataract surgery," Clin. Exp. Optom. **93**, 379–389 (2010).

79. S. M. Raj, A. R. Vasavada, S. R. K. Johar, V. A. Vasavada, and V. A. Vasavada, "Post-operative capsular opacification: a review," Int. J. Biomed. Sci. **3**, 237–50 (2007).

80. S. Marcos, J. S. Werner, S. A. Burns, W. H. Merigan, P. Artal, D. A. Atchison, K. M. Hampson, R. Legras, L. Lundstrom, G. Yoon, J. Carroll, S. S. Choi, N. Doble, A. M. Dubis, A. Dubra, A. Elsner, R. Jonnal, … L. C. Sincich, "Vision science and adaptive optics, the state of the field," Vision Res. **132**, 3–33 (2017).

81. P. Artal, L. Chen, E. J. Fernández, B. Singer, S. Manzanera, and D. R. Williams, "Neural compensation for the eye's optical aberrations," J. Vis. **4**, 4 (2004).

82. E. J. Fernández, I. Iglesias, and P. Artal, "Closed-loop adaptive optics in the human eye," Opt. Lett. **26**, 746–8 (2001).

83. B. C. Platt and R. Shack, "History and Principles of Shack-Hartmann Wavefront Sensing," J. Refract. Surg. **17**, S573-7 (2001).

84. J. Liang, D. R. Williams, and D. T. Miller, "Supernormal vision and high-resolution retinal imaging through adaptive optics," J. Opt. Soc. Am. A **14**, 2884–92 (1997).

85. L. N. Thibos and X. Hong, "Clinical applications of the Shack-Hartmann aberrometer," Optom. Vis. Sci. **76**, 817–25 (1999).

86. R. Shetty, S. Kochar, T. Grover, P. Khamar, P. Kusumgar, K. Sainani, and A. Sinha Roy, "Repeatability of a Commercially Available Adaptive Optics Visual Simulator and Aberrometer in Normal and Keratoconic Eyes," J. Refract. Surg. **33**, 769–772 (2017).

87. N. Maeda, T. Fujikado, T. Kuroda, T. Mihashi, Y. Hirohara, K. Nishida, H. Watanabe, and Y. Tano, "Wavefront aberrations measured with Hartmann-Shack sensor in patients with keratoconus," Ophthalmology **109**, 1996–2003 (2002).

88. N. Sachdev, S. E. Ormonde, T. Sherwin, and C. N. J. McGhee, "Higher-order aberrations of lenticular opacities," J. Cataract Refract. Surg. **30**, 1642–8 (2004).

89. W. J. Donnelly, K. Pesudovs, J. D. Marsack, E. J. Sarver, and R. A. Applegate, "Quantifying Scatter in Shack-Hartmann Images to Evaluate Nuclear Cataract," J. Refract. Surg. **20**, S515–S522 (2004).

90. R. Navarro and E. Moreno-Barriuso, "Laser ray-tracing method for optical testing," Opt. Lett. **24**, 951–3 (1999).

91. F. Faria-Correia, B. Lopes, T. Monteiro, N. Franqueira, and R. Ambrósio, "Scheimpflug lens densitometry and ocular wavefront aberrations in patients with mild nuclear cataract," J. Cataract Refract. Surg. **42**, 405–11 (2016).

92. L. Y. Qiao, X. H. Wan, X. G. Cai, B. Vasudevan, Y. Xiong, J. X. Tan, Z. Guan, D. A. Atchison, and N. L. Wang, "Comparison of ocular modulation transfer function determined by a ray-tracing aberrometer and a double-pass system in early cataract patients," Chin. Med. J. (Engl). **127**, 3454–8 (2014).

93. D. Akbulut, T. J. Huisman, E. G. van Putten, W. L. Vos, and A. P. Mosk, "Focusing light through random photonic media by binary amplitude modulation," Opt. Express **19**, 4017 (2011).

94. I. M. Vellekoop and A. P. Mosk, "Focusing coherent light through opaque strongly scattering media," Opt. Lett. **32**, 2309 (2007).

95. I. M. Vellekoop and A. P. Mosk, "Phase control algorithms for focusing light through turbid media," Opt. Commun. **281**, 3071–3080 (2008).

96. D. B. Conkey, A. N. Brown, A. M. Caravaca-Aguirre, and R. Piestun, "Genetic algorithm optimization for focusing through turbid media in noisy environments," Opt. Express **20**, 4840 (2012).

97. O. Katz, E. Small, and Y. Silberberg, "Looking around corners and through thin turbid layers in real time with scattered incoherent light," Nat. Photonics **6**, 549 (2012).

98. H. Yu, J. Park, K. Lee, J. Yoon, K. Kim, S. Lee, and Y. Park, "Recent advances in wavefront shaping techniques for biomedical applications," Curr. Appl. Phys. **15**, 632–641 (2015).

99. H. Yu, P. Lee, K. Lee, J. Jang, J. Lim, W. Jang, Y. Jeong, and Y. Park, "*In vivo* deep tissue imaging using wavefront shaping optical coherence tomography," J. Biomed. Opt. **21**, 101406 (2016).

100. A. M. Caravaca-Aguirre and R. Piestun, "Single multimode fiber endoscope," Opt. Express **25**, 1656 (2017).

101. E. J. Fernández, P. M. Prieto, and P. Artal, "Binocular adaptive optics visual simulator," Opt. Lett. **34**, 2628 (2009).

102. Z. Zhang, Z. You, and D. Chu, "Fundamentals of phase-only liquid crystal on silicon (LCOS) devices," Light Sci. Appl. **3**, e213–e213 (2014).

103. W. H. Lee, "III Computer-Generated Holograms: Techniques and Applications," Prog. Opt. **16**, 119–232 (1978).

104. D. B. Conkey, A. M. Caravaca-Aguirre, and R. Piestun, "High-speed scattering medium characterization with application to focusing light through turbid media," Opt. Express **20**, 1733–1740 (2012).

105. F. Roddier and Cambridge University Press., *Adaptive Optics in Astronomy* (Cambridge University Press, 1999).

106. E. J. Fernández and P. Artal, "Membrane deformable mirror for adaptive optics: performance limits in visual optics," Opt. Express **11**, 1056 (2003).

107. T. Bifano, "Adaptive imaging: MEMS deformable mirrors," Nat. Publ. Gr. **5**, 21–23 (2011).

108. T. G. Bifano, Y. Lu, C. Stockbridge, A. Berliner, J. Moore, R. Paxman, S. Tripathi, and K. Toussaint, "MEMS spatial light modulators for controlled optical transmission through nearly opaque materials," in *MEMS Adaptive Optics VI* (SPIE, 2012), Vol. 8253, p. 82530L.

109. D. Miller, J. L. Zuckerman, and G. O. Reynolds, "Phase aberration balancing of cataracts using holography," Exp. Eye Res. **15**, 157–160 (1973).

110. D. F. Sweeney, T. J. Millar, and S. R. Raju, "Tear film stability: A review," Exp. Eye Res. **117**, 28–38 (2013).

111. S. Martinez-Conde, S. L. Macknik, and D. H. Hubel, "The role of fixational eye movements in visual perception," Nat. Rev. Neurosci. (2004).

112. H. A. Anderson, A. Glasser, R. E. Manny, and K. K. Stuebing, "Age-related changes in accommodative dynamics from preschool to adulthood," Invest. Ophthalmol. Vis. Sci. **51**, 614–22 (2010).

113. R. Navarro, "Incorporation of intraocular scattering in schematic eye models," J. Opt. Soc. Am. A **2**, 1891–1894 (1985).

114. T. J. van den Berg, "Light scattering by donor lenses as a function of depth and wavelength," Invest. Ophthalmol. Vis. Sci. **38**, 1321–1332 (1997).

115. Y. C. Chen, C. J. Jiang, T. H. Yang, and C. C. Sun, "Development of a human eye model incorporated with intraocular scattering for visual performance assessment," J. Biomed. Opt. **17**, 075009 (2012).

116. R. Paeglis, M. Ozolinsh, P. Cikmacs, and S. Andersson-Engels, "Eye model with controllable lens scattering," in *Hybrid and Novel Imaging and New Optical Instrumentation for Biomedical Applications* (SPIE, 2001), Vol. 4434, pp. 233–238.

117. H. Ginis, G. M. Perez, J. M. Bueno, and P. Artal, "The wide-angle point spread function of the human eye reconstructed by a new optical method," J. Vis. **12**, 20–20 (2012).

118. P. H. B. Kok, H. W. van Dijk, T. J. T. P. van den Berg, and F. D. Verbraak, "A Model for the Effect of Disturbances in the Optical Media on the OCT Image Quality," Invest. Ophthalmol. Vis. Sci. **50**, 787–792 (2009).

119. G. C. De Wit, L. Franssen, J. E. Coppens, and T. J. T. P. Van Den Berg, "Simulating the straylight effects of cataracts," J. Cataract Refract. Surg. **32**, 294–300 (2006).

120. H. Ginis, J. J. Rozema, M.-J. B. R. Tassignon, and P. Artal, "A phase perturbation model of light scattering in the human eye," Invest. Ophthalmol. Vis. Sci. **55**, 2120 (2014).

121. A. Arias, H. Ginis, and P. Artal, "Physical Model of Intraocular Scattering using a Spatial Light Modulator," Invest. Ophthalmol. Vis. Sci. **56**, 1066 (2015).

122. T. Coleman and Y. Zhang, *Optimization Toolbox for Use with MATLAB User's Guide* (MathWorks, 2018).

123. P. Szendro, G. Vincze, and A. Szasz, "Pink-noise behaviour of biosystems," Eur. Biophys. J. **30**, 227–31 (2001).

124. M. Xu and R. R. Alfano, "Fractal mechanisms of light scattering in biological tissue and cells," Opt. Lett. **30**, 3051–3053 (2005).

125. J. S. McLellan, S. Marcos, and S. A. Burns, "Age-related changes in monochromatic wave aberrations of the human eye," Invest. Ophthalmol. Vis. Sci. **42**, 1390–5 (2001).

126. "ZernikeCalc - File Exchange - MATLAB Central," https://es.mathworks.com/matlabcentral/fileexchange/33330-zernikecalc.

127. L. N. Thibos, A. Bradley, and R. A. Applegate, "Metrics of Optical Quality of the Eye," J. Vis. **4**, 322–8 (2003).

128. A. Guirao, C. González, M. Redondo, E. Geraghty, S. Norrby, and P. Artal, "Average optical performance of the human eye as a function of age in a normal population," Invest. Ophthalmol. Vis. Sci. **40**, 203–13 (1999).

129. J. Santamaría, P. Artal, and J. Bescós, "Determination of the point-spread function of human eyes using a hybrid optical-digital method.," J. Opt. Soc. Am. A **4**, 1109–14 (1987).

130. J. A. Martínez-Roda, M. Vilaseca, J. C. Ondategui, M. Aguirre, and J. Pujol, "Effects of aging on optical quality and visual function," Clin. Exp. Optom. **99**, 518–525 (2016).

131. F. Díaz-Doutón, A. Benito, J. Pujol, M. Arjona, J. L. Guell, and P. Artal, "Comparison of the Retinal Image Quality with a Hartmann-Shack Wavefront Sensor and a Double-Pass Instrument," Investig. Opthalmology Vis. Sci. **47**, 1710 (2006).

132. H. S. Ginis, G. M. Perez, J. M. Bueno, A. Pennos, and P. Artal, "Wavelength dependence of the ocular straylight," Invest. Ophthalmol. Vis. Sci. **54**, 3702–8 (2013).

133. D. Christaras, H. Ginis, A. Pennos, and P. Artal, "Scattering contribution to the double-pass PSF using Monte Carlo simulations," Ophthalmic Physiol. Opt. **37**, 342–346 (2017).

134. G. C. Simpson, "Ocular haloes and coronas," Br. J. Ophthalmol. **37**, 450–86 (1953).

135. T. J. T. P. van den Berg, M. P. J. Hagenouw, and J. E. Coppens, "The ciliary corona: Physical model and simulation of the fine needles radiating from point light sources," Investig. Ophthalmol. Vis. Sci. **46**, 2627–2632 (2005).

136. P. Ferraro, S. De Nicola, G. Coppola, A. Finizio, D. Alfieri, and G. Pierattini, "Controlling image size as a function of distance and wavelength in Fresnel-transform reconstruction of digital holograms," Opt. Lett. **29**, 854–856 (2004).

137. J. C. Stevens and S. S. Stevens, "Brightness Function: Effects of Adaptation*," J. Opt. Soc. Am. **53**, 375 (1963).

138. T. H. Wertheim and I. L. Dunsky, "Peripheral Visual Acuity," Optom. Vis. Sci. **57**, 915–924 (1980).

139. M. H. Kao, K. A. Jester, A. G. Yodh, and P. J. Collings, "Observation of Light Diffusion and Correlation Transport in Nematic Liquid Crystals," Phys. Rev. Lett. **77**, 2233–2236 (1996).

140. F. Forooghian, E. Agrón, T. E. Clemons, F. L. Ferris, E. Y. Chew, and Age-Related Eye Disease Study Research Group, "Visual acuity outcomes after cataract surgery in patients with age-related macular degeneration: age-related eye disease study report no. 27," Ophthalmology **116**, 2093–100 (2009).

141. M. Lundström, K. G. Brege, I. Florén, B. Lundh, U. Stenevi, and W. Thorburn, "Cataract surgery and quality of life in patients with age related macular degeneration," Br. J. Ophthalmol. **86**, 1330–5 (2002).

142. Y. Ma, J. Huang, B. Zhu, Q. Sun, Y. Miao, and H. Zou, "Cataract surgery in patients with bilateral advanced age-related macular degeneration: Measurement of visual acuity and quality of life," J. Cataract Refract. Surg. **41**, 1248–1255 (2015).

143. E. Mönestam and B. Lundqvist, "Long-term visual outcome after cataract surgery: Comparison of healthy eyes and eyes with age-related macular degeneration," J. Cataract Refract. Surg. **38**, 409–414 (2012).

144. P. Artal, "Optics of the eye and its impact in vision: a tutorial," Adv. Opt. Photonics **6**, 340 (2014).

145. D. Yager, R. Yuan, and S. Mathews, "What is the utility of the psychophysical "light scattering factor"?," Invest. Ophthalmol. Vis. Sci. **33**, 688–90 (1992).

146. N. A. P. Brown, "The morphology of cataract and visual performance," Eye **7**, 63–67 (1993).

147. B. Treutwein, "Adaptive psychophysical procedures," Vision Res. **35**, 2503–2522 (1995).

148. A. B. Watson and D. G. Pelli, "QUEST: a Bayesian adaptive psychometric method.," Percept. Psychophys. **33**, 113–20 (1983).

149. J. Rovamo, V. Virsu, and R. Nasanen, "Cortical magnification factor predicts the photopic contrast sensitivity of peripheral vision," Nature **271**, 54–56 (1978).

150. R. Rosen, L. Lundstrom, A. P. Venkataraman, S. Winter, and P. Unsbo, "Quick contrast sensitivity measurements in the periphery," J. Vis. **14**, 3–3 (2014).

151. F. J. Martínez, A. Márquez, S. Gallego, M. Ortuño, J. Francés, A. Beléndez, and I. Pascual, "Averaged Stokes polarimetry applied to evaluate retardance and flicker in PA-LCoS devices," Opt. Express **22**, 15064–74 (2014).

152. C. Ramirez, B. Karakus, A. Lizana, and J. Campos, "Polarimetric method for liquid crystal displays characterization in presence of phase fluctuations," Opt. Express **21**, 3182–3192 (2013).

153. P. A. Cheremkhin, N. N. Evtikhiev, V. V Krasnov, V. G. Rodin, and S. N. Starikov, "Reduction of phase temporal fluctuations caused by digital voltage addressing in LC SLM "HoloEye PLUTO VIS" for holographic applications," in *Practical Holography XXVIII: Materials and Applications* (SPIE, 2014), Vol. 9006, p. 900615.

154. A. Márquez, F. J. Martínez, S. Gallego, M. Ortuño, J. Francés, A. Beléndez, and I. Pascual, "Static and dynamic effects of flicker in phase multilevel elements on LCoS devices," in *Optics and Photonics for Information Processing IX* (SPIE, 2015), Vol. 9598, p. 95980C.

155. E. J. Fernandez, P. M. Prieto, E. Chirre, and P. Artal, "Performance of a 6-Pi liquid crystal on silicon (LCoS) spatial light modulator under white light illumination for visual applications," in *Imaging and Applied Optics, OSA Technical Digest (Online)*, Optical Society of America, ed. (2013), p. OM3A.3.

156. A. P. Bondareva, P. A. Cheremkhin, N. N. Evtikhiev, V. V. Krasnov, R. S. Starikov, and S. N. Starikov, "Measurement of characteristics and phase modulation accuracy increase of LC SLM "HoloEye PLUTO VIS,"" J. Phys. Conf. Ser. **536**, 012011 (2014).

157. V. Arrizón, E. Carreón, and M. Testorf, "Implementation of Fourier array illuminators using pixelated SLM: efficiency limitations," Opt. Commun. **160**, 207–213 (1999).

158. J. Harriman, A. Linnenberger, and S. Serati, "Improving spatial light modulator performance through phase compensation," in *Advanced Wavefront Control: Methods, Devices, and Applications II* (SPIE, 2004), Vol. 5553.

159. J. Xia, C. Chang, Z. Chen, Z. Zhu, T. Zeng, P.-Y. Liang, and J. Ding, "Pixel-addressable phase calibration of spatial light modulators: a common-path phase-shifting interferometric microscopy approach," J. Opt. **19**, 125701 (2017).

160. E. Hällstig, J. Stigwall, T. Martin, L. Sjöqvist, and M. Lindgren, "Fringing fields in a liquid crystal spatial light modulator for beam steering," J. Mod. Opt. **51**, 1233 (2004).

161. B. Apter, U. Efron, and E. Bahat-Treidel, "On the fringing-field effect in liquid-crystal beam-steering devices," Appl. Opt. **43**, 11 (2004).

162. A. Ravikumar, J. D. Marsack, H. E. Bedell, and R. A. Applegate, "Change in visual acuity is well correlated with change in image-quality metrics for both normal and keratoconic wavefront errors," J. Vis. **13**, 28 (2013).

163. A. Ravikumar, E. J. Sarver, and R. A. Applegate, "Change in visual acuity is highly correlated with change in six image quality metrics independent of wavefront error and/or pupil diameter," J. Vis. **12**, 11 (2012).

164. G. D. Boreman and S. Yang, "Modulation Transfer Function Measurement Using Three- and Four-bar Targets," Appl. Opt. **34**, 8050–2 (1995).

165. G. Yoon, "The use of metrics and adaptive optics to evaluate different correction strategies for highly aberrated eyes," in *Wavefront Congress* (2008).

166. J. Lee Rodgers and W. Alan Nice Wander, "Thirteen ways to look at the correlation coefficient," Am. Stat. **42**, 59–66 (1988).

167. S. Marcos, E. Moreno, and R. Navarro, "The depth-of-field of the human eye from objective and subjective measurements," Vision Res. **39**, 2039–2049 (1999).

168. M. Rolfs, "Microsaccades: Small steps on a long way," Vision Res. **49**, 2415–41 (2009).

169. S. Meimon, J. Jarosz, C. Petit, E. G. Salas, K. Grieve, J.-M. Conan, B. Emica, M. Paques, and K. Irsch, "Pupil motion analysis and tracking in ophthalmic systems equipped with wavefront sensing technology," Appl. Opt. **56**, D66–D71 (2017).

170. W. Kosnik, J. Fikre, and R. Sekuler, "Visual fixation stability in older adults," Investig. Ophthalmol. Vis. Sci. **27**, 1720–5 (1986).

171. H. R. Lieberman and A. P. Pentland, "Microcomputer-based estimation of psychophysical thresholds: The Best PEST," Behav. Res. Methods Instrum. **14**, 21–25 (1982).

172. S. Marcos, L. Sawides, E. Gambra, and C. Dorronsoro, "Influence of adaptive-optics ocular aberration correction on visual acuity at different luminances and contrast polarities," J. Vis. **8**, 1 (2008).

173. C. Schwarz, S. Manzanera, and P. Artal, "Binocular visual performance with aberration correction as a function of light level," J. Vis. **14**, 6 (2014).

174. R. J. Jacobs, I. L. Bailey, and M. a Bullimore, "Artificial pupils and Maxwellian view," Appl. Opt. **31**, 3668–77 (1992).

175. Thorlabs, "Unmounted N-BK7 Ground Glass Diffusers," https://www.thorlabs.com/newgrouppage9.cfm?objectgroup_id=1132.

176. P. Artal, S. Marcos, R. Navarro, and D. R. Williams, "Odd aberrations and double-pass measurements of retinal image quality," J. Opt. Soc. Am. A **12**, 195–201 (1995).

177. S. Marcos, R. Navarro, and P. Artal, "Coherent imaging of the cone mosaic in the living human eye," J. Opt. Soc. Am. A **13**, 897–905 (1996).

178. C. E. García-Guerra, M. Aldaba, M. Arjona, and J. Pujol, "Speckle reduction in double-pass retinal images using variable-focus lenses," J. Eur. Opt. Soc. **10**, 15001 (2015).

179. P. Artal, I. Iglesias, N. López-Gil, and D. G. Green, "Double-pass measurements of the retinal-image quality with unequal entrance and exit pupil sizes and the reversibility of the eye's optical system," J. Opt. Soc. Am. A. Opt. Image Sci. Vis. **12**, 2358–66 (1995).

180. N. López-Gil and P. Artal, "Comparison of double-pass estimates of the retinal-image quality obtained with green and near-infrared light," J. Opt. Soc. Am. A **14**, 961–71 (1997).

181. E. J. Fernández and P. Artal, "Ocular aberrations up to the infrared range: from 632.8 to 1070 nm," Opt. Express **16**, 21199–21208 (2008).

182. H. Hofer, P. Artal, B. Singer, J. L. Aragón, and D. R. Williams, "Dynamics of the eye's wave aberration," J. Opt. Soc. Am. A **18**, 497–506 (2001).

183. V. Albanis, E. N. Ribak, and Y. Carmon, "Speckle reduction in ocular wave-front sensing," ArXiv e-prints **0704.2173**, (2007).

184. J. L. M. Fuentes, E. J. Fernández, P. M. Prieto, and P. Artal, "Interferometric method for phase calibration in liquid crystal spatial light modulators using a self-generated diffraction-grating," Opt. Express **24**, 14159 (2016).

PUBLICATIONS RELATED TO THIS THESIS

Peer reviewed journal publications

Light scattering in the human eye modelled as random phase perturbations

Augusto Arias, Harilaos Ginis, Pablo Artal

Biomedical Optics Express 9, 2664-2670 (2018).

Performance of a differential contrast sensitivity method to measure intraocular scattering

Alexandros Pennos, Augusto Arias, Dimitrios Christaras, Harilaos Ginis, Pablo Artal

Biomedical Optics Express 8, 1382-1389 (2017).

Peer-reviewed conference papers

Physical Model of Intraocular Scattering using a Spatial Light Modulator

Augusto Arias, Harilaos Ginis, Pablo Artal

Investigative Ophthalmology & Visual Science 57, 1066 (2015).

Visual impact of artificially induced intraocular scatter with a liquid crystal phase modulator

Augusto Arias, Alexandros Pennos, Harilaos Ginis, Pablo Artal

Investigative Ophthalmology & Visual Science 57, 215 (2016).

Novel Approach for Generating Ocular Wavefronts

Augusto Arias, Alexandros Pennos, Harilaos Ginis, Pablo Artal

Latin America Optics and Photonics Conference, Optical Society of America, paper LTh2C.3 (2016).

Impact of induced intraocular scatter in visual performance in the near periphery

Augusto Arias, Diego Montagud, Enrique-Josua Fernandez, Pablo Artal

Investigative Ophthalmology & Visual Science 58, 4226 (2017).

Wavefront shaping to correct intraocular scattering

Pablo Artal, Augusto Arias, Enrique-Josua Fernandez

Adaptive Optics and Wavefront Control for Biological Systems IV, 105020Q, Proc. SPIE 10502 (2018).

Optical correction of the effects of cataracts

Augusto Arias, Enrique-Josua Fernandez, Pablo Artal

ACKNOWLEDGMENTS

This work is the result of the effort of many people and institutions. Surely, the following lines are not enough to express all my thankfulness.

I thank to Pablo Artal and Josua Fernandez, directors of this thesis, because of the opportunity to develop this project and their contributions. My gratitude is extended to all (current and formers) members of the LOUM and Voptica, who made this period more pleasant. I am really grateful to Carmen Martinez for her kind help to understand the university's procedures.

During this project, I had the great opportunity to work with Haris Ginis, whom I am grateful because of his helpful discussions. I recognize the received encouragement from him and the rest of the local greek community (Dimitris, Alexandros and Kleoniki). Moreover, I thank to Diego Montagud for his scientific contribution.

The support of my family was fundamental throughout this adventure. Once again, I would like to say 'thank you' to Elena. Being aware of the reduced time to my friends as consequence of this work, I would like to express not only my gratitude, but also my excuses.

Finally, thank you for the complete reading (I hope) of this manuscript.